

CONE-BASED ELECTRICAL RESISTIVITY TOMOGRAPHY

A DISSERTATION

SUBMITTED TO THE DEPARTMENT OF GEOPHYSICS

AND THE COMMITTEE ON GRADUATE STUDIES

OF STANFORD UNIVERSITY

IN PARTIAL FULFILLMENT OF THE REQUIREMENTS

FOR THE DEGREE OF

DOCTOR OF PHILOSOPHY

Adam Pidlisecky  
March 2006

©Copyright by Adam Pidlisecky 2006  
All Rights Reserved

I Certify that I have read this dissertation and that, in my opinion, it is fully adequate in scope and quality as a dissertation for the degree of Doctor of Philosophy.

---

Rosemary Knight, Principal Adviser

I Certify that I have read this dissertation and that, in my opinion, it is fully adequate in scope and quality as a dissertation for the degree of Doctor of Philosophy.

---

Jerry M. Harris

I Certify that I have read this dissertation and that, in my opinion, it is fully adequate in scope and quality as a dissertation for the degree of Doctor of Philosophy.

---

Gary Mavko

Approved for the University Committee on Graduate Studies.

# ABSTRACT

---

Determining the 3-D spatial distribution of subsurface properties is a critical part of managing the clean-up of contaminated sites. Most standard hydrologic methods sample small regions immediately adjacent to wells or testing devices. This provides data which are not representative of the entire region of interest. Furthermore, at many contaminated sites invasive methods are not acceptable, due to the risks associated with contacting and spreading the contaminants. To address these issues, I have developed a minimally invasive technology that provides information about the 3-D distribution of electrical conductivity. This new technique, cone-based electrical resistivity tomography (C-bert), integrates the existing technologies of resistivity cone penetration testing (RCPT) with electrical resistivity tomography. Development of this tool included the creation of new software and modeling algorithms, the design of field equipment, field testing, and processing and interpretation of the resulting data.

I present a 2.5-D forward modeling algorithm that incorporates an effective correction for the errors caused by boundary effects and source singularities. The algorithm includes an optimization technique for acquiring the Fourier coefficients required for the solution. A 3-D inversion algorithm is presented that has two major improvements over existing algorithms. First, it includes a 3-D version of the boundary correction/source singularity correction developed for the 2.5-D problem. Second, the algorithm can handle any type of acquisition geometry; this was a requirement for the development of C-bert.

C-bert involves placing several permanent current electrodes in the subsurface and using electrodes mounted on a cone penetrometer and at the surface to measure the resultant potential field. In addition to these measurements, we obtain the standard suite of RCPT data, including high resolution resistivity logs. The RCPT data can be used to generate a realistic starting model for the inversion. Furthermore, the resistivity logs can be used as constraints in the inversion of the potential field data. Effective incorporation of resistivity logs into the inversion process, however, requires an understanding the spatial averaging that occurs during logging. I developed a forward modeling and

inversion algorithm that allows us to understand and remove the averaging that is present in the logs. A successful field test of C-bert was conducted at the Kidd2 site in Richmond, British Columbia, leading me to conclude that C-bert is a promising new way to image the subsurface.

# ACKNOWLEDGMENTS

First off, I would like to thank Rosemary Knight. Rosemary has been a wonderful advisor and mentor. As an advisor she has guided my research using a tempered hand, always letting me freely explore the many scientific avenues one encounters during research, while being there to nudge me back on the road map when I would stray too far. As a mentor, Rosemary has helped me develop as a person as well as a scientist. Her mentorship has led me to understand and appreciate the balancing act that is required when managing a successful research group, an academic career and a life. It has been a true privilege to have worked with her.

I would also like to thank Eldad Haber. Eldad has been a wonderful collaborator over the years. At the beginning of my Ph.D. Eldad was to be the collaborator who would do all of the inverse modeling for my proposed project. However, within the first year, Eldad forced me to delve into the details of inversion. Once I got involved with the details of inversion, I was hooked. I find this a fascinating area of research and hope to continue working on it.

John Howie has been an invaluable resource and collaborator. As a Civil engineer, he has kept me grounded in the reality of what engineers are interested in knowing, not what we as Geophysicists think they should know. His help and generosity with field equipment has made much of this research possible.

Thanks to Jerry Harris and Gary Mavko, my committee members. Both have offered me great advice over the past four years. It is amazing to see that, despite not knowing the intimate details of my work, their commentary and analysis have been particularly relevant and insightful.

Thanks to Kamini Singha. Kamini has taught me most of what I know about ERT. She has offered candid commentary and great advice on my work. She is also largely responsible for my being obsessed about making perfect power point slides. I am not sure whether or not I owe thanks for that. Either way she is now promoted to A-1 Awesome Commander of the Universe.

Thanks to all of the members of the Environmental Geophysics Group. In particular, my office mates Kristina Keating and James Irving. Both of whom have endured many days of either surliness or satirical abuse from me.

Thanks to all the people who helped with the C-bert Field experient at Kidd2: Ali Amini, Scott Jackson, Rob Jasper, Rob Sanders, Matt Lennox-King, Jenny Dicus, James Irving, John Howie

I owe much thanks to my great friends. If it wasn't for their support I can't imagine having made it through this degree. In particular I would like to thank Brad Artman. Brad is single handedly responsible for having gotten me utterly addicted to sailing, for that I will always be indebted to him. Stanford has allowed me to meet and nurture relationships with amazing people, all of whom I hope to be friends with for years to come: Kamini Singha, Steve Hubbard, Martine Ast, James Irving, Kristina Keating, Seth Haines, Dave Shelly, Dave Wynn, Darcy McPhee, Charlie Wilson, C.J. Powers, Sang-Ho Yun, Ted Callahan.

My parents have been amazingly supportive of me over the years. To say I was a challenging child to raise would be the understatement of the year. Despite this they always supported my endeavors. Without their ongoing support, this dissertaion would never have been realized.

Finally, I want to thank my girlfriend Tasha Reddy. Simply put, meeting Tasha has made my Stanford experience truly spectacular. I would never have made it through without her support and love. I am also indebted to her for her bravery, she didn't bat an eye at the concept of living on a boat, and has worked hard over the last four years to make boat life a great experience.

Funding for my studies came from a Department of Geophysics Graduate student fellowship. Support for my field work came from a McGee grant, from the School of Earth Sciences and a Shell fund grant from the Department of Geophysics.

# TABLE OF CONTENTS

<b>ABSTRACT.....</b>	<b>iv</b>
<b>ACKNOWLEDGMENTS .....</b>	<b>vi</b>
<b>TABLE OF CONTENTS .....</b>	<b>viii</b>
<b>LIST OF TABLES .....</b>	<b>xi</b>
<b>LIST OF FIGURES .....</b>	<b>xii</b>
<b>CHAPTER 1: INTRODUCTION.....</b>	<b>1</b>
<b>CHAPTER 2: AN IMPROVED 2.5-D ELECTRICAL RESISTIVITY MODELLING ALGORITHM .....</b>	<b>4</b>
Abstract.....	4
2.1 Introduction.....	5
2.2 The Forward Problem .....	7
2.2.1 Governing equations .....	7
2.2.2 Discretizing the operators .....	8
2.2.3 Correction for BC and source singularities.....	10
2.2.4 Optimizing the choice of k and g.....	12
2.3 MATLAB Implementation .....	15
2.3.1 Data structure.....	15
2.3.2 Calculating q.....	17
2.3.3 Calculating k and g .....	20
2.3.4 Solving the Forward Problem .....	20
2.3.5 Picking data.....	21
2.4 Examples.....	22
2.4.1 A surface survey of layered media.....	22
2.4.2 Fullspace Solution.....	24
2.5 Discussion.....	26
<b>CHAPTER 3: A 3-D DC RESISTIVITY INVERSION ALGORITHM .....</b>	<b>27</b>
Abstract.....	27
3.1 Introduction.....	28
3.2 Theory .....	30
3.2.1 The forward problem .....	30
3.2.1.1 Governing equations .....	30
3.2.1.2 Parameterizing the forward problem .....	31
3.2.1.3 Boundary conditions and source term improvement .....	32
3.2.2 The inverse problem .....	33
3.2.2.1 Gauss-Newton.....	33

3.2.2.2 Incomplete Gauss-Newton.....	34
3.2.2.3 Line-search and further iterations .....	35
3.2.2.4 The complete algorithm .....	36
3.3 MATLAB Implementation .....	38
3.3.1 Data structure .....	38
3.3.2 Solving the Forward Problem .....	41
3.3.3 Making a right hand side and picking data .....	42
3.3.4 Data weighting .....	43
3.3.5 Regularization and Model weighting.....	43
3.3.5.1 A note on $\beta$ .....	44
3.3.6 Active vs InActive cells .....	45
3.3.7 Incomplete Gauss Newton .....	45
3.4 Examples.....	47
3.4.1 A surface based field experiment.....	47
3.4.1.1 The model .....	47
3.4.1.2 Inverse results .....	47
3.4.2 A example of cone- based electrical resistivity tomography .....	51
3.4.2.1 The model .....	52
3.4.2.2 Inverse results .....	52
3.5 Summary .....	55

## **CHAPTER 4: CONE-BASED ELECTRICAL RESISTIVITY TOMOGRAPHY .. 56**

Abstract.....	56
4.1 Introduction.....	58
4.2 Description of the Field Site .....	62
4.2.1 Kidd2 C-bert Experiment.....	64
4.2.1.1 Description of Cone Truck.....	66
4.2.1.2 Description of the Resistivity Cone .....	66
4.2.1.3 Design and Emplacement of Permanent Electrodes .....	67
4.2.1.4 Data Acquisition .....	71
4.3 Field Results and Interpretation .....	73
4.3.1 Resistivity Cone Data .....	73
4.3.1.1 ERT Forward Modeling.....	75
4.3.1.2 ERT Inversion.....	76
4.3.1.3 The Cone Effect .....	79
4.3.2 Kidd2 Inversion Results.....	87
4.4 C-bert Numerical Experiment.....	89
4.5 Summary and Conclusions .....	95

## **CHAPTER 5: IMPROVED INTERPRETATION OF RESISTIVITY CONE PENETRATION LOGS ..... 96**

Abstract.....	96
5.1 Introduction.....	97

5.2 RCPT.....	100
5.3 Modeling and Inversion .....	103
5.3.1 Forward Modeling .....	103
5.3.2 Inversion .....	105
5.4 Synthetic Examples.....	109
5.4.1 Layers of Varying Thickness .....	110
5.4.2 Layers of Varying Resistivity .....	113
5.4.3 Truncated layers and 3-D effects .....	116
5.5 Field data.....	120
5.5 Conclusions.....	124
<b>CHAPTER 6: CONCLUSIONS .....</b>	<b>126</b>
<b>REFERENCES.....</b>	<b>130</b>

# LIST OF TABLES

<b>Table 2.1</b> Starting and final objective function values for a variety of $n$ values. For $n = 5$ the starting point is a minima and thus the optimization does not improve the estimate of $k$ and $g$ .....	<b>20</b>
<b>Table 4.1</b> Kidd2 Hydrostratigraphic units (after Neilson-Welch and Smith, 2001). .....	<b>62</b>
<b>Table 4.2</b> Testing depths for the tomography component of the C-bert experiment. ....	<b>72</b>

# LIST OF FIGURES

<b>Figure 2.1</b> The finite volume grid.....	<b>9</b>
<b>Figure 2.2</b> Contents of the ‘Para’ structure.....	<b>16</b>
<b>Figure 2.3</b> Map view representations of the $q$ vector. (a) the $q$ term with sources located at cell centers. (b) BC/singularity correction applied to the source term used in (a). (c) difference map of (a) and (b). (d) interpolated $q$ term. (e) BC/singularity correction applied to the source term used in (d). (f) difference image of (d) and (e).....	<b>19</b>
<b>Figure 2.4</b> Upper: The data obtained at the surface from the analytical model, the solution of Xu et al., and our solution using both optimized $k$ and $g$ values and the BC/singularity correction. Lower: The model of 2 layers with current electrodes at the surface.....	<b>23</b>
<b>Figure 2.5</b> (a) The fullspace model. (b) Analytical solution to the model in (a). (c) absolute difference between (b) and the numerical solution using Fourier coefficients from Xu et al (2000). (d) absolute difference between the solution in (b) and the numerical solution using our optimized Fourier coefficients.....	<b>25</b>
<b>Figure 3.1</b> A breakdown of the components that make up the ‘para’ structure. All entries in ‘para’ are user defined, and must be entered before the ‘MTX’ structure can be created.....	<b>39</b>
<b>Figure 3.2</b> A breakdown of the components in the ‘MTX’ structure. The total structure is built in two stages, the first is created using the function generateMTX.m; the second part is created in the beginning of InvMainN.m.....	<b>40</b>
<b>Figure 3.3</b> A schematic of the surface field experiment. Blue electrodes function as potential electrodes only, while the red electrodes serve as both potential and current electrodes.....	<b>49</b>
<b>Figure 3.4</b> Inversion results for surface based acquisition.....	<b>50</b>
<b>Figure 3.5</b> Schematic of the Cone-based acquisition. Blue locations are where potential measurements are made. Current electrodes are seen in red.....	<b>53</b>
<b>Figure 3.6</b> Inverse results for the Cone-based acquisition.....	<b>54</b>
<b>Figure 4.1</b> Schematics of a) a standard cone penetrometer and b) a resistivity cone. ...	<b>60</b>
<b>Figure 4.2</b> A cross-section of the Kidd2 site, with the approximate boundary of the salt water intrusion overlaid (after Neilson-Welch and Smith, 2001).....	<b>63</b>

**Figure 4.3:** Schematic of a cone-based resistivity tomography system. The current electrodes are permanently emplaced prior to C-bert testing. Potential measurements are made using the cone-mounted potential electrode and can thus be made anywhere in the volume..... **65**

**Figure 4.4** Kidd2 survey map. The surface grid consisted of 39 electrodes. The locations of the 9 permanent current electrodes are indicated by the ‘X’; the depth directly below the ‘X’ is the depth of emplacement. C-bert data were acquired at 5 locations, labeled C-bert01 through C-bert05. The maximum depths reached in the C-bert data acquisition are listed below the location. .... **68**

**Figure 4.5** (a) Schematic of Permanent electrode seated in deployment rod. (b) Permanent current electrode. .... **70**

**Figure 4.6** The RCPT data obtained from C-bert05 at Kidd2. The data are superimposed over the interpreted cross-section for the site. .... **74**

**Figure 4.7** Schematic of the iteratively determined boundary conditions approach (IDBC), using two iterations. (a) large coarse grid is defined with boundaries sufficiently far away so as not to influence the region of interest (ROI). (b) High resolution resistivity logs, or the fine scale 3D resistivity structure, are upscaled onto the coarse grid. (c) The potential field is determined at every point in the volume. (d) Fine scale grid defined with cell dimensions that are ½ of coarse grid. Potentials from the coarse grid solution (the yellow region in frame c) are interpolated onto the boundary cells of the fine grid. (e) High resolution resistivity logs are upscaled onto the new grid; however, the boundary cells remain fixed potential boundaries. (f) Final solution is computed on the fine scale grid yielding a fine scale solution in the ROI. .... **81**

**Figure 4.8** Comparison of IDBC solution versus the fully parameterized solution; the solutions are for a dipole in a homogenous 100 Ohm-m media. The geometric factor has been applied to the potential fields and thus the entire image should be 100 Ohm-m. (a) 2d slice through the center of the 3d solution using the full solution method. (b) The same slice as in (a) solved using the IDBC approach. (c) The vertically averaged resistivities from the images in (a) and (b). (d) A percent difference map between images (a) and (b). .... **82**

**Figure 4.9** (a) An example of a calibration resistivity structure. (b) Calculated data for the resistivity structure in (a). (c) A perturbed resistivity structure. (d) Data calculated for the resistivity structure in (c). .... **86**

**Figure 4.10** Results from the inversions of the Kidd2 data set. Frames (a)-(e) are slices from the 3D solution. In frames (c) and (e), the upscaled RCPT logs are superimposed over the inversion results. In the upper 10m of frame (c) there is a discrepancy between RCPT logs and the inversion results. .... **88**

**Figure 4.11** Schematic of the synthetic problem. There is a suspected leak directly

beneath the factory.....	90
<b>Figure 4.12</b> Eight permanent electrodes are placed around the perimeter of the factor. Four are situated at depths of 4m and four are placed at 8m. Eight C-bert profiles are aquired around the perimeter, as indicated by the figure. C-bert profiles were acquired to a depth of 20m. ....	91
<b>Figure 4.13</b> Inversion results for the synthetic experiment. Frames a and a' are west-east slices through the synthetic model and the inverse result, respectively. Frames b and b' are depth slices, at 6m, through the synthetic model and the inverse results, respectively. ....	93
<b>Figure 5.1</b> UBC RCPT cone. ....	101
<b>Figure 5.2</b> The forward and inversion grid. The cone is modeled at the center of the grid. ....	109
<b>Figure 5.3</b> Forward modeling results for clay layers of varied thickness. (a) the 2.5D resistivity structure used for the forward modeling. (b) 1-D resistivity profile. (c) modeled RCPT resistivity log.....	111
<b>Figure 5.4</b> Inversion results for the model in Figure 5.3. (a) the 1-D resistivity profile and the inverted profile. (c) the modeled RCPT log and the inverted log.....	112
<b>Figure 5.5</b> Forward modeling results for layers with varied conductivity. (a) the 2.5D resistivity structure used for the forward modeling. (b) the 1-D resistivity profile. (c) modeled RCPT resistivity log.....	113
<b>Figure 5.6</b> Inversion results for the model in Figure 5.5. (a) the 1-D resistivity profile and the inverted profile. (c) the RCPT log and the inverted log.....	115
<b>Figure 5.7</b> Forward modeling results for truncated clay layers. (a) the 2.5-D resistivity structure used for the forward modeling. (b) the 1-D resistivity profile. (c) modeled RCPT resistivity log.....	117
<b>Figure 5.8</b> Inversion results for the model in Figure 5.7. (a) the 1-D resistivity profile and the inverted profile. (c) the RCPT log and the inverted log.....	119
<b>Figure 5.9</b> RCPT logs from the Kidd2 site. ....	120
<b>Figure 5.10</b> Inversion results for KIDD2 data. The red line corresponds to a discretization of 2.5cm. The green line corresponds to a discretization based on SBT. (a) The inverted 1-D resistivity profiles. (b) the measured RCPT log, and the calculated RCPT logs obtained from the inversion.....	123

# CHAPTER 1

## INTRODUCTION

---

Obtaining accurate models of the subsurface is a key component in developing cost-effective and efficient clean-up strategies for contaminated sites. Ideally these models need to contain information about the location and extent of contaminants along with information about the subsurface architecture that governs the long-term fate and transport of contaminants. In-situ measurements, often made in boreholes, are commonly sparsely distributed, and thus provide only limited information about the subsurface region of interest. Geophysical measurements are potentially very useful for supplementing these traditional forms of measurements. Geophysical measurements are spatially exhaustive and can be acquired at relatively low cost. Of particular use for studying contaminated sites are electrical resistivity measurements. These measurements can be used to produce maps of electrical resistivity, or its inverse, electrical conductivity. These maps have been used in a variety of ways, for example, to infer the presence of contaminants with electrical conductivity different from that of the background environment (e.g LaBrecque and Yang, 2001; Daily and Ramirez, 1995) and to obtain information about potential flow paths by imaging the movement of conductive tracers (Versteeg et al, 2000; Slater et al, 2000; Kemna et al, 2002; Slater, 2002; Singha and Gorelick, 2005).

Although electrical resistivity methods have been successfully used for imaging the subsurface, there still remains need for further refinement of this geophysical technique to provide more detailed and reliable subsurface conductivity images. The focus of this thesis is to move forward the “state of the science” of electrical resistivity imaging. At the core of this work is the development and successful field testing of a cone-based electrical resistivity tomography (C-bert) system. This system combines the benefits of the minimally invasive resistivity cone penetration test (RCPT) with the 3-D imaging capabilities of electrical resistivity measurements. The development of this integrated system has required the development of new forward modeling and inversion

algorithms for these data. This dissertation consequently has considerable focus on numerical modeling of electrical resistivity data.

This dissertation is separated into six chapters. Chapters 2 through 5 have been prepared as stand-alone papers for submission to peer-reviewed journals. As such, each of these chapters contains an abstract, introduction and conclusion. However, the references for each chapter have been consolidated and appear at the end of the thesis.

Chapter 2 focuses on the development of a 2.5-D forward modeling algorithm for electrical resistivity modeling. This algorithm uses a novel boundary condition and source singularity correction. Boundary effects and the effects of source singularities contribute significant error to numerical solutions. The correction I present largely eliminates these errors. Furthermore, in this chapter I develop an optimization scheme for determining the Fourier coefficients that are used in the 2.5-D approximation. The algorithm was implemented as an open source MATLAB package. Chapter 2 has been submitted for publication to *Computers in Geosciences* (Pidlisecky and Knight, 2006).

In Chapter 3, I document the development of an open source 3-D DC resistivity inversion package. The code was developed because of an absence of open source inversion software that is flexible and can allow for inverting non-standard geometries; This is a critical issue when developing new methodologies, such as the C-bert. The implementation incorporates many improvements over existing algorithms. In particular, I apply a 3-D version of the boundary correction/ source singularity correction developed in Chapter 2. Using this correction greatly decreases the computational time required to solve the 3-D problem. Furthermore, the algorithm can be used to invert data acquired from any combination of acquisition geometries, including a combination of surface and borehole electrodes. The code also allows for the addition of other data as hard and soft constraints in the inversion. This is a key feature required for the development of C-bert, as RCPT data can be directly incorporated into the inversion of C-bert data. This paper is in review for publication in *Geophysics* (Pidlisecky, Haber and Knight, 2006).

Chapter 4 documents the development and testing of the cone-based electrical resistivity imaging system. Field equipment and procedures are described in detail. A C-bert data set was acquired at the Kidd2 research site in Richmond, British Columbia. The data were processed using the inversion algorithm described in Chapter 3. Inversion of

these data proved difficult due to the effect of the highly conductive cone on the measured potential field. This necessitated the development of a cone correction technique to correct for the effect of the cone. The correction was done in a computationally efficient manner through the use of a new forward solver developed for this problem. This highly efficient solver made the cone correction computationally tractable. I demonstrated, by way of a successful field experiment and a numerical example, that C-bert has the potential to be a very useful technology for near-surface imaging. This chapter has been accepted for publication in *Geophysics* (Pidlisecky, Knight and Haber, 2006).

Chapter 5 concerns modeling and inversion of RCPT logging data. As a result of disparities between the RCPT logs and inverted images from the C-bert experiment, I endeavored to answer the question: what is the RCPT log really measuring? RCPT logs, which are high resolution resistivity logs, are often taken as being representative of the “true” in-situ resistivity structure. However, in this work I demonstrated that the RCPT log is a non-linear average of the subsurface resistivity structure. This averaging is a function of both the in-situ conductivity structure and the resistivity tool geometry, and results in resistivity logs that incorrectly predict the in-situ resistivity values. Based on the 2.5-D algorithm developed in Chapter 2, I developed an approach to modeling a RCPT resistivity log for a given tool geometry. I also developed an inversion routine that allows for the recovery of the layered resistivity structure that gives rise to observed RCPT logs. Using this inverse approach, one can obtain resistivity models that are not affected by the averaging of the tool, and are thus independent of tool geometry. This is in preparation for submission to *Geotechnique* (Pidlisecky, Knight, and Howie, 2006).

Chapter 6 presents a summary of the key contributions of this thesis and outlines some avenues of future research that build on this work.

## CHAPTER 2

# AN IMPROVED 2.5-D ELECTRICAL RESISTIVITY MODELLING ALGORITHM

### Abstract

---

We present a 2.5-D forward modeling algorithm for electrical resistivity data. The algorithm incorporates a novel boundary condition and source singularity correction that greatly reduces the need to pad the model space. The correction is computationally efficient and highly effective. In addition, the algorithm includes an improved optimization method for estimating the appropriate Fourier coefficients to achieve an accurate 2.5-D approximation. The optimization scheme uses a regularized gradient-based search to find the optimal coefficients. We compare results from our algorithm to two analytical solutions. We are able to achieve errors on the order 1% when compared to these models. We have implemented the algorithm as an open source MATLAB based forward modeling package. The MATLAB code is useful for exploring subsurface current flow. It has been coded so that it can be easily ported to work with inversion routines. The code is computationally efficient and suitable for solving 2-D problems with more than of 250,000 model parameters.

## 2.1 Introduction

---

Electrical resistivity imaging (ERI) is being increasingly used for a wide range of applications in earth sciences. In contaminant hydrology, results from ERI surveys have been interpreted to infer the presence of contaminants, (e.g. LaBrecque, 2001; Daily and Ramirez, 1995) and to obtain information about potential flow paths (Versteeg et al., 2000; Slater et al., 2000; Kemna et al., 2002; Slater, 2002; Singha and Gorelick, 2005). Resistivity imaging has also been used in mining applications to gain geologic insight and to monitor mine drainage (Oldenburg et al., 1997; Yuval and Oldenburg, 1996).

Given the type and number of field applications of ERI, there is growing need for the ability to rapidly invert the acquired data. Because most of the computational time in an inversion is spent solving the forward model, the real need is for an accurate and efficient forward modeling algorithm. This is particularly true for recently developed inversion methods involving stochastic techniques (Malinverno and Torres-Verdin, 2000; Andersen et al., 2001; Yeh et al., 2002; Ramirez et al., 2005). While these techniques have the advantage of yielding an estimate of error in the obtained model, they can require the forward problem be solved thousands of times. A computationally expedient forward modeling algorithm is essential to furthering research into these new inversion methods.

One challenge in developing efficient forward modeling capabilities is the 3-D nature of electrical current flow. In many geological situations, however, we can assume that the subsurface conductivity structure is invariant in one dimension. With this in mind, Dey and Morrison, (1979) developed a 2.5-D modeling algorithm. In this approach, the geology is described as two dimensional, but through an approximation in the third dimension, the algorithm considers current flow in all three dimensions. This technique is potentially a very efficient way for solving the forward problem. It provides the accuracy required for the inversion of field data, while being only marginally more expensive than solving the 2-D problem.

We have developed a MATLAB-based 2.5-D forward modeling code, based on the Dey and Morrison (1979) algorithm, that is completely open source and easy to read.

The code improves on existing algorithms in two main ways. First, we employ a novel optimization routine that minimizes the effect of approximating current flow in the third dimension. Second, we employ a new correction term that greatly reduces boundary effects and source singularity effects. The code is highly efficient, and can be easily integrated with resistivity inversion algorithms. We have optimized the code where possible, while retaining readability and usability. The code has multiple user-controlled options that balance computational efficiency and solution accuracy. Here we present the theory behind the forward problem, describe the pertinent details of our implementation and present examples that demonstrate the utility of the code.

## 2.2 The Forward Problem

---

### 2.2.1 Governing equations

The 3-D potential field due to a known input current is related to the conductivity structure, for appropriate boundary conditions, as described by equation 2.1:

$$-\nabla \cdot \sigma(x, y, z) \nabla \phi(x, y, z) = I(\delta(\mathbf{r} - \mathbf{r}_+) - \delta(\mathbf{r} - \mathbf{r}_-)). \quad (2.1)$$

where  $\phi$  is the potential field,  $I$  is the input current from a dipole, and  $\sigma$  is the conductivity structure of the medium. Here,  $\mathbf{r}_+$  and  $\mathbf{r}_-$  are the locations of the positive and negative current sources, respectively, and  $\delta(\mathbf{r} - \mathbf{r}_+)$  is the dirac delta function, centered at the current source location. If we assume  $\frac{d}{dy} \sigma(x, y, z) = 0$ , equation 2.1 can be rewritten as follows:

$$-\nabla \cdot \sigma(x, z) \nabla \phi(x, y, z) = I(\delta(\mathbf{r} - \mathbf{r}_+) - \delta(\mathbf{r} - \mathbf{r}_-)). \quad (2.2)$$

Dey and Morrison (1979) demonstrated that equation 2.2 can be efficiently solved in the Fourier domain. The forward and inverse Fourier cosine transforms are defined, respectively, as follows:

$$\tilde{f}(x, k_y, z) = \int_0^\infty f(x, y, z) \cos(k_y y) dy \quad (2.3)$$

and

$$f(x, y, z) = \frac{2}{\pi} \int_0^\infty \tilde{f}(x, k_y, z) \cos(k_y y) dk_y \quad (2.4)$$

where  $k_y$  is the wave number. Applying the forward transform to equation 2.2 we obtain a solution for the 2-D transformed potential:

$$-\nabla \cdot \sigma(x, z) \nabla \tilde{\phi}(x, k_y, z) + k_y^2 \cdot \sigma(x, z) \cdot \tilde{\phi}(x, k_y, z) = \frac{I}{2}(\delta(\mathbf{r} - \mathbf{r}_+) - \delta(\mathbf{r} - \mathbf{r}_-)). \quad (2.5)$$

where  $\tilde{\phi}$  is the transformed 2-D potential. In matrix notation, we can write equation 2.5 as follows:

$$(\mathbf{D} \cdot \mathbf{S}(\sigma) \cdot \mathbf{G} + k_y^2 \cdot \mathbf{S}(\sigma)) \tilde{\mathbf{u}} = \mathbf{A}(\sigma, k_y^2) \tilde{\mathbf{u}} = \mathbf{q}. \quad (2.6)$$

Here,  $\mathbf{D}$  and  $\mathbf{G}$  are matrices representing 2-D, divergence and gradient operators, respectively;  $\mathbf{S}(\boldsymbol{\sigma})$  is a diagonal matrix containing the conductivity values;  $\tilde{\mathbf{u}}$  is a vector containing the transformed potentials;  $\mathbf{A}(\boldsymbol{\sigma}, k_y^2)$  is the forward operator matrix; and  $\mathbf{q}$  is a vector containing the locations of the positive and negative current sources. From equation 2.6 we see that if we wish to predict the transformed potentials for a given conductivity model and wave number, we must solve the following equation:

$$\tilde{\mathbf{u}} = \mathbf{A}(\boldsymbol{\sigma}, k_y^2)^{-1} \mathbf{q}. \quad (2.7)$$

Practically speaking, we are interested in the potential distribution,  $\mathbf{u}$ , and not the transformed potential,  $\tilde{\mathbf{u}}$ . Therefore we must perform an inverse Fourier transform to obtain  $\mathbf{u}$ . However, because we are solving equation 2.7 discretely, we only solve for a finite number of  $k$  values. We approximate the inverse Fourier transform described by equation 2.4 with the following ( $y = 0$ ):

$$\mathbf{u} = \frac{2}{\pi} \sum_{i=0}^n \tilde{\mathbf{u}}(\boldsymbol{\sigma}, k_i^2) g_n \quad (2.8)$$

where  $n$  is the number of wavenumbers and  $g_n$  are the summation weights for each wavenumber. In order to solve for the potential in an efficient manner, we want to minimize the number of times we solve equation 2.7, i.e. we want to minimize the number of wavenumbers we solve for. We therefore need to make judicious choices as to which wavenumbers we should solve for, and what the associated summation weights should be. In a subsequent section, we document a method for optimizing the choice of both the wavenumbers and the weights.

### 2.2.2 *Discretizing the operators*

In order to solve equation 2.7, the problem is approximated on a grid, and solved numerically. We have chosen to discretize the system using a cell-centered, variable-grid, finite volume approach, similar to that presented by Haber et al. (2000a). This approach allows us to have a reasonably flexible mesh, and is well-suited for dealing with large variations in conductivity. With this approach,  $\mathbf{D}$  and  $\mathbf{G}$  are matrices representing 2-D second order finite difference divergence and gradient operators, respectively. In equation 2.6,  $\mathbf{S}$  is a diagonal matrix that contains the harmonic average of the

conductivity of each cell face along the main diagonal; this is an appropriate way to average for the conductivity at the faces, as it corresponds to serial current flow across the faces. Figure 2.1 is a schematic of the 2-D solution grid. The resulting operators,  $\mathbf{D}$ ,  $\mathbf{G}$ , and  $\mathbf{S}$ , are all sparse and thus can be explicitly formed and stored in a computationally efficient manner. We note from equation 2.6 that, through a series of sparse matrix multiplications and matrix additions, we can create and store the forward model operator,  $\mathbf{A}(\boldsymbol{\sigma}, k_y^2)$ , for a given wavenumber.

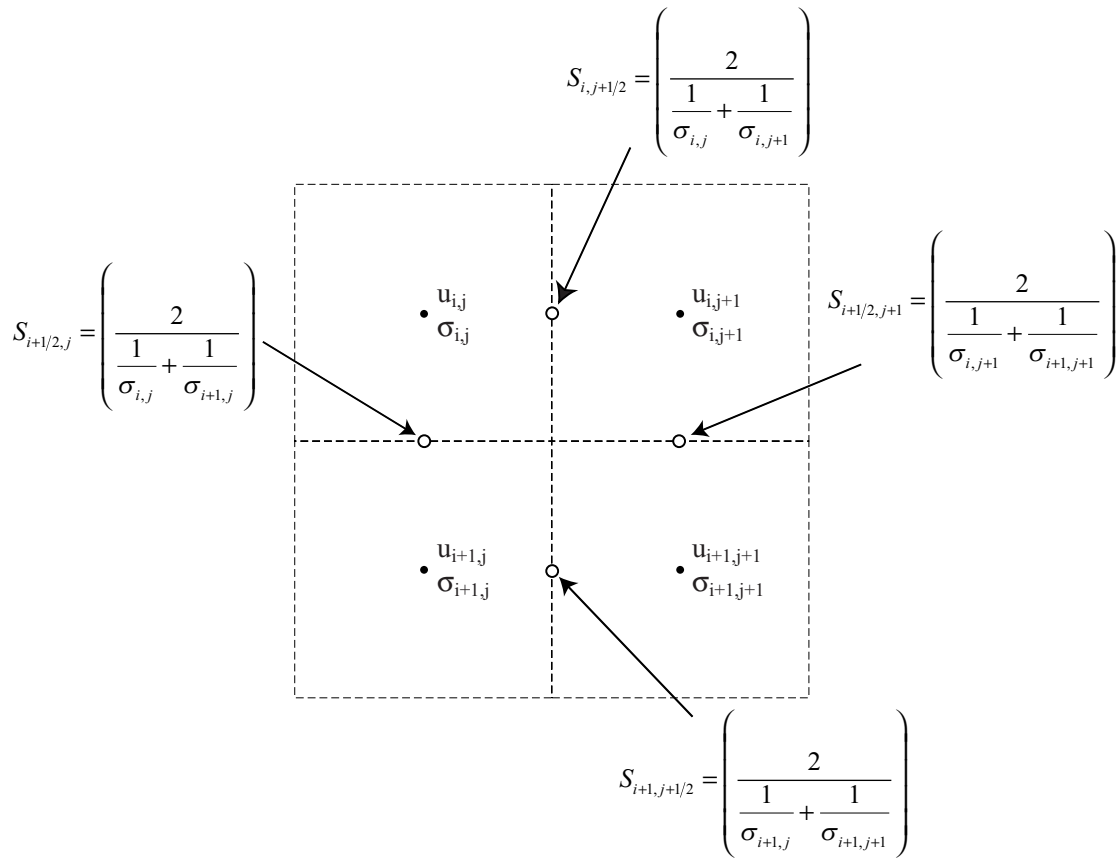


**Figure 2.1**      **The finite volume grid.**

The finite difference operators,  $\mathbf{D}$  and  $\mathbf{G}$ , are applied across the entire model space, including the boundary cells. This enforces no-flux boundary conditions (BC) at the edges of the model space. We have used these BC's for three reasons: 1) they fall out of the discretization, 2) they are numerically efficient to solve, and 3) their effects decay as  $\frac{1}{r^2}$ . Furthermore, a variable grid discretization scheme allows us to push the boundaries far away from our region of interest without creating prohibitively large models.

The source vector,  $\mathbf{q}$ , is an approximation to the delta function described in the right hand side of equation 2.5. As such,  $\mathbf{q}$  is a vector of zeros with a value of  $\frac{1}{\Delta A}$  at the positive source location and a value of  $-\frac{1}{\Delta A}$  at the negative source location, where  $\Delta A$  is the area of the cell.

### **2.2.3 Correction for BC and source singularities**

There are two issues that greatly impact the accuracy and performance of a discretized solution to the PDE in equation 2.1. The first of these is boundary effects. Although the BC's described above are a reasonable choice for this problem, they are physically unrealistic. Therefore, to reduce errors associated with the BC's, we are required to pad the model space with cells at the boundaries. Padding the model space can quickly increase the size of the model, making it computationally expensive to solve. The second issue with discretizing equation 2.2 is that singularities exist at the source locations. The potential falls off rapidly near a source and thus, if we wish to have an accurate solution near a source electrode, we must finely discretize around this location. If we do not finely discretize, we can introduce significant error in our estimate of the potential field in cells adjacent to a source.

In order to address both of these issues, we apply a correction to the source term,  $\mathbf{q}$ , that reduces the effects of the BC's, and the source singularities. To develop this solution, we substitute equation 2.7 into equation 2.8 we obtain:

$$\mathbf{u} = \frac{2}{\pi} \left[ \sum_{i=0}^n g_n \mathbf{A}(\boldsymbol{\sigma}, k_y^2)^{-1} \right] \bullet \mathbf{q}. \quad (2.9)$$

Rearranging equation 2.9 to solve for  $\mathbf{q}$ , we have:

$$\mathbf{q} = \frac{\pi}{2} \underbrace{\left[ \sum_{i=0}^n g_n \mathbf{A}(\boldsymbol{\sigma}, k_y^2)^{-1} \right]^{-1}}_{\mathbf{L}^{-1}} \bullet \mathbf{u} \quad (2.10)$$

where  $\mathbf{L}^{-1}$  is the complete forward modeling matrix (i.e. for all chosen  $k$  values). Given equation 2.10, we can see that if we know the potential field,  $\mathbf{u}$ , we can recover the source term,  $\mathbf{q}$ . We can use equation 2.10 to calculate an improved source term using the following BC/singularity correction algorithm:

1. Define a homogenous conductivity field,  $\boldsymbol{\sigma}_H$ , such that,  $\boldsymbol{\sigma}_H = \text{mean}(\boldsymbol{\sigma}_T)$ , where  $\boldsymbol{\sigma}_T$  is the total conductivity that we are solving for.
2. Calculate the analytical solution for the potential field,  $\mathbf{u}_H$ , resulting from the conductivity structure  $\boldsymbol{\sigma}_H$  using equation 2.2.
3. Construct  $n$  forward operators,  $\mathbf{A}(\boldsymbol{\sigma}_H, k_y^2)$ , where  $n$  is the number of wavenumbers.
4. Calculate  $\mathbf{L}$ , by summing the inverted operators:  $\mathbf{L} = \frac{\pi}{2} \left[ \sum_{i=0}^n g_n \mathbf{A}(\boldsymbol{\sigma}_H, k_y^2)^{-1} \right]$ .
5. Evaluate  $\mathbf{q}_{\text{corr}} = \mathbf{L}^{-1} \bullet \mathbf{u}_H$ .

Once we have the vector  $\mathbf{q}_{\text{corr}}$ , we substitute it for  $\mathbf{q}$  in equation 2.9 and solve the system,

$$\mathbf{u}_T = \frac{2}{\pi} \left[ \sum_{i=0}^n g_n \mathbf{A}(\boldsymbol{\sigma}_T, k_y^2)^{-1} \right] \bullet \mathbf{q}_{\text{corr}} \quad (2.11)$$

By generating  $\mathbf{q}_{\text{corr}}$  in this manner, we obtain a vector that is no longer just two spikes at the source locations; the new vector now contains additional information that corrects for the errors in the forward operator. The errors in the forward operators are largely a function of the BC's and the source singularity. The new source term compensates for both of these factors. We note, that for some problems, this source term correction can become computationally expensive, as step 3 of the BC algorithm requires the explicit computation of  $\mathbf{A}(\boldsymbol{\sigma}_H, k_y^2)^{-1}$  for all of the wavenumbers. However, this computational cost

is somewhat balanced by the fact that  $\mathbf{q}_{\text{corr}}$  can be calculated once, and then used for a variety of conductivity structures ( $\sigma_{\text{T}}$ 's).

#### 2.2.4 *Optimizing the choice of $k$ and $g$*

In order to solve equation 2.9 in an efficient manner, we would like to solve the equation for the smallest number of wavenumbers possible, while still obtaining an accurate solution. Xu et al. (2000), presented an optimization technique for selecting appropriate  $k$  and  $g$ . Their method centers around optimizing  $k$  and  $g$  for a point source in a homogeneous full space, and then using these  $k$  and  $g$  values to solve equation 2.9 for an inhomogeneous half space. They employed a two-step gradient-based optimization technique to calculate  $k$  and  $g$ . We have built on their work, and developed an optimization approach that uses a regularized gradient-based approach. Our approach also incorporates a line-search which helps to minimize the number of iterations required for the solution to converge. The regularization stabilizes the solution, and results in a robust algorithm. In addition, we have extended their solution to optimize for specific source and receiver locations. By doing this, we consider the current flow from dipole sources in a halfspace, rather than pole sources in a fullspace.

The potential field, due to a dipole source, in a homogeneous halfspace can be described as follows:

$$u = \frac{I}{4\pi\sigma} \underbrace{\left( \frac{1}{\|r - r_+\|} - \frac{1}{\|r - r_-\|} + \frac{1}{\|r - r_+^{im}\|} - \frac{1}{\|r - r_-^{im}\|} \right)}_{\frac{1}{R}} \quad (2.12)$$

where  $r$  is the observation location,  $(x, z)$ ;  $r_+$  is the position of the positive source term,  $(x_+, z_+)$ ;  $r_-$  is the position of the negative source term,  $(x_-, z_-)$ ;  $r_+^{im}$  is the position of the positive image term,  $(x_+, -z_+)$ ;  $r_-^{im}$  is the position of the negative image term,  $(x_-, -z_-)$ . Substituting equation 2.12 into the transform described in equation 2.3, for  $y=0$ , we obtain:

$$\tilde{u}(x, k, z) = \int_0^\infty \frac{I}{4\pi\sigma} \left( \frac{1}{\|r - r_+\|} - \frac{1}{\|r - r_-\|} + \frac{1}{\|r - r_+^{im}\|} - \frac{1}{\|r - r_-^{im}\|} \right) dy \quad (2.13)$$

solving the integral, yields:

$$\tilde{u} = \frac{I}{4\pi\sigma} \left( K_0(k\|r - r_+\|) - K_0(k\|r - r_-\|) + K_0(k\|r - r_+^{im}\|) - K_0(k\|r - r_-^{im}\|) \right) \quad (2.14)$$

where  $K_0$  is the zero-order modified Bessel function of the second kind. By applying the discrete inverse transform in equation 2.8 and rearranging variables, we obtain:

$$1 \approx \frac{2R}{\pi} \sum_{j=0}^n g_j \left( \begin{array}{c} K_0(k_j\|r - r_+\|) - K_0(k_j\|r - r_-\|) + \\ K_0(k_j\|r - r_+^{im}\|) - K_0(k_j\|r - r_-^{im}\|) \end{array} \right) = v \quad (2.15)$$

Given that we are concerned with the error at a variety of observation locations and we are interested in optimizing for  $n$  values, we can define the following system of equations:

$$\mathbf{M}\mathbf{g} = \mathbf{v} \quad (2.16)$$

where  $M_{ij} = \left( K_0(k_j\|r_i - r_+\|) - K_0(k_j\|r_i - r_-\|) + K_0(k_j\|r_i - r_+^{im}\|) - K_0(k_j\|r_i - r_-^{im}\|) \right)$ ,  $\mathbf{g}$  is a vector containing  $n$  terms. In order to minimize the error associated with our choice of  $k$  and  $g$  we seek to minimize the following objective function:

$$\Phi = \|\mathbf{I} - \mathbf{M}\mathbf{g}\| \quad (2.17)$$

where  $\mathbf{I}$  is a unit vector. We note that, in this form, equation 2.17 is a function of  $k$  and  $g$ ; however, the component associated with  $g$  is linear. We can obtain an optimal choice for

$g$ , as a function of  $k$ , by taking  $\frac{\partial}{\partial \mathbf{g}}$  of equation 2.17 and setting the derivative to zero. The

differentiation yields:

$$\frac{\partial \Phi}{\partial \mathbf{g}} = 2\mathbf{M}^T (\mathbf{I} - \mathbf{M}\mathbf{g}) = 0 \quad (2.18)$$

Rearranging equation 2.18 yields:

$$\mathbf{g} = (\mathbf{M}^T \mathbf{M})^{-1} \mathbf{M}^T \mathbf{I} \quad (2.19)$$

substituting this into equation 2.17 we obtain our global objective function in terms of  $k$ :

$$\Phi = \left\| \mathbf{I} - \mathbf{M}(\mathbf{M}^T \mathbf{M})^{-1} \mathbf{M}^T \mathbf{I} \right\| = \left\| \mathbf{I} - \mathbf{v}(k) \right\| \quad (2.20)$$

Equation 2.20 is now a function of  $k$  only, however, it is a nonlinear function of  $k$ . In order to find the minimum of equation 2.20, we linearize around a starting point  $\mathbf{v}(\mathbf{k}_0)$  and iteratively solve for the best  $k$  values. However, as noted above, we create  $\mathbf{M}$  for a variety of  $r$  values, and thus the problem is overdetermined. In addition, because the  $k$  values vary over orders of magnitude, and the Bessel function,  $K_0$ , is small for large values of  $k \left\| r - r_{src} \right\|$ , the entries of  $\mathbf{M}$  vary over orders of magnitude. These factors lead to a highly unstable optimization problem and thus we need to regularize the problem to obtain a reliable solution. Adding a regularization component to equation 2.20, and linearizing about a starting point,  $\mathbf{v}(\mathbf{k}_0)$ , we obtain:

$$\Phi = \left\| \mathbf{I} - \mathbf{v}(\mathbf{k}_0) + \frac{\partial \mathbf{v}}{\partial \mathbf{k}} \right\| + \beta \left\| \mathbf{W} \cdot \mathbf{k}_0 \right\| \quad (2.21)$$

where  $\frac{\partial \mathbf{v}}{\partial \mathbf{k}}$  is the sensitivity matrix;  $\mathbf{k}$  is a vector containing the  $k$  values; and  $\mathbf{W}$  is a model weighting matrix, in this case the identity matrix;  $\beta$  is the damping parameter, which in practice is very small, e.g.  $10^{-9}$ . Differentiating equation 2.21 with respect to  $\mathbf{k}$ , and setting the result to zero, we obtain the following  $\mathbf{k}$  update, for the  $i^{th}$  iteration:

$$\delta \mathbf{k}_i = \left( \frac{\partial \mathbf{v}^T}{\partial \mathbf{k}_i} \frac{\partial \mathbf{v}}{\partial \mathbf{k}_i} + \beta \mathbf{W} \right)^{-1} \cdot \left( \frac{\partial \mathbf{v}}{\partial \mathbf{k}_i} (\mathbf{I} - \mathbf{v}_i) + \beta \mathbf{W} \cdot \mathbf{k}_i \right) \quad (2.22)$$

We now define a new  $k$  vector for the  $i^{th} + 1$  iteration:

$$\mathbf{k}_{i+1} = \mathbf{k}_i + \alpha \delta \mathbf{k}_i \quad (2.23)$$

where  $\alpha$  is a line search parameter that ensures we take an adequate step length to reduce the value of equation 2.21 at each iteration. Once equation 2.21 is reduced to a desired tolerance, we evaluate equation 2.19, for our final  $k$  values, to obtain the optimal  $g$  values.

## 2.3 MATLAB Implementation

---

In this section we describe the pertinent details regarding our implementation of the forward modeling code. All of the source code has been developed in MATLAB. This was done for three reasons. MATLAB source code is platform independent, and thus any user can download the source code and run the driver files without any need to recompile. MATLAB code, when vectorized, yields speeds comparable with Fortran implementations of similar algorithms. MATLAB has excellent built-in graphical support, allowing the user to easily produce a variety of different 2-D renderings of the resulting potential fields. In addition, MATLAB code is relatively easy to read, so users can easily navigate the software and modify it for their own purposes.

### 2.3.1 Data structure

In our implementation, we make use of MATLAB's structure arrays. The advantage of using these data structures is that it allows one to pass a large quantity of information between functions, with only a few variable names. For this work we require the user defined structure 'Para' for the forward code to operate. 'Para' contains most of the information needed to run the forward model; the only additional input is the 2-D conductivity structure that is being modeled. Figure 2.2 outlines the components of 'Para'.

'Para' is created by calling the function, *get\_2\_5Dpara.m*. There are seven inputs to the function call, five required and two optional. The required inputs are: source electrode positions, the x-direction discretization, the z-direction discretization, an on/off toggle for applying the BC/singularity correction and an entry for the desired number of Fourier coefficients. The optional inputs are: receiver electrode locations, and a vector with the source number that corresponds to a given receiver location.

Once 'Para' has been created, it can be saved and used repeatedly to model the potential field for different conductivity structures (given that none of the inputs are required to change). The computational time required to calculate 'Para' varies greatly

depending on the chosen inputs. If the user elects to apply the BC/singularity correction and to optimize for  $k$  and  $g$  values, generating 'Para' can take several minutes.

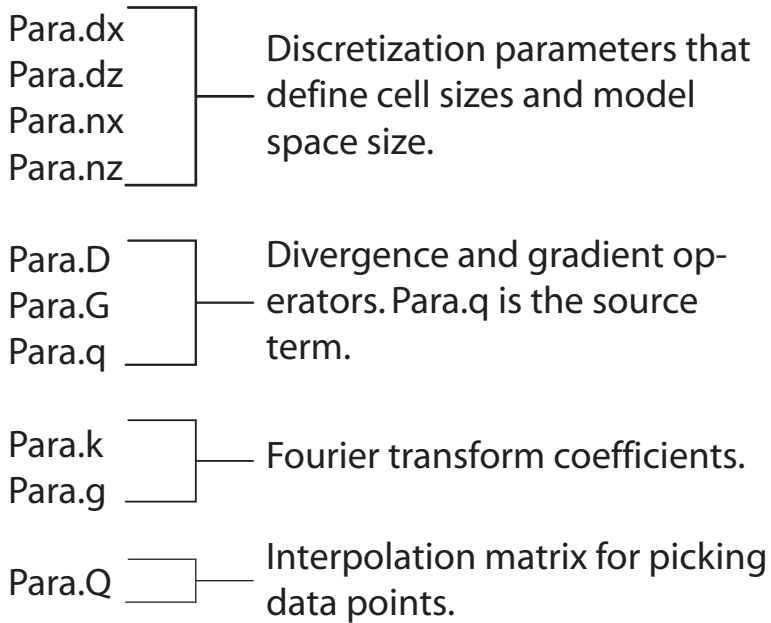


Figure 2 2 Contents of the 'Para' structure.

### 2.3.2 Calculating $\mathbf{q}$

In order to solve equation 2.9, we first need to create a right hand side source vector (or matrix for the case of multiple sources). When we are considering real world scenarios, we are often faced with constraints, such as topography and borehole deviations, that do not allow us to locate sources on a regular grid, at cell centers. Therefore, we must interpolate to cell centers. The vector  $\mathbf{q}$  is stored in the ‘Para’ structure as Para.q. We have two options for forming  $\mathbf{q}$ , one involves creating an interpolated vector that approximates a delta function at the source location. The second method is to create a corrected  $\mathbf{q}$  term as described in the BC/singularity correction section.

We first describe the formation of the  $\mathbf{q}$  matrix using interpolation; creating  $\mathbf{q}$  in this manner is done using the function call *calcRHS\_2\_5.m*. As stated earlier, if the source electrodes fall on cell centers, they are assigned values of  $\frac{1}{\Delta A}$  at the positive electrode location, and  $-\frac{1}{\Delta A}$  at the negative electrode location. If the sources are not located on a cell center, we linearly interpolate  $\frac{1}{\Delta A}$  for the positive source and  $-\frac{1}{\Delta A}$  for the negative source, to the four surrounding cell centers. For sources located at the surface where the z-coordinate equals zero, the data are assigned a z-coordinate that corresponds to the center of the first cell in the z direction. The surface data are then interpolated to the two adjacent cells in the x direction.

The second method for creating  $\mathbf{q}$  is to call the function, *BC\_sing\_2\_5.m*. This function performs the BC/singularity correction described in the earlier section. The  $\mathbf{q}$  term is created by multiplying our forward operator by the analytical potential field. Because the analytical potential field is calculated using the exact location of the source electrodes, there is no need to interpolate, as the new  $\mathbf{q}$  implicitly accounts for sources being off of cell centers. Figure 2.3 shows the source term, in map view, for two source dipoles. Figures 2.3a, 2.3b and 2.3c consider a source dipole where the sources are located on cell centers. In Figure 2.3a and 2.3b we see the results of using interpolation and the BC/singularity correction, respectively. As can be seen in Figure 2.3b, the

BC/singularity correction adds information to the source term. Figure 2.3c is a difference image from Figures 2.3a and 2.3b; it further highlights the difference between the  $\mathbf{q}$  terms. Figures 2.3d and 2.3e consider a dipole where the electrodes are slightly off the cell center. In Figure 2.3d we see that the source term has been interpolated to adjacent cells. In Figure 2.3e we see that the BC/singularity correction has accounted for the shift in the source. Figure 2.3f is a difference image from Figures 2.3d and 2.3e.

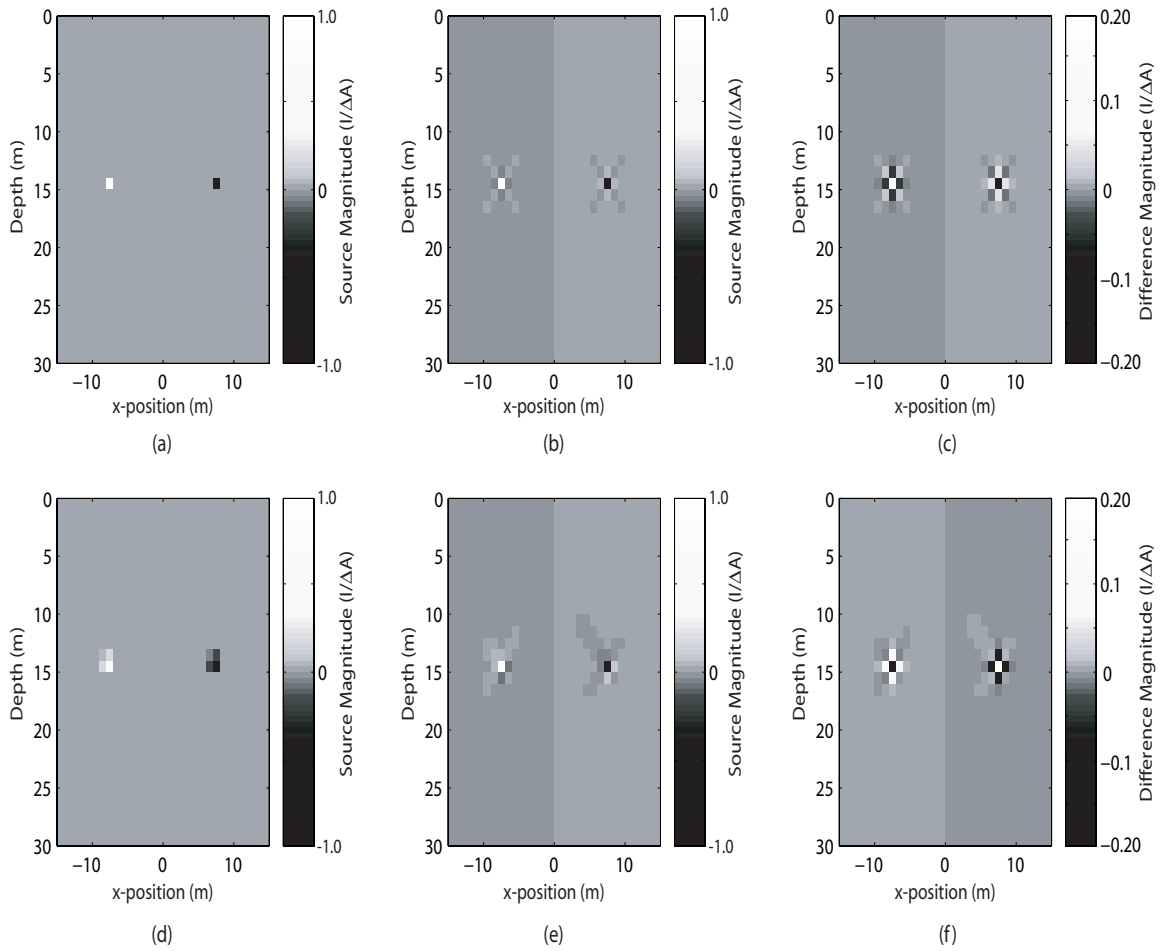


**Figure 2.3** Map view representations of the  $q$  vector. (a) the  $q$  term with sources located at cell centers. (b) BC/singularity correction applied to the source term used in (a). (c) difference map of (a) and (b). (d) interpolated  $q$  term. (e) BC/singularity correction applied to the source term used in (d). (f) difference image of (d) and (e).

### 2.3.3 Calculating $k$ and $g$

The function `get_k_g_opt.m` calculates the optimized values of  $k$  and  $g$  for a given survey geometry. The call to this function takes place in `get_2_5Dpara.m`. The code optimizes the choice of  $k$  and  $g$ , for a given number of coefficients,  $n$ , based on the acquisition geometry of the survey. The code solves the optimization problem, for all the user defined source locations, over a subset of the model space (i.e. a limited number of  $r$  values). As mentioned earlier, the problem is overdetermined, and thus solving for all observation points adds little to solution, while increasing the computational cost of the optimization.

$N$	$\Phi_0$	$\Phi_{\text{final}}$
1	88	1.34
2	7.1	0.040
3	0.22	5.9e-4
4	3.8e-3	1.6e-4
5	9.6e-5	9.6e-5*
6	1.5e-4	3.4e-7
7	1.2e-4	6.7e-7
8	7.2e-5	6.7e-9

**Table 2.1. Starting and final objective function values for a variety of  $n$  values. \*For  $n = 5$  the starting point is a minimum and thus the optimization does not improve the estimate of  $k$  and  $g$ .**

Table 2.1 presents results for a series of optimizations for a range of  $n$  values. The source configuration that was optimized is the same as the one shown in Figure 2.3a. The model space spans 30m x 30m with 1m cell dimensions. This grid results in 898 possible observation locations. The optimization takes place over a subset of 100 of these locations. We note that increasing  $n$  increases the computational time of the forward problem, and thus we want to use the minimum number of coefficients possible. Our work suggests that using between four and six coefficients will produce reasonable modeling results.

### 2.3.4 Solving the Forward Problem

As seen in Figure 2.2, the gradient and divergence operators are created within the function call `get_2_5Dpara.m` and stored in 'Para'. These operators,  $\mathbf{D}$  and  $\mathbf{G}$ , are

generated by *div2.m* and *grad2.m*, respectively. Within *dcfw\_2\_5D.m* we create our  $\mathbf{S}$  matrix, for a given  $k$  value, with the function *massf2.m*. The three resulting sparse matrices,  $\mathbf{D}$ ,  $\mathbf{G}$ , and  $\mathbf{S}$ , are multiplied together to yield the forward modeling matrix,  $\mathbf{A}$ . Once  $\mathbf{A}$  has been created, we solve equation 2.7 for  $\tilde{\mathbf{u}}$ .  $\mathbf{S}$  is then updated for a new  $k$  value,  $\mathbf{A}$  reformed, and equation 2.7 solved once again. Once we have  $\tilde{\mathbf{u}}$  for all the  $k$  values, we evaluate equation 2.8 to obtain  $\mathbf{u}$ . Because the  $\mathbf{A}$  matrix is sparse and banded, we use the built in MATLAB matrix solver for efficiently solving the linear system described in equation 2.7.

### 2.3.5 Picking data

In order to make this package more convenient for coupling to inversion codes, we have included an option that allows the code to output the data that a given survey geometry (i.e. source and receiver locations) would yield. In practice, the data that we observe are likely a subset of the entire potential field we solve for. In addition, we often acquire data with receivers not located at cell centers. In matrix notation, we can define our observed data as follows:

$$\mathbf{d}_{\text{obs}} = \mathbf{Q} \cdot \mathbf{u} \quad (2.24)$$

where  $\mathbf{Q}$  is the projection matrix.  $\mathbf{Q}$  is generated, for a given series of receiver locations, in *get\_2\_5Dpara.m*.  $\mathbf{Q}$  is calculated in a similar manner to  $\mathbf{q}$  when the interpolation option is chosen. If a receiver is not located at a cell center, we linearly interpolate to the four surrounding cells. This results in a row entry in  $\mathbf{Q}$  that has four weighting values; these values are the weighted contribution of the surrounding four cells to the off-center datum. For data located at the surface where the z-coordinate equals zero, the data are assigned a z-coordinate that corresponds to the center of the first cell in the z direction. The surface datum is the interpolated value from the two surrounding cells. In this case the corresponding row of  $\mathbf{Q}$  has two data weights. If the datum lies at a cell center, the resulting row entry in  $\mathbf{Q}$  is simply one at the datum location. Within the call to *dcfw\_2\_5D.m*, equation 2.24 is evaluated to yield  $\mathbf{d}_{\text{obs}}$ .

## 2.4 Examples

---

In order to evaluate the effectiveness of our modeling routine we present two examples that compare our numerical results to those from analytical solutions.

### ***2.4.1 A surface survey of layered media.***

Our first example models the surface potential, due to a surface current dipole, over a layered medium. The analytical solution to this situation is found in Telford et al. (1998). The model that is considered can be seen in Figure 2.4. The first layer in the subsurface is 10m thick, with a conductivity of 1 S/m. The second layer, from 10 to 30m, has a conductivity of 100 S/m. In the analytical solution, the second layer is assumed to extend to infinity. For the numerical solution, we solved the problem on a 30 x 30 grid. The cell dimensions were 1m x 1m. The current electrode locations (i.e. source locations) can be seen in the figure. In Figure 2.4 we present three solutions: 1) the analytical solution, 2) the numerical solution using the Fourier coefficients presented by Xu et al. (2000), and 3) our solution using the BC/singularity correction and optimized  $k$  and  $g$  values. As can be seen from the figure, our solution does an excellent job of matching the analytical solution at almost all points. The Xu et al. (2000) solution does a reasonably good job of matching analytical solution, however, there is measurable error at the current electrode locations and model boundaries. As can be seen in our solution this error is absent. This is primarily due to our BC/singularity correction. We note that for this example, if we applied our BC/singularity correction to the Xu et al. (2000) solution, we would greatly improve the solution. In the next section we apply the BC/singularity correction to the Xu et al. (2000) solution in order to evaluate the benefit of our optimization routine for  $k$  and  $g$ .

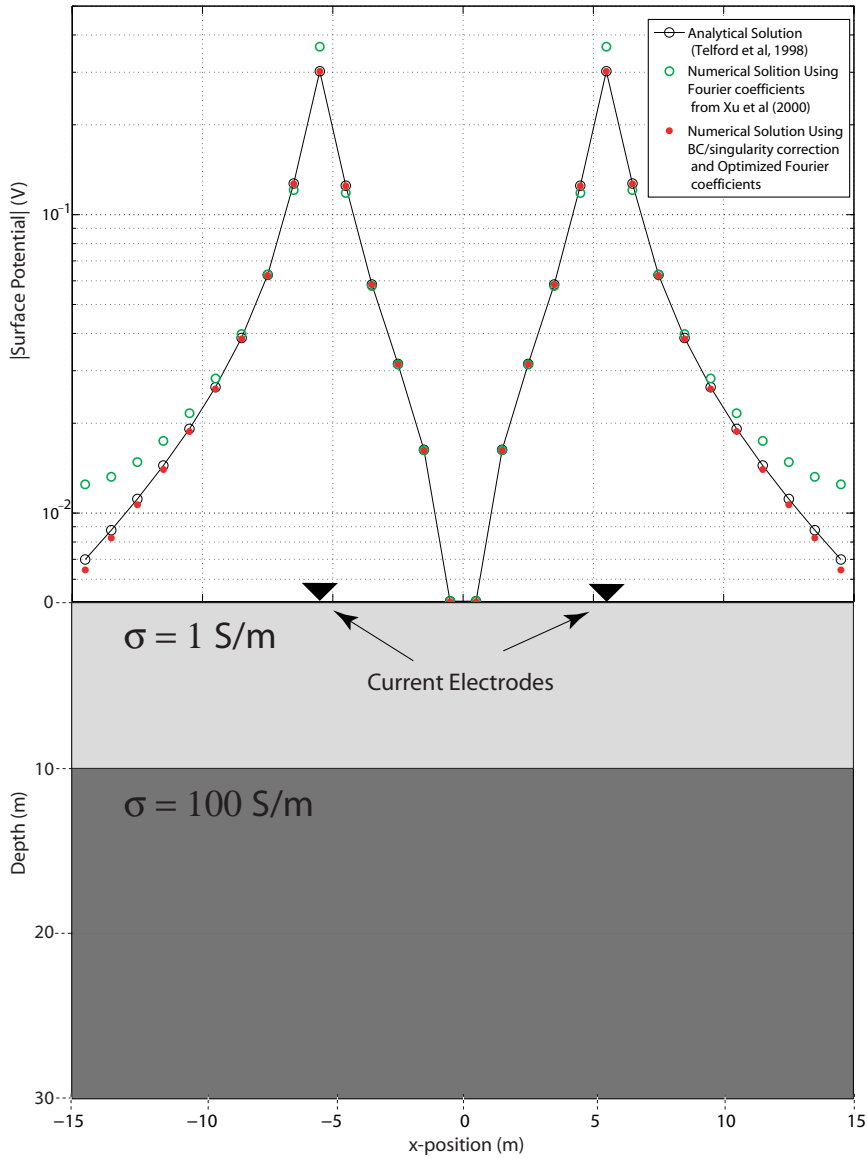


**Figure 2.4 Upper:** The data obtained at the surface from the analytical model, the solution of Xu et al., and our solution using both optimized  $k$  and  $g$  values and the BC/singularity correction. **Lower:** The model of 2 layers with current electrodes at the surface.

### ***2.4.2 Fullspace Solution***

Our second example considers the potential field through a 2-D slice of a 3-D fullspace. As seen in Figure 2.5a, the fullspace is separated into two half spaces of different conductivities. There is a dipole current source, oriented parallel to the boundary of the half spaces. The halfspace in the negative  $z$  region has a conductivity of 1 S/m, while the other halfspace has a conductivity of 100 S/m. An analytical solution to this problem can be found in Jackson, 1975. For the theoretical solution, the halfspaces extend to infinity in all directions. For the computational solution, we solve the problem using a variable grid discretization and push the boundaries out to approximately 150m in all directions. This yields a model space that is 45 x 44 cells. The region presented in the figure, occupies a 25 x 24 cell space with 1m discretization. Figure 2.5b is the analytical solution for this problem. Figure 2.5c is a map of the absolute error, in percent, between the analytical solution and the Xu et al. (2000) solution coupled with our BC/singularity correction. The improved Xu et al. (2000) solution shows good agreement, having a RMS error of 1%. The maximum error is approximately 4% at the interface of the two halfspaces. Figure 2.5d is a map of the absolute error between the analytical solution and a numerical solution that uses our BC/singularity correction and four Fourier coefficients that were optimized using our technique. As can be seen in Figure 2.5d our solution yields excellent agreement with the analytical solution. The RMS error is 0.4% and the maximum error is approximately 1%. We note that this is a marginal improvement over the solution of Xu et al., however, there is little additional computational cost with our approach.

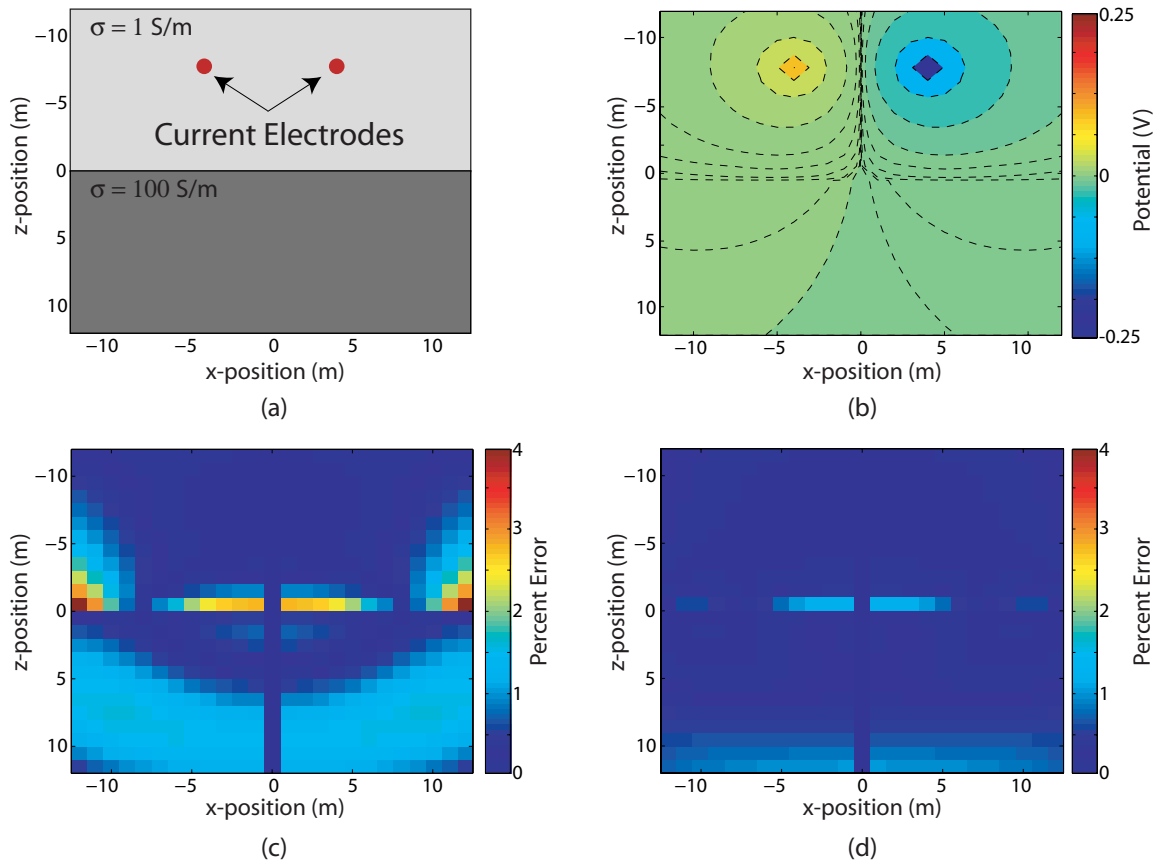


**Figure 2.5** (a) The fullspace model. (b) Analytical solution to the model in (a). (c) absolute difference between (b) and the numerical solution using Fourier coefficients from Xu et al (2000). (d) absolute difference between the solution in (b) and the numerical solution using our optimized Fourier coefficients.

## 2.5 Summary and Conclusions

---

We have developed an improved 2.5-D forward modeling algorithm, and have developed a MATLAB modeling package based on this algorithm. The improved algorithm presents a novel, highly effective, boundary condition and source singularity correction. This correction greatly decreases the errors associated with boundary effects, and thus reduces the need to pad the model space. The correction factor also increases model accuracy near the source locations. Our algorithm also includes an improved optimization scheme for selecting the Fourier wavenumbers that are used for approximating current flow in the third dimension. We have compared our modeled results to two analytical solutions. The comparisons demonstrate that using optimized Fourier coefficients, and the BC/singularity correction improves the accuracy of our numerical model with little added computational cost.

The algorithm has been implemented as a MATLAB 2.5-D DC resistivity forward modeling. The code is useful for exploring and understanding subsurface current flow. Moreover, it is well suited for coupling with new inversion routines. We have paid particular attention to implementing the code in a computationally efficient manner, and thus have achieved computational speeds that are comparable to implementations in Fortran. The code is easy to read, and users will find it easy to modify. We hope this code will be a useful tool for furthering the development of electrical resistivity imaging.

## CHAPTER 3

# A 3-D DC RESISTIVITY INVERSION

## ALGORITHM

### Abstract

---

We present an open source 3-D, MATLAB-based, resistivity inversion package. The package uses a finite volume discretization to solve the forward partial differential equation. We include a highly efficient approach to reducing boundary effects and source electrode singularities. Solving of the forward problem is achieved by using a preconditioned bi-conjugate stabilized gradient method. For the inversion algorithm we have implemented an Incomplete Gauss-Newton solver, with the model update being calculated using a preconditioned conjugate gradient algorithm. Default regularization is based on zeroth and first order Tikhonov. However, regularization type and magnitude can easily be changed. The code also has functions to include topography and constraints such as borehole logs. We include two synthetic examples that demonstrate the usefulness of this code.

## 3.1 Introduction

---

3-D DC resistivity imaging is a geophysical method that is being increasingly used to assist hydrologists, engineers and geologists in the development of subsurface models. This method involves injecting current through a pair of electrodes, either on the surface or in boreholes, and measuring the resulting potentials at numerous (tens to hundreds of) electrodes located on the surface or in boreholes. The measurements yield values of resistance that can be inverted to determine the subsurface electrical resistivity structure. The electrical resistivity structure has been used, for example, to infer the presence of a contaminant, with electrical resistivity different from that of the background environment, (e.g LaBrecque and Yang, 2001; Daily and Ramirez, 1995) and to obtain information about potential flow paths of contaminants by imaging the movement of conductive tracers (Versteeg et al., 2000; Slater et al., 2000; Kemna et al., 2002; Slater, 2002; Singha and Gorelick, 2005). Resistivity imaging has also been used in mining applications to provide geologic insight and to monitor mine drainage, (Oldenburg et al. 1997; Yuval and Oldenburg, 1996).

Inversion of resistivity data is a critical and challenging step if one desires to use the resulting images in a quantitative way. In particular, challenges exist because, the inversion problem is non-linear, ill-conditioned and underdetermined. Furthermore, because we are working in 3-D, the problems are often quite large. There are a few commercial inversion codes available and a small number of academic codes. However none of these inversion codes are open source, and are thus, to some degree, a “blackbox”. Although these codes are often successfully used in practice, we felt that for researchers it would be useful to introduce an open source code that would allow the user to control all aspects of the inversion. Of particular importance is the ability to control the type and magnitude of regularization. These inverse problems are highly underdetermined, so regularization is an important part in the solution. Thus, if quantitative interpretation of the results is desired, the effect of regularization must be understood. In addition, we wanted to develop a code that would allow researchers to experiment with novel acquisition geometries.

Resistivity inversion is one example of inversion of an elliptical partial differential equation. As such, the code has an educational role. Working with resistivity inversion can help researchers understand the elements needed for the other types of non-linear inverse problems. In particular, many equations in earth sciences, such as Maxwell's equations, the acoustic wave equation, and the ground water flow equation, share common traits with the resistivity problem. Many components of the code we developed can easily be converted to help solve inverse problems that consider these equations.

We have developed a MATLAB-based 3-D inversion code, that is completely open source and easy to read. Moreover, it is extremely flexible in terms of both acquisition geometries as well as regularization. The code is efficient enough to solve moderate size inverse problems. We have optimized the code as much as possible, while striving to retain readability and usability. Nevertheless, we have made a few choices that make the code run more slowly in some practical cases. These choices were made in order to keep its applicability as general as possible. If the user desires, the code can easily be modified to increase the efficiency for a specific problem.

Here we present the theory behind the forward and inverse algorithms, describe the pertinent details regarding our implementation and present two synthetic examples that demonstrate the utility of this code.

## 3.2 Theory

---

### 3.2.1 The forward problem

#### 3.2.1.1 Governing equations

DC resistivity and electrical resistivity tomography experiments yield a series of voltage measurements in response to a series of known input currents. These voltages and currents are related to the subsurface conductivity structure via the following relationship:

$$\nabla \cdot -\sigma \nabla \phi = I(\delta(\mathbf{r} - \mathbf{r}_{s+}) - \delta(\mathbf{r} - \mathbf{r}_{s-})) \quad (3.1)$$

with appropriate boundary conditions. Equation 3.1 is the partial differential equation that relates the potential field ( $\phi$ ) to the input current ( $I$ ), from a dipole, through the conductivity structure of the medium ( $\sigma$ ). Here,  $\mathbf{r}_{s+}$  and  $\mathbf{r}_{s-}$  are the locations of the positive and negative current sources, respectively, and  $\delta(\mathbf{r} - \mathbf{r}_s)$  is the dirac delta function, centered at the current source location.

In matrix notation, we can write equation 3.1 as follows:

$$(\mathbf{D} \cdot \mathbf{S}(\sigma) \cdot \mathbf{G}) \mathbf{u} = \mathbf{A}(\sigma) \mathbf{u} = \mathbf{q}. \quad (3.2)$$

Here,  $\mathbf{D}$  and  $\mathbf{G}$  are matrices representing 3-D divergence and gradient operators, respectively;  $\mathbf{S}(\sigma)$  is a diagonal matrix containing the conductivity values;  $\mathbf{u}$  is a vector containing the potentials;  $\mathbf{A}(\sigma)$  is the complete forward operator matrix; and  $\mathbf{q}$  is a vector containing the locations of the positive and negative current sources. From equation 3.2 we see that if we wish to predict the voltages for a given conductivity model, we must solve the following equation:

$$\mathbf{u} = \mathbf{A}(\sigma)^{-1} \mathbf{q}. \quad (3.3)$$

Equation 3 yields the potential everywhere in the 3-D volume. However, our data are likely a subset of these potentials and thus we define a projection matrix,  $\mathbf{Q}$ , for selecting data points from the volume. This results in the following equation for calculating data from the forward model:

$$\mathbf{d} = \mathbf{Q}\mathbf{u} = \mathbf{Q}\mathbf{A}(\boldsymbol{\sigma})^{-1}\mathbf{q}. \quad (3.4)$$

### 3.2.1.2 *Parameterizing the forward problem*

In order to solve 3.3, the problem is approximated on a grid, and solved numerically. We have chosen to discretize the system using a cell-centered, variable-grid, finite volume approach, similar to that presented by Haber et al. (2000a). This approach allows us to have a reasonably flexible mesh, and is well suited for dealing with large variations in conductivity. With this approach,  $\mathbf{D}$  and  $\mathbf{G}$  are matrices representing 3-D second order finite difference divergence and gradient operators, respectively. In equation 3.2,  $\mathbf{S}$  is a diagonal matrix that contains the harmonic average of the conductivity of each cell face along the main diagonal; this is an appropriate way to average for the conductivity at the faces, as it corresponds to serial current flow across the faces.

The finite difference operators,  $\mathbf{D}$  and  $\mathbf{G}$ , are applied across the entire model space, including the boundary cells. This enforces no-flux boundary conditions (BC) at the edges of the model space. We have used these BC's because: they fall out of the discretization, they are numerically efficient to solve, and their effects decay as  $\frac{1}{r^2}$ . Furthermore, a variable grid discretization scheme allows us to push the boundaries far away from our region of interest without creating prohibitively large models.

Through a series of sparse matrix multiplications, we can create and store the forward model operator,  $\mathbf{A}(\boldsymbol{\sigma})$ . We note that due to the imposed BC's the resulting forward operator has a constant null space, i.e. the solution is non-unique because it can be shifted by a constant. In order to circumvent this problem, we set the first row of the  $\mathbf{A}$  matrix to zero, except at location  $\mathbf{A}(1,1)$ , where we assign a value of  $\frac{1}{\Delta V}$ , where  $\Delta V$  is the volume of the cell. This sets the potential in this cell to zero, and removes the null space from the operator.

The source vector,  $\mathbf{q}$ , is a vector of zeros with a value of  $\frac{1}{\Delta V}$  at the positive source location and a value of  $-\frac{1}{\Delta V}$  at the negative source location. If the source is not located at a cell center, then the source values are interpolated, using linear interpolation, to the surrounding eight cell centers.

### 3.2.1.3 *Boundary conditions and source term improvement*

Although the BC's described above are a reasonable choice for this problem, they still require us to pad our model space to reduce their effects in our region of interest. Padding, even with a small number of cells, quickly increase the size of the problem when we are considering a 3-D case. We would like to improve the BC's, if it can be done in a computationally efficient manner. Another issue with this model, is that if we wish to have an accurate solution near a source electrode, we must finely discretize around the source location. Because the potential falls off rapidly near the source, there can be a significant error in our solution for the potentials near the source.

In order to address both of these issues, we apply a correction to the source term,  $\mathbf{q}$ , that both improves the BC's, and reduces errors near the source locations. The correction is obtained as follows (BC Algorithm):

1. We define a homogenous conductivity field,  $\sigma_H$ , such that,  $\sigma_H = \text{mean}(\sigma_T)$ , where  $\sigma_T$  is the total conductivity that we are solving for.
2. Calculate the analytical solution for the potential field,  $\mathbf{u}_H$ , resulting from the conductivity structure  $\sigma_H$  due to a source term  $\mathbf{q}$ .
3. Construct the forward operator  $\mathbf{A}(\sigma_H)$ .
4. Evaluate  $\mathbf{q}_{\text{corr}} = \mathbf{A}(\sigma_H) \cdot \mathbf{u}_{\text{true}}$

Once we have the vector  $\mathbf{q}_{\text{corr}}$ , we substitute it for  $\mathbf{q}$  in equation 3 and solve the system,

$$\mathbf{u}_T = \mathbf{A}(\sigma_T)^{-1} \cdot \mathbf{q}_{\text{corr}} \quad (3.5)$$

The modified vector,  $\mathbf{q}_{\text{corr}}$ , is no longer a vector with only two spikes at the source locations, it now contains additional information that corrects for the inadequacies of the forward operator,  $\mathbf{A}(\sigma_H)$ . Because  $\mathbf{A}(\sigma_H)$  is fairly similar to  $\mathbf{A}(\sigma_T)$ , the correction factor greatly reduces errors at source electrode locations, and errors associated with the

BC's for the solution to the conductivity field  $\sigma_T$ , with minimal added computational cost.

### 3.2.2 *The inverse problem*

#### 3.2.2.1 *Gauss-Newton*

From equation 3.4 we can see that if we desire to obtain the conductivity structure from our data (the measured voltages and input currents), we have to solve a non-linear optimization problem. Furthermore, as the number of data is much smaller than the number of model parameters we wish to obtain, the system is underdetermined and thus our optimization problem has a two-part objective function:

$$\Phi(\mathbf{m}) = \frac{1}{2} \|\mathbf{d}(\mathbf{m}) - \mathbf{d}_{\text{obs}}\|^2 + \frac{\beta}{2} \|\mathbf{W}(\mathbf{m} - \mathbf{m}_{\text{ref}})\|^2 \quad (3.6)$$

where  $\mathbf{d}_{\text{obs}}$  is a vector containing the observed data (observed voltages divided by the input current);  $\mathbf{d}(\mathbf{m})$  is a vector containing calculated data for a given conductivity model obtained by solving equation 3.3; The second term in equation 3.6 is a Tikanov style term that contains our a-priori knowledge about the solution;  $\beta$  is the regularization parameter that balances the effect of data misfit and model regularization during the minimization;  $\mathbf{m}$  is our model at a given iteration, where the model parameters are  $\ln(\sigma)$  (taking the log enforces a positivity constraint on the solution); and  $\mathbf{m}_{\text{ref}}$  is the best guess starting model.

The first term in the objective function serves to ensure that our recovered model matches the observed data. The second term enforces our a-priori knowledge as to the shape and structure of the final model. For Tikanov style regularization, this term usually forces the model to be either: small, meaning it deviates little from the reference model; flat, meaning that the first derivative of the  $\mathbf{m} - \mathbf{m}_{\text{ref}}$  is minimized; smooth, meaning that the second derivative of the  $\mathbf{m} - \mathbf{m}_{\text{ref}}$  is minimized; or some combination of the three.

Given the above objective function, we use the Gauss-Newton approach to invert for the best model, given our regularization choices, that fits the observed data. We

define a starting model,  $\mathbf{m}_i$ , that is near the local minimum of the objective function,  $\mathbf{m}_{\min}$ , of equation 3.6, and linearize equation 3.6 about this solution:

$$\Phi(\mathbf{m}) = \frac{1}{2} \left\| \left( \mathbf{d} + \frac{\partial \mathbf{d}}{\partial \mathbf{m}} \cdot \delta \mathbf{m} \right) - \mathbf{d}_{\text{obs}} \right\|^2 + \frac{\beta}{2} \|\mathbf{W}(\mathbf{m}_i - \mathbf{m}_{\text{ref}})\|^2 \quad (3.7)$$

To obtain the minimum of equation 3.7, we take the derivative with respect to the model, set it to zero, and obtain the Gauss-Newton update:

$$\underbrace{(\mathbf{J}^T \mathbf{J} + \beta \mathbf{W}^T \mathbf{W})}_{\mathbf{H}} \cdot \delta \mathbf{m} = - \underbrace{(\mathbf{J}^T (\mathbf{Q} \mathbf{A}^{-1} \mathbf{q} - \mathbf{d}_{\text{obs}}) + \beta \mathbf{W}^T \mathbf{W} (\mathbf{m} - \mathbf{m}_{\text{ref}}))}_{\mathbf{g}} \quad (3.8)$$

where  $\mathbf{J}$  is the Jacobian, or sensitivity matrix,  $\left( \frac{\partial \mathbf{d}}{\partial \mathbf{m}} \right)$ ;  $\mathbf{g}$  is the gradient of the objective function; and  $\mathbf{H}$  is the approximation to the Hessian. We note that  $\mathbf{J}$  is a very large, dense matrix so, from a computational point of view we want to avoid explicitly forming the matrix. However, it was shown in Haber et al. (2000b) that  $\mathbf{J}$  has the form:

$$\mathbf{J} = -\mathbf{Q} \mathbf{A}^{-1} \mathbf{B} \quad (3.9)$$

where  $\mathbf{B} = \frac{\partial(\mathbf{A}(\mathbf{m})\mathbf{u})}{\partial \mathbf{m}}$ . The matrices  $\mathbf{B}$  and  $\mathbf{Q}$  are sparse matrices, thus the product of the sensitivity matrix and a vector (or its adjoint) can be found by solving the forward or adjoint problems. Because of this, we do not compute the Hessian explicitly but instead perform as series of matrix-vector products. The algorithm for computing the Hessian approximation is as follows (**J** Algorithm):

1. Given a vector  $\mathbf{v}$ , we calculate the vector matrix product,  $\mathbf{w} = \mathbf{B} \cdot \mathbf{v}$ ;
2. We then solve the linear system  $\mathbf{y} = \mathbf{A}^{-1} \mathbf{w}$ ;
3. Finally we solve for  $\mathbf{J} \cdot \mathbf{v}$  by taking the matrix-vector product of  $\mathbf{Q} \cdot \mathbf{y}$ .

We can therefore calculate our model update as described by equation 3.8 through a series of computationally efficient matrix-vector products.

### 3.2.2.2 *Incomplete Gauss-Newton*

In order to solve equation 3.8 we have two practical challenges. First, although  $\mathbf{J}$  can be calculated through a series of matrix-vector products, this requires solving the

linear system,  $\mathbf{y} = \mathbf{A}^{-1}\mathbf{w}$  many times. If we are required to do this to a high tolerance, this can become computationally prohibitive. Second, solving equation 3.8 involves computing the solution:

$$\delta\mathbf{m} = -\mathbf{H}^{-1} \cdot \mathbf{g} \quad (3.10)$$

Regardless how one solves this equation, whether by Gauss elimination or an iterative technique such as conjugate gradients,  $\mathbf{H}$  is a very large, dense matrix and thus solving for  $\delta\mathbf{m}$  to a high tolerance can be expensive. Fortunately, Dembo, Eisenstat and Stiehaug (1982) noted that neither  $\mathbf{J}$  nor  $\mathbf{H}^{-1}$  need to be solved to a high tolerance to obtain a useful model update; this observation led to the Inexact Gauss-Newton (IGN) algorithm. When using this approach we use the same Gauss-Newton formulation as in equation 3.8, but we solve equation 3.8 (and its' components) to a very low tolerance. With this algorithm, we solve for  $\delta\mathbf{m}$  as follows ( $\delta\mathbf{m}$  Algorithm):

1. Calculate  $\mathbf{g}$  to a high tolerance, so that the descent direction is correct.
2. Enter into a preconditioned conjugate gradient (PCG) solver to solve equation 3.10
3. Form  $\mathbf{H}$  within the PCG solver, at each iteration in the solver, to a low tolerance using the  $\mathbf{J}$  Algorithm.
4. Iterate within the PCG solver for a small number of iterations (e.g. less than five) to obtain an approximate model update.

Obtaining the update by this method is substantially cheaper than performing a traditional Gauss-Newton inversion.

### 3.2.2.3 *Line-search and further iterations*

Once we have acquired a model update vector, as described in the  $\delta\mathbf{m}$  Algorithm, we generate a new model:

$$\mathbf{m}_{i+1} = \mathbf{m}_i + \alpha\delta\mathbf{m} \quad (3.11)$$

where  $\mathbf{m}_{i+1}$  is the new model, and  $\alpha$  is a line search parameter. The line search parameter is used to control the magnitude of the model update. We determine an acceptable value

for  $\alpha$  by defining a sufficient decrease condition, the Armijo rule, for our objective function:

$$\Phi(\mathbf{m}_{i+1}) = \Phi(\mathbf{m}_i + \alpha \delta \mathbf{m}) \leq \Phi(\mathbf{m}_i) + c_1 \alpha \nabla \Phi(\mathbf{m}_i)^T \delta \mathbf{m} \quad (3.12)$$

where  $c_1$  is a constant that in practice takes a very small value, for example  $10^{-4}$ . When performing the model update in equation 3.11, the initial value of  $\alpha$  is set to one and the new model is generated. The inequality in equation 3.12 is evaluated, and if the condition is satisfied, the new model is accepted; however, if the condition is not satisfied,  $\alpha$  is reduced by one-half, and the equations are re-evaluated. This procedure is repeated until we find a new model that meets the criterion of equation 3.12.

As equation 3.8 resulted from a linearization about the model,  $\mathbf{m}_i$ , the resulting model,  $\mathbf{m}_{i+1}$ , so is not likely the local minimum we seek. We therefore perform another iteration of the IGN update, this time linearizing about the model  $\mathbf{m}_{i+1}$ . This iterative process is repeated until the objective function and/or the data misfit have decreased to a specified level.

In practice, if the initial model guess is near the solution, the number of overall iterations, i.e. the number of model updates obtained using IGN, will rarely exceed ten. When the initial model guess is far from the solution, it may take more IGN iterations; however, for an extremely poor initial guess, the algorithm may not converge.

#### 3.2.2.4 *The complete algorithm*

In order to summarize the key details of the inversion algorithm, we present the following pseudo code, **Inversion**, that outlines the implementation of the algorithms described above. This pseudo code bears much resemblance to the functioning source code we have included, **InvMainN.m**. Users should note that many of the function names are different within that code, as the pseudo code provided here has been written with a view to detailing the general structure of the code.

```
function [d,msol] = Inversion(dobs,mi)
% Input:      dobs = observed data, mi = initial model
% Output:     d = predicted data, msol = solution

A = Form_Forward_operator(mi); % Obtain forward operator for mi
qcorr = BC_correction(A,mi); % Apply Boundary Correction to the source term
```

```

% Start Incomplete Gauss-Newton loop
while  $\Phi >$  tolerance
    % Solve forward problem for the potential field
     $\mathbf{U} = \text{Asolve}(\mathbf{A}, \mathbf{q}_{\text{corr}})$ ;
    % Calculate the predicted data from  $\mathbf{U}$ 
     $\mathbf{d} = \text{Qu}(\mathbf{U})$ ;
    % Calculate the value of the objective function
     $\Phi(\mathbf{m}_i) = 0.5 * \text{norm}(\mathbf{d} - \mathbf{d}_{\text{obs}}) + 0.5 * \beta * \text{norm}(\mathbf{W}(\mathbf{m}_i - \mathbf{m}_{\text{ref}}))$ ;
    % Evaluate the gradient of the objective function
     $\mathbf{g} = \text{Objective\_function\_gradient}(\mathbf{A}, \mathbf{q}_{\text{corr}}, \mathbf{d}, \mathbf{m}_i)$ 
    % Solve for incomplete Gauss-Newton update using PCG
     $\delta \mathbf{m} = \text{PCG}(\mathbf{A}, \mathbf{q}_{\text{corr}}, -\mathbf{g}, \mathbf{d}, \mathbf{m}_i)$ ;
    % Start line search to find correct step length
     $\alpha = 1$ ;
    for j = [1:5];
        % Update model
         $\mathbf{m}_{i+1} = \mathbf{m}_i + \alpha * \delta \mathbf{m}$ ;
        % Update the forward operator
         $\mathbf{A} = \text{Form\_Forward\_operator}(\mathbf{m}_{i+1})$ ;
        % Solve forward problem for the potential field
         $\mathbf{U} = \text{Asolve}(\mathbf{A}, \mathbf{q}_{\text{corr}})$ ;
        % Calculate the (predicted) data from  $\mathbf{U}$ 
         $\mathbf{d} = \text{Qu}(\mathbf{Q}, \mathbf{U})$ ;
        % Calculate the value of the objective function for  $\mathbf{m}_{i+1}$ 
         $\Phi(\mathbf{m}_{i+1}) = 0.5 * \text{norm}(\mathbf{d} - \mathbf{d}_{\text{obs}}) + 0.5 * \beta * \text{norm}(\mathbf{W}(\mathbf{m}_{i+1} - \mathbf{m}_{\text{ref}}))$ ;
        % Define the Armijo goal
         $\Phi_{\text{goal}} = \Phi(\mathbf{m}_i) - c_1 * \alpha * (\mathbf{g}' * \delta \mathbf{m})$ ;
        % Check to see if  $\Phi(\mathbf{m}_{i+1})$  meets criteria, if not, reduce  $\alpha$ 
        if  $\Phi(\mathbf{m}_{i+1}) < \Phi_{\text{goal}}$ ; break;
        else ;  $\alpha = \alpha / 2$ ; end;
    end
end
end

```

## 3.3 MATLAB Implementation

---

In this section we describe the pertinent details regarding our implementation of the above Incomplete Gauss-Newton algorithm. All of the source code has been developed in MATLAB. This was done for two main reasons. MATLAB source code is platform independent, and thus any user can download the source code and run the driver files, without any need to recompile. MATLAB has excellent built in graphical support, allowing the user to easily produce a variety of different 3-D renderings of the resulting models. Also throughout the development stage of the is code many colleagues have suggested that MATLAB is good only for small problems; however, this implementation has been used on desktop PC's to invert for model spaces that exceed 300,000 parameters – more than enough to accommodate most realworld resistivity surveys. Furthermore, by paying special attention to vectorizing the MATLAB code, we are able to obtain computational speeds that are on par with Fortran implementations of similar algorithms.

### 3.3.1 Data structure

Our entire inversion code has 35 m-files associated with it; additionally, many of these functions call built in MATLAB functions. With this number of functions an efficient method for passing variables in and out functions is necessary. Throughout this code we take advantage of MATLAB's structure arrays. MATLAB structures arrays have fields that can be named and assigned values that can range from scalars to multidimensional matrices. The advantage of using these data structures is that it allows one to pass a large quantity of information between functions, with only a few variable names having to be passed. For this work we require two user defined structures for the inversion to operate, the default names for these structures are 'MTX' and 'para'. These two structures contain all the information needed to run the inversion. Figures 3.1 and 3.2 outline the key components of the 'para' and 'MTX' structures respectively. Further details, such as specific parameter values, can be found in the driver files for the inversion code.

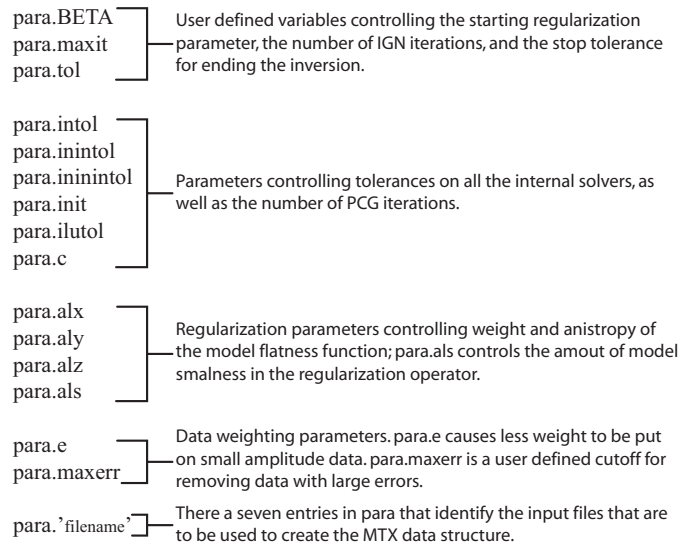


**Figure 3.1 A breakdown of the components that make up the ‘para’ structure. All entries in ‘para’ are user defined, and must be entered before the ‘MTX’ structure can be created.**

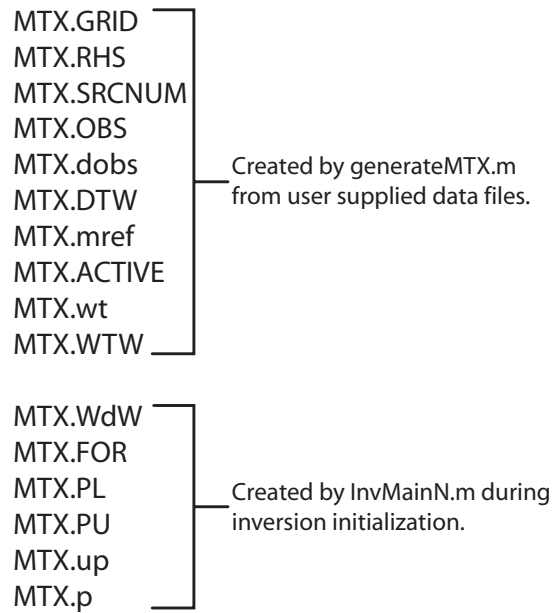


**Figure 3.2 A breakdown of the components in the 'MTX' structure. The total structure is built in two stages, the first is created using the function generateMTX.m; the second part is created in the beginning of InvMainN.m.**

Of particular note in the ‘para’ structure is the ability for the user to easily adjust the amount of regularization and type of regularization (smallness or flatness) that is applied to a specific problem; one can also adjust the magnitude of the flatness operator in the x, y and z directions. This allows the user to directly observe the effect of different regularization weights on the final solution.

‘MTX’ is the structure that contains all the information regarding the model and data spaces. A description of each component of ‘MTX’ can be found in the documented m-files, *updateMTX.m* and *generateMTX.m*; however, below we will refer to some of the more important components of ‘MTX’ in the context of specific features of our inversion code.

### 3.3.2 *Solving the Forward Problem*

For each iteration of our IGN algorithm, we need to create a single forward operator matrix, as described by equation 2. We have chosen to create and store the operator matrix as well as the preconditioning matrices, rather than recreate them each time they are required. This only marginally increases memory requirements, as the matrices are all sparse. But greatly increasing computational performance, as we only have to update the operator and preconditioner once per IGN iteration.

In order to construct the forward operator matrix, we first generate the divergence and gradient operator matrices with function calls to *div.m* and *grad.m*, respectively. Then we create our **S** matrix with the function *massf.m*. The three resulting sparse matrices are multiplied together to yield the forward modeling matrix, which is stored in the ‘MTX’ structure as MTX.FOR. It should be noted, that prior to storing the forward operator matrix, we perform a symmetric reverse Cuthill-McKee permutation (*symcrm.m*) to reshape the problem so that it is faster to calculate the preconditioner for the iterative solver. That is, we store a permutation of the forward operator.

The forward operator is sparse and banded, therefore, equation 3 can be rapidly solved using preconditioned iterative methods. However, because we must solve the linear system in equation 3 for each source term, it is computationally expedient to calculate a good preconditioner, as this needs to be done only once per IGN iteration. For this work, we use an incomplete LU factorization, using the built-in MATLAB function

*luinc* to generate the preconditioning matrices. Using a low drop tolerance, of between  $10^{-3}$  and  $10^{-4}$ , we realize a dramatic speed up of the iterative solver. With this preconditioner, we solve the system in equation 3 for all the source terms, using a preconditioned bi-conjugate stabilized gradient algorithm (*bicgstb.m*) (Saad, 1996).

### 3.3.3 *Making a right hand side and picking data*

In order to solve equation 3, we first need to create a right hand side source vector (or matrix for the case of multiple sources). In practice, we have field constraints such as topography and borehole deviations that do not allow us to locate sources at cell centers. Furthermore, upon solving equation 3 we have the potential field at each cell centre in our model space. Our observed data however, are likely a subset of these measurements, and as above, the receivers might not be located at cell centers. Therefore, for both the source term,  $\mathbf{q}$ , and the projection matrix,  $\mathbf{Q}$ , we must interpolate to cell centers. The matrices  $\mathbf{q}$  and  $\mathbf{Q}$  are stored in the ‘MTX’ structure as MTX.RHS and MTX.OBS, respectively.

We describe here the formation of the  $\mathbf{Q}$  matrix. The process for generating  $\mathbf{q}$  is the same, except that in  $\mathbf{q}$ , interpolation weights are scaled by a factor of  $\frac{1}{\Delta V}$ , where  $\Delta V$  is the cell volume. If a receiver is not located on a cell center, we linearly interpolate to the eight surrounding cells. This results in a row entry in  $\mathbf{Q}$  that has eight weighting values; these values are the weighted contribution of the surrounding eight cells to the off-center datum. For data located at the surface where the z-coordinate equals zero, the data are assigned a z-coordinate that corresponds to the center of the first cell in the z direction. The surface data are then interpolated to the four surrounding cells in the x and y directions. In this case the corresponding row of  $\mathbf{Q}$  has four data weights. If the datum lies on a cell center, the resulting row entry in  $\mathbf{Q}$  is simply one at the datum location.

We note that our approach to dealing with data picking and creating the source term does not take advantage of certain acquisition structures. When using traditional surface arrays, it is possible to reorder the source and receivers in such a way as to create a smaller number of RHS’s; this can result in a faster inversion. However, given that this code is intended as a research tool, we felt that the user should be free to use any

acquisition geometry, and thus opted to pay the computational penalty. We hope this freedom will encourage users to deviate from traditional survey geometries and explore novel modes of acquisition, such as combined surface and borehole, which can lead to substantially accurate inversion results.

### 3.3.4 *Data weighting*

In order to ensure that we match the most trustworthy data, i.e. data with low error, we need to apply a data weighting term to the first term in the objective function, equation 6. The residual in the data term of the objective is scaled by a matrix (MTX.WdW) such that the objective function becomes:

$$\Phi(\mathbf{m}) = \frac{1}{2} \|\mathbf{WdW}(\mathbf{d}(\mathbf{m}) - \mathbf{d}_{\text{obs}})\|^2 + \frac{\beta}{2} \|\mathbf{W}(\mathbf{m} - \mathbf{m}_{\text{ref}})\|^2 \quad (3.13)$$

In our implementation  $\mathbf{WdW}$  has a simple, standard form. The main diagonal of  $\mathbf{WdW}$  contains entries of the absolute error:

$$\text{diag}(\mathbf{WdW}) = \frac{\mathbf{1}}{|\mathbf{d}_{\text{obs}}| \cdot \text{SD}(\mathbf{d}_{\text{obs}}) + \varepsilon} \quad (3.14)$$

where,  $\text{SD}(\mathbf{d}_{\text{obs}})$  is the standard deviation of the observed data (MTX.DTW) and  $\varepsilon$  is a weighting term (para.e) that keeps the inversion from placing too much weight on very low amplitude data. We note that  $\varepsilon$  should be chosen to be larger than the smallest data value, otherwise the data residual vector in equation 3.13 will become close to a vector of ones, and the inversion will not be able to accurately determine a step direction.

### 3.3.5 *Regularization and Model weighting*

Regularization is a critical part of the inversion process. Because we are solving a highly underdetermined system, regularization has a high level of control over the resulting solution. We have chosen to use Tikhonov style regularization in this implementation; however, users will find it easy to modify the code and implement a different regularization scheme.

The function *calcWTW.m* creates the model regularization matrix,  $\mathbf{W}$ , in equation 3.13. The output is stored as MTX.WTW. This is set not to change for the entire inversion, although this can be easily changed if one desires. We use a combination of

model smallness, a diagonal matrix of ones, and anisotropic model flatness, a weighted gradient operator, to create `MTX.WTW`. The variable `para.als` controls the smallness weighting. `para.alx`, `para.aly` and `para.alz` are the relative weights applied to the x,y and z components of the gradient, respectively. The addition of a smoothness constraint can be easily achieved by adding a second gradient term. We have found little difference between ‘flat’ and ‘smooth’ solutions, so have opted not to include this.

In addition to including the smallness and flatness term, `MTX.WTW`, also contains a user defined vector of model weights, `MTX.wt`. The purpose of this vector is to allow the use to inject further a-prior knowledge into the regularization operator. In the absence of additional knowledge, the vector is set to ones. In many situations the vector will be more complicated than this. For example, if one wishes to penalize model changes near source locations, such as in the borehole example provided here, one can construct a vector that has weights that fall off away from the source location. In the case of the surface data presented here, we have included a depth weighting term, that has model weights that fall off as  $\frac{1}{z^2}$ . In addition, this term is useful for ‘softly’ forcing the inversion to match other data, such as borehole logs. If the log data are included in the reference model, a large model weight can be applied at the borehole locations forcing the inversion results to remain close to the logs at these locations, while not completely constraining results to match the log values.

#### ***3.3.5.1 A note on $\beta$***

Much work has been done on the benefits of reducing  $\beta$  during the inversion process. Many approaches have been suggested in the literature and are used in practice. The three most common approaches to dealing with  $\beta$  are: 1) fixing  $\beta$  for the entire inversion, 2) reducing  $\beta$  by a fixed amount after each iteration and 3) using a L-curve criteria to choose the appropriate  $\beta$  at each iteration. The last of these approaches arguably will provide the best results; however, there is a substantial computational cost associated with determining the correct  $\beta$ . For this implementation we have chosen to fix  $\beta$  for the entire inversion. We have found that this often yields suitable results and is the least computationally intensive approach. Furthermore, we have written the code in such a way that is easy for a user to implement a different strategy for finding  $\beta$ .

### 3.3.6 *Active vs InActive cells*

In addition to regularization and model weighting, we have also included another way to impose a-priori knowledge on the solution. This is in the form of user defined active and inactive cells. The vector, `MTX.ACTIVE`, contains 1's for active cells and 0's for inactive cells. Inactive cells are included in the forward problem, i.e. calculating the data, but are excluded from the inversion step, and thus the value of the model at these locations remains fixed at the reference model value. This is an excellent way to incorporate data, such as borehole data, as hard constraints. In addition, it is also often desirable to make cells in boundary regions inactive, so the inversion concentrates on the region of interest.

This functionality also provides the user with the ability to incorporate topography into the inversion. By setting cells near the surface to inactive, and assigning a very small conductivity to the reference model at these locations, say  $10^{-5}$  S/m, one can simulate the effect of topography.

### 3.3.7 *Incomplete Gauss Newton*

As stated above, the IGN algorithm involves solving for the Gauss-Newton update to a low tolerance. In general the implemented algorithm closely parallels the pseudo code presented above. The complete routine is *InvMainN.m*; the only required inputs for the code are 'para' and 'MTX'. One note about our implementation of the IGN algorithm: all the expensive calculations are a series of matrix vector products; if needed we can solve these matrix vector products without having to explicitly form the matrix. This can be quite advantageous for particularly large problems, as it greatly reduces the memory requirements. In particular, we take advantage of this when calculating the matrix vector product  $\mathbf{w} = \mathbf{B} \cdot \mathbf{v}$ . We never actually form  $\mathbf{B}$ , which is denser than the  $\mathbf{A}$  matrix

The first step is to calculate the objective function gradient  $\mathbf{g}$  to a high tolerance. This step involves solving equation 3.3 for each source term, as well as solving the adjoint of equation 3.3. The tolerance to which we solve equation 3.3 governs the tolerance of the resulting gradient, thus we solve to a tolerance of  $10^{-8}$  or higher. This tolerance level is set in `para.inintol`.

Once we have calculated the gradient we call the function *IPCG.m*, which is the pre-conditioned conjugate gradient solver. This function solves for the model update in equation 3.8. We precondition at each iteration by first solving the following equation:

$$\beta \mathbf{W}^T \mathbf{W} \cdot \mathbf{z} = -\mathbf{g} \quad (3.15)$$

where  $\mathbf{z}$  is the approximate solution to equation 3.8. Solving 15 is inexpensive because  $\mathbf{W}^T \mathbf{W}$  is very sparse; moreover, if  $\beta$  is large the regularization term dominates the objective function, and  $\mathbf{z}$  is likely close to the solution of equation 3.8. Within the PCG solver, at each iteration, we are required to compute the forward and adjoint solutions to equation 3.3, as we did for the gradient. In order to obtain a computationally efficient solution we: 1) minimize the number of conjugate gradient iterations (controlled by `para.init`) and 2) solve the forward and adjoint problems to a very low tolerance, say  $10^{-4}$ , which is set in `para.inintol`. This results in a solution for the model update from equation 3.8 that may have a solution tolerance of  $10^{-2}$ ; although low, this is sufficient to achieve a good descent direction.

## 3.4 Examples

---

### 3.4.1 *A surface based field experiment*

#### 3.4.1.1 *The model*

The MATLAB script *DCdriverS.m* runs an inversion of a synthetic surface-based field experiment. In this experiment the goal is to image the injection of a saline tracer into the subsurface. Injection of tracers is often performed by hydrologists in an effort to obtain information about subsurface hydrologic properties. In this experiment, we simulate the tracer-saturated soil as a 10 Ohm-m material immediately adjacent to the borehole. Slightly away from the borehole we simulate the diffuse edge of the injected tracer by setting the resistivity to 40 Ohm-m. Figure 3.3 is a schematic outlining the field scenario.

The maximum extent of the tracer is seen as the blue 40 Ohm-m isosurface. On the surface we deploy 96 electrodes. 38 of these electrodes function as potential electrodes only, while the remaining 58 serve as both potential and current electrodes. The experiment involves 41 independent current pairs. For each of these pairs, data are recorded at the remaining 94 electrodes. Data are recorded using dipoles, so for each current pair, we record 93 independent data. This results in a total of 3813 data for the entire survey. The entire model space for this experiment is 19040 cells, with the tracer occupying only 198 of these cells. The synthetic data were created using the forward modeling algorithm described above; however, as these were being used for synthetic modeling, no boundary condition correction was applied. The resulting synthetic data were corrupted with 3% uniformly distributed random noise.

#### 3.4.1.2 *Inverse results*

For this inversion, the reference model was set to a homogeneous 200 Ohm-m background. Regularization was a combination of smallness and isotropic flatness; the relative weights of these components were  $1^{-2}$  and 1, respectively.  $\beta$  was fixed at a value

of five. The model weighting vector contains weights that fall off with depth as  $\frac{1}{z^2}$ . This is done to account for the nonuniqueness associated with the lack of data in the  $z$ -direction. We ran five iterations of IGN, at which point the objective function had been reduced to approximately 20% of its original value. Figure 3.4 shows the results of the inversions.

Frames **a** and **b** are slices through the 3-D volume of the synthetic model. **a** is a cross-section slice while **b** is a depth slice, taken at a depth of four meters. **a'** and **b'** are inversion slices, taken at the same locations as **a** and **b**. The inversion captures the location of the tracer in both the cross-section and depth slice. The magnitudes recovered from the inversion overestimate the resistivity, and the variance of the solution is higher; both of these are a function of the underdetermined nature of the problem.

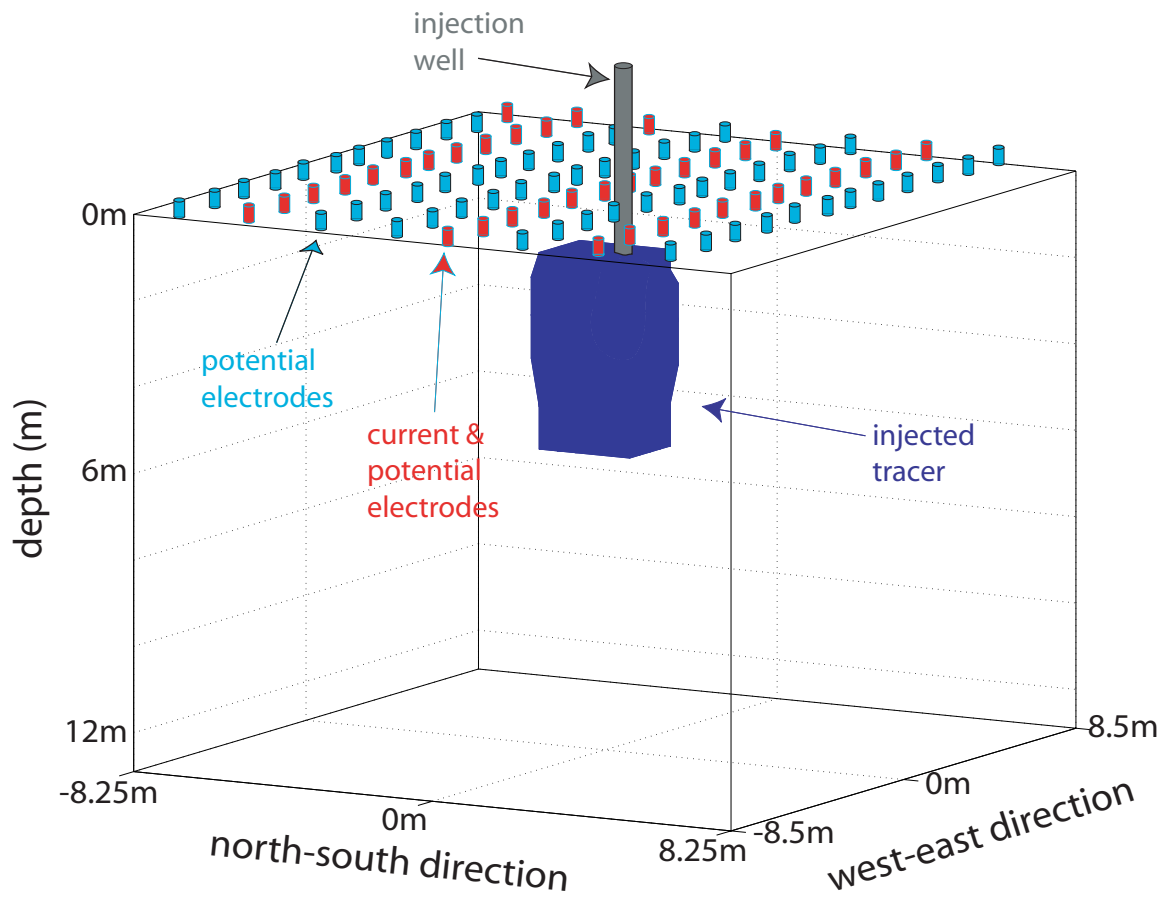
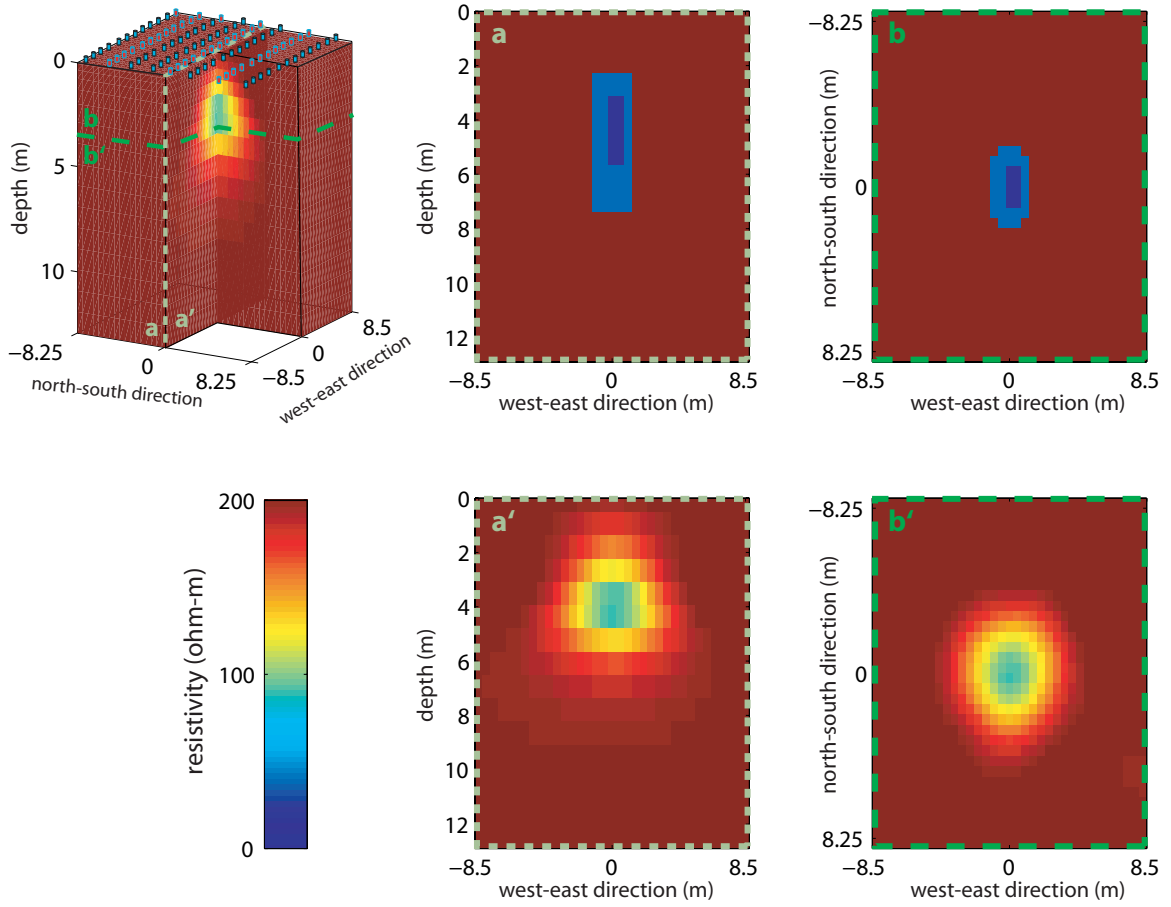


Figure 3.3 A schematic of the surface field experiment. Blue electrodes function as potential electrodes only, while the red electrodes serve as both potential and current electrodes.



**Figure 3.4 Inversion results for surface based acquisition.**

### 3.4.2 *A example of cone- based electrical resistivity tomography*

#### 3.4.2.1 *The model*

For the second synthetic example we explore a slightly more complex survey geometry that includes sub surface electrodes. The acquisition technique used here is cone-based electrical resistivity tomography; this technique has been documented in Pidlisecky et al. 2005. The acquisition technique involves first emplacing a small number of permanent current electrodes, then using an electrode mounted on a cone penetrometer to make potential measurements at various locations in the subsurface. In this synthetic example, a factory is suspected of leaking contaminants into the ground beneath its footprint. The presence of the factory makes it impossible to perform a surface-based geophysical survey over the region of interest. As we wish to image the volume beneath the factory, we need to surround the volume with electrodes. For this example, we have eight source electrodes, and 168 potential electrodes, the respective locations can be seen in Figure 3.5.

The conductivity model that was used for this experiment has a homogeneous 100 Ohm-m background resistivity, corresponding to a freshwater sandy aquifer. The contaminated soil is modeled as a 5 Ohm-m material. The model space has 13200 cells, with the contaminant occupying 116 of these cells. The position of the contaminant can be seen in Figure 3.5. The eight source electrodes yield 28 independent current pairs. We have 168 potential electrode positions. With this acquisition technique we have a potential electrode located at infinity, thus we acquire pole-dipole data. The entire experiment yields 4704 synthetic data points. As with the previous example, the data were generated using the forward modeling algorithm described above; these data were corrupted with 3% uniformly distributed random noise.

#### 3.4.2.2 *Inverse results*

The example run we have included here, which can be found in *DCdriverBH.m*, was run using a fixed regularization value,  $\beta$ , of  $1^{-1}$ . The reference model is a

homogeneous 100 Ohm-m half space.  $\mathbf{W}$  was a combination of model smallness and isotropic flatness, with a weighting of  $10^0$  and  $10^{-2}$  on the respective criteria. The model weighting vector contains weights at the current source locations to penalize structure at these points. As with the previous example, we ran five iterations of IGN, at which point the objective function had been reduced to approximately 7% of its original value. Figure 3.6 shows the results of the inversions. For this example, we have 3-D data, and thus see excellent inversion results. The location of the plume, and the magnitude of resistivity values are reasonably well matched. We still slightly overestimate the resistivity values, and we have some smearing, but obtain a high quality image.

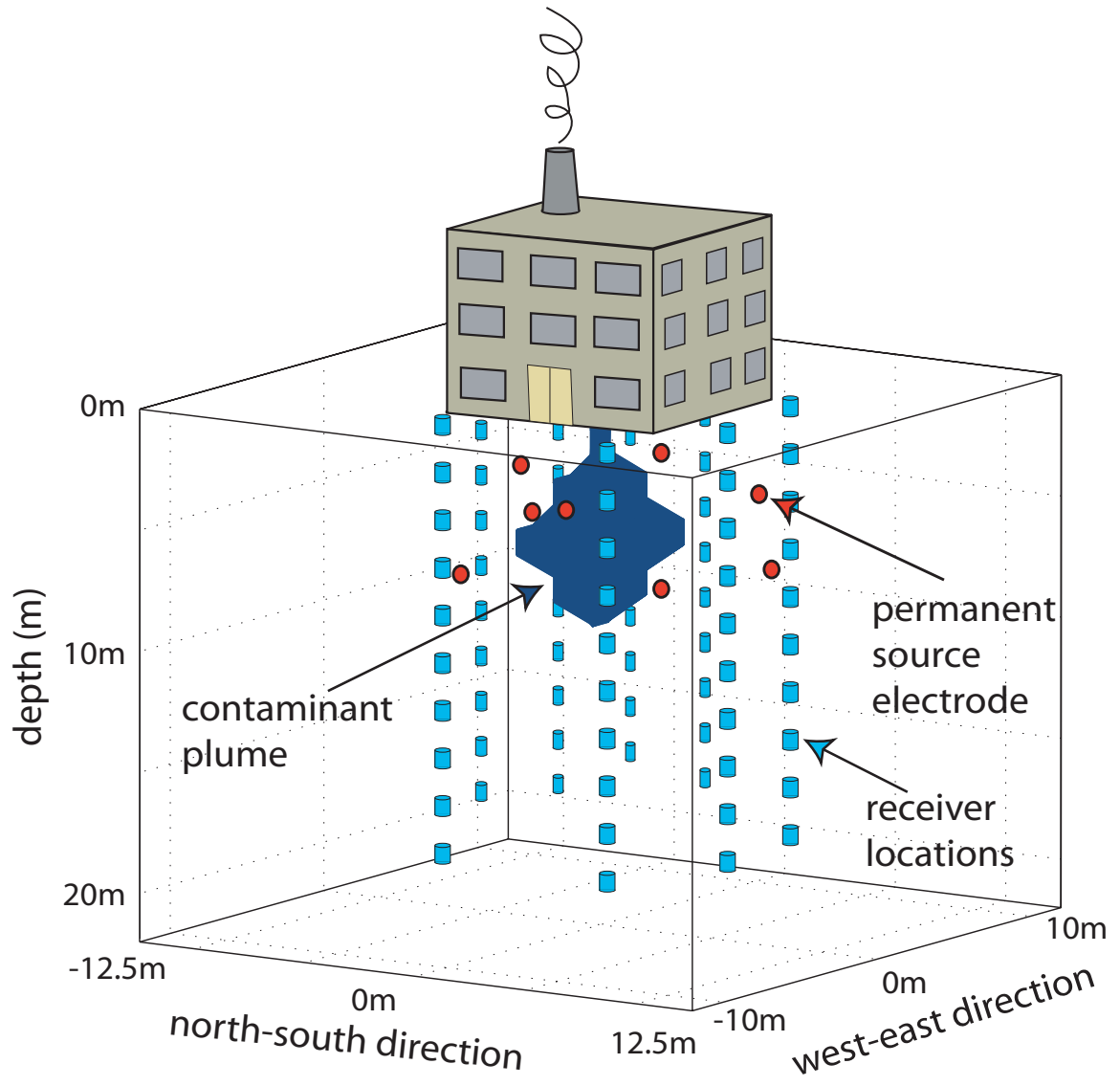
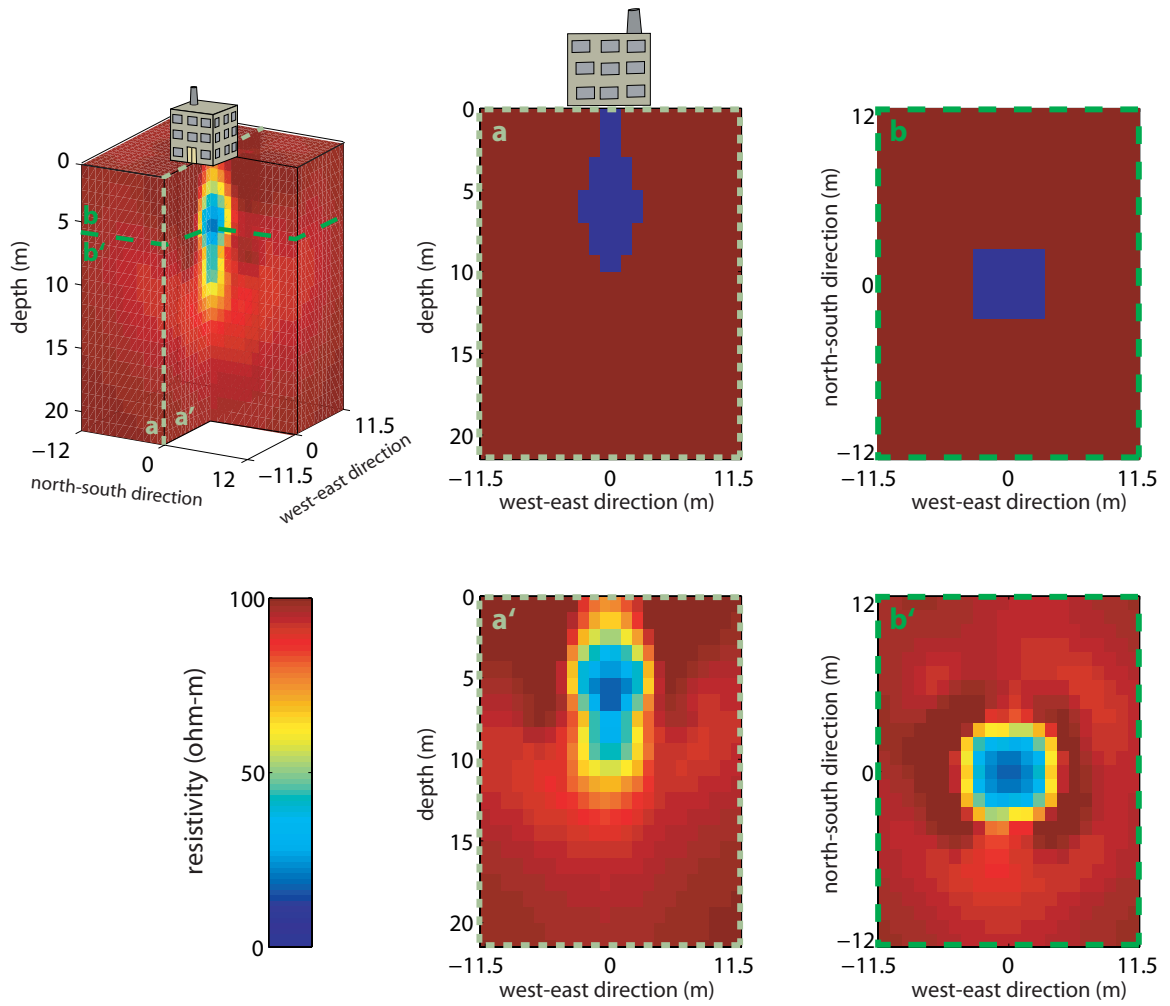


Figure 3.5 Schematic of the Cone-based acquisition. Blue locations are where potential measurements are made. Current electrodes are seen in red.



**Figure 3.6 Inverse results for the Cone-based acquisition.**

## 3.5 Summary

---

We have developed a 3-D inversion package for electrical resistivity data. The code is easy to read, flexible and can easily be modified by the user. It has been developed in the MATLAB environment, and thus is platform independent. Furthermore, working in MATLAB allows the user to take advantage of the built-in visualization functions that are excellent for working with the inverse models. We used a very efficient inversion algorithm, the Incomplete Gauss-Newton. In addition, we paid special attention to implementing the code in a computationally efficient manner, and thus have achieved computational speeds that are comparable to implementations in Fortran. We hope this code will be adopted by researchers, and further developed so as to create an open source repository of codes for working with, and improving in the state of the science of, resistivity imaging.

# CHAPTER 4

## CONE-BASED ELECTRICAL RESISTIVITY TOMOGRAPHY

### Abstract

---

Determining the 3-D spatial distribution of subsurface properties is a challenging, but critical, part of managing the clean-up of contaminated sites. We have developed a minimally invasive technology that can provide information about the 3-D distribution of electrical conductivity. The technique, cone-based electrical resistivity tomography (C-bert), integrates resistivity tomography with cone-penetration testing. Permanent current electrodes are emplaced in the subsurface and used to inject current into the subsurface region of interest. The resultant potential fields are measured using a surface reference electrode, and an electrode mounted on a cone penetrometer. The standard suite of cone penetration measurements, including high resolution resistivity logs, are also obtained and are an integral part of the C-bert method.

C-bert data are inverted using an inexact Gauss-Newton algorithm to produce a 3-D electrical conductivity map. A major challenge with the inversion is the large local perturbation around the measurement location, due to the highly conductive cone. As the cone is small with respect to the total model space, explicitly modeling the cone is cost prohibitive. We have developed a rapid method for solving the forward model which uses iteratively determined boundary conditions (IDBC). This allows us to generate a computationally feasible, pre-inversion, correction for the cone perturbation.

We assessed C-bert by performing a field test to image the conductivity structure of the Kidd2 site near Vancouver, British Columbia. A total of nine permanent current electrodes were emplaced and five C-bert data sets were obtained, resulting in 6516 data points. These data were inverted to obtain a 3-D conductivity image of the subsurface.

Furthermore, we demonstrated, using a synthetic experiment, that C-bert can yield high quality electrical conductivity images in challenging field situations. We conclude that C-bert is a promising new imaging technique.

## 4.1 Introduction

---

One of the main challenges in the clean-up and management of a contaminated site is developing an accurate model of the subsurface. Such a model ideally contains information about the location of contaminants, and information about the subsurface properties controlling the long-term fate and transport of the contaminants. Borehole-based electrical resistivity tomography (ERT) is a geophysical method that is being increasingly used to assist in the development of subsurface models. ERT involves injecting current through a pair of electrodes in one borehole, and measuring the resulting potentials at numerous (tens to hundreds of) electrodes located in the same borehole, and in different boreholes. The measurements yield values of resistance that can be inverted to determine the subsurface electrical conductivity structure. The electrical conductivity structure has been used, for example, to infer the presence of a contaminant, with electrical conductivity different from that of the background environment, (e.g LaBrecque and Yang, 2001; Daily and Ramirez, 1995) and to obtain information about potential flow paths of contaminants by imaging the movement of conductive tracers (Versteeg et al., 2000; Slater et al., 2000; Kemna et al., 2002; Slater, 2002; Singha and Gorelick, 2005).

A critical problem with the use of borehole-based ERT is the requirement of boreholes. Boreholes are not desirable at many contaminated sites due to the fact that installation is expensive, time consuming, and risks the exposure of workers to contaminants. In addition there is potential for mobilizing contaminants by creating, with the boreholes, new pathways in the subsurface. These issues have motivated us to develop an ERT system that does not require the use of boreholes, but uses a cone penetrometer to position a small number of subsurface current electrodes around the region of interest and to make potential field measurements between an electrode mounted on the cone and a surface reference electrode.

The cone penetrometer is a testing tool that was developed by geotechnical engineers for obtaining high-resolution depth logs of mechanical soil properties. A cone penetrometer, commonly referred to as a cone, is a 36mm diameter steel rod, ~1m long,

with sensors mounted close to a cone-shaped tip. Cone penetration testing (CPT), i.e. using the cone for subsurface characterization, is a technique that is now widely used in the environmental and geotechnical engineering community (Campanella and Weemeees, 1990; Daniel et. al., 1999). The technique is classified as minimally invasive because instead of drilling a borehole to make subsurface measurements, a cone is pushed into unconsolidated materials using hydraulic rams mounted on a large truck, referred to as the cone truck. While the cone is being pushed, measurements are made with the sensors in a near continuous fashion, with typical sampling every 2.5cm. To reach the measurement depth of interest, 1m sections of steel rod are added to the end of the cone. The maximum depth of investigation varies with geologic environment, but is generally limited to ~100m. CPT is an efficient, relatively inexpensive alternative to borehole installation and works extremely well in areas of alluvial and deltaic deposits consisting of clays, silts or sands.

The standard cone penetrometer, as most commonly configured, is shown schematically in Figure 4.1a. This standard cone measures three separate ground properties: tip penetration resistance, friction sleeve resistance and induced pore pressure, all of which are used to obtain information about subsurface stratigraphy. The accelerometers can be calibrated to function as deviation sensors so that the cone can be accurately located. However, in standard cone penetration testing the accelerometers are rarely used for this purpose, and therefore the uncertainties associated with these measurements has not been well established.

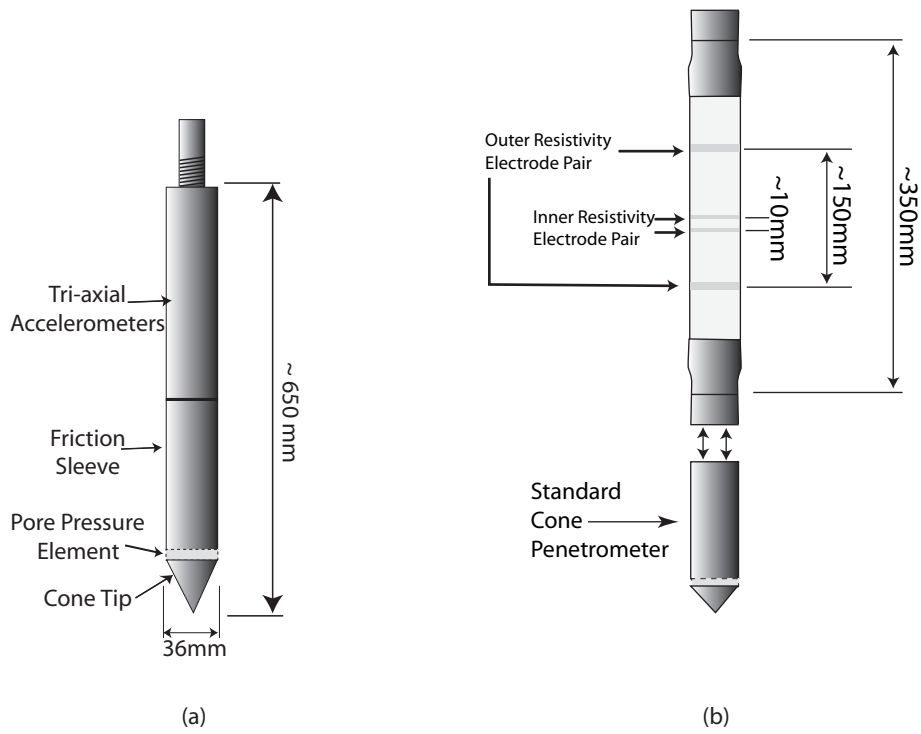


**Figure 4.1 Schematics of a) a standard cone penetrometer and b) a resistivity cone.**

Of use for identifying zones of anomalous electrical conductivity, is the method referred to as resistivity cone penetrometer testing (RCPT) which utilizes a resistivity module containing two pairs of ring electrodes. What is referred to as the resistivity cone is shown schematically in Figure 4.1b and includes the resistivity module and the standard cone. To make a measurement, a high frequency (~1000 Hz) AC current is injected into one pair of electrodes, and the voltage is measured across the same pair of electrodes (Lunne et al., 1997). Figure 4.1b shows the two electrode pairs; the measurements are made for each electrode pair. The separation distance of the electrodes, along with the resistivity of the surrounding sediments, determines the volume sampled by the measurement. The module is 36.6mm in diameter, which is larger than the diameter of the standard cone to ensure good soil-electrode coupling. RCPT yields a high-resolution resistivity log in addition to the standard suite of cone data.

Recent work has highlighted the advantage of coupling geophysical imaging techniques with CPT. Narbutovskih et al. (1997) demonstrated the benefit of using CPT technology to emplace permanent vertical electrode arrays to monitor infiltration experiments using ERT. Their design proved successful, and showed the advantages in speed, cost and safety over borehole-based ERT. Jarvis and Knight (2000, 2002) used a vertical seismic profile, obtained using accelerometers mounted on a cone, to constrain the inversion of 2-D seismic shear wave reflection data, thus improving the quality of the subsurface velocity model. Motivated by these previous studies, we have developed an acquisition system that combines ERT and CPT so as to gain the benefits realized by these studies.

In this paper we present our new cone-based ERT (C-bert) system. We describe in detail a successful field test of this new approach, covering both the field procedures and the data processing/interpretation algorithms. We conclude with a synthetic example to demonstrate the potential of C-bert as a new way to obtain conductivity images of the subsurface.

## 4.2 Description of the Field Site

---

The field experiment was conducted at the BC Hydro Kidd2 research site in Richmond, British Columbia, Canada. The site is immediately adjacent to the Fraser River and has a zone of saltwater intrusion, extending well into the site (Neilson-Welch 1999). Kidd2 is a very well documented site, having been the focus of several geotechnical, geophysical and hydrogeologic studies. Work on the site has included multiple cone penetrometer tests, multiple hydrogeologic well installations, various geophysical surveys and the analysis of numerous core samples (Hofmann 1997; Hunter et al. 1998; Jarvis et al. 1999; Neilson-Welch, 1999; Neilson-Welch and Smith, 2001; Jarvis and Knight 2000, 2002).

The Kidd2 site is composed of Holocene sediments deposited during the progradation of the Fraser River (Clague et al., 1983). Figure 4.2 is a cross-section through the area around the Kidd2 site, showing the five hydrostratigraphic units defined by Neilson-Welch and Smith (2001); these units are described in Table 4.1. Also shown in Figure 4.2 is the approximate extent of the saltwater intrusion. Imaging the conductivity structure to a depth of 30 m was defined as the objective of our C-bert field test.

**Table 4.1: Kidd2 Hydrostratigraphic units (after Neilson-Welch and Smith, 2001).**

<b>Unit Designation</b>	<b>Approximate Depth (m)</b>	<b>Description</b>
1	1-3.5	Clayey silt: clayey silt with trace fine sand laminations.
2	3.5 – 9	Silty sand: fine- and medium-grained sand with interbeds of clayey silt, sandy silt, and fine sand.
3	9-12	Fine and medium sand: includes interbeds of silt and fine sand.
4	12-22	Medium sand: uniform medium sand with trace interbeds of silts.
5	>22	Silty clay: includes thin laminations of silt

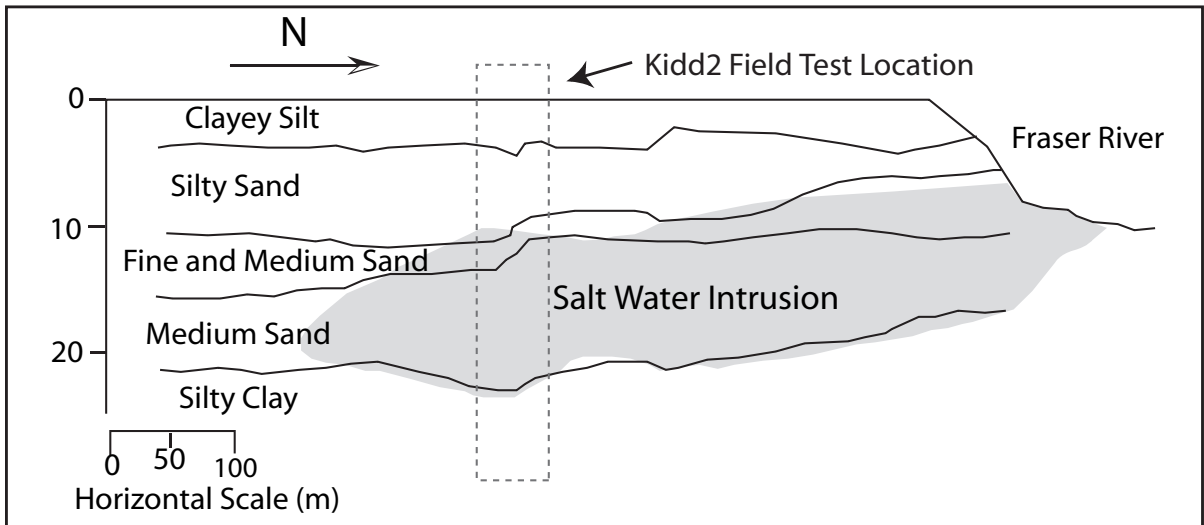
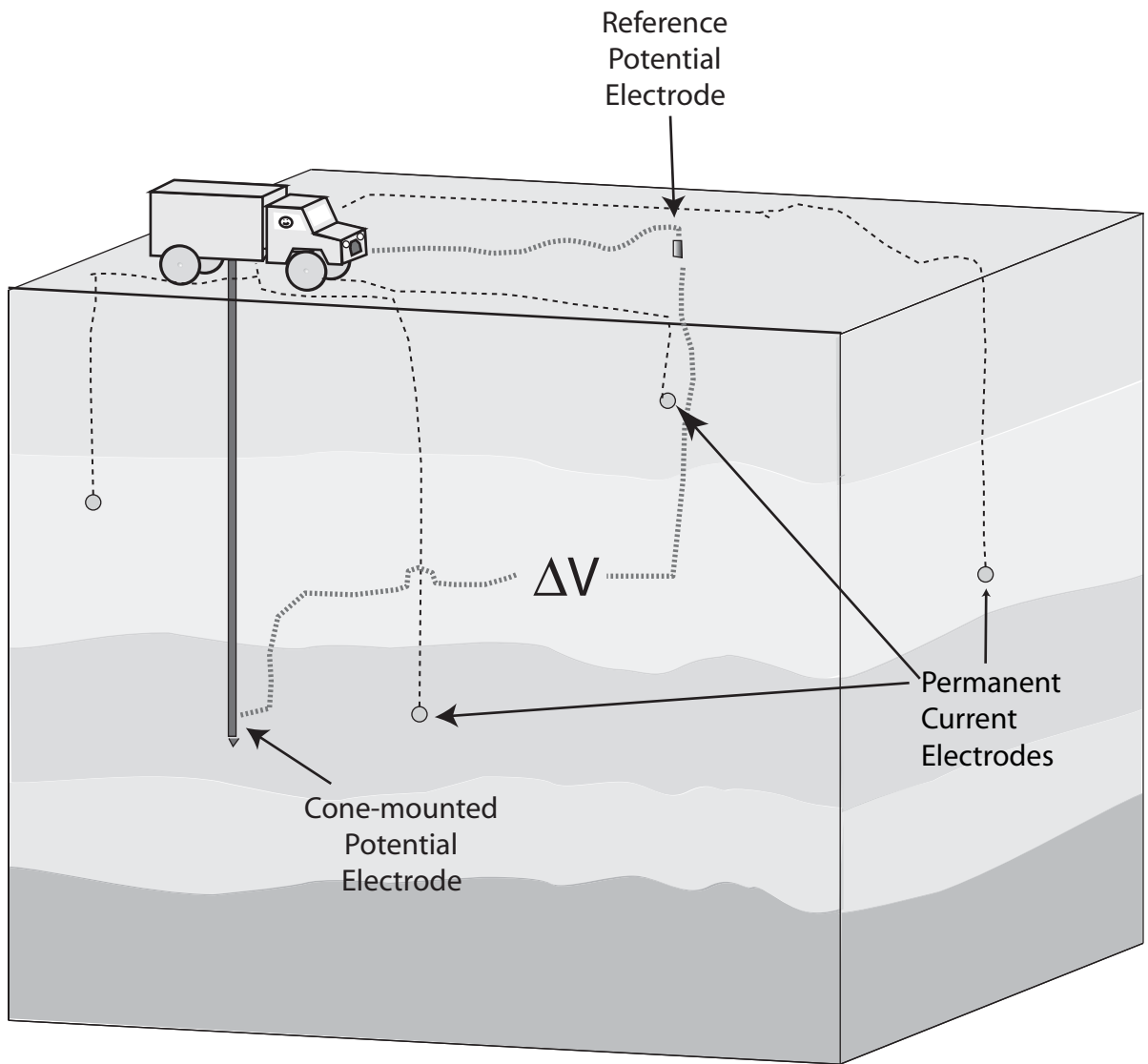


Figure 4.2 A cross-section of the Kidd2 site, with the approximate boundary of the salt water intrusion overlaid (after Neilson-Welch and Smith, 2001).

### ***4.2.1 Kidd2 C-bert Experiment***

Figure 4.3 is a schematic that illustrates the basic components of the C-bert system used at the field site. The survey area was 35 m x 30 m (in the north-south and east-west directions respectively). At nine locations on the grid, we used a cone truck to emplace permanent current electrodes in the subsurface. Once the current electrodes were in place, we pushed a resistivity cone into the ground and began the process referred to as C-bert. We acquired data in the standard RCPT mode, using the outer pair of electrodes on the resistivity module to obtain a 1D resistivity profile. At regular depth intervals (every 1-2m), the cone was stopped and resistivity tomography measurements were made. To do this, current was injected into a pair of the permanent current electrodes. The potential drop was measured between a surface reference potential electrode, and the inner electrodes on the resistivity module (i.e. the cone). This form of measurement was repeated for all independent current pairs. The cone was then pushed to the next interval, and the procedure repeated. This continued until the cone reached approximately 30 m. The truck was then moved, and the experiment repeated at a different location. Below we describe in detail this field experiment.



**Figure 4.3: Schematic of a cone-based resistivity tomography system. The current electrodes are permanently emplaced prior to C-bert testing. Potential measurements are made using the cone-mounted potential electrode and can thus be made anywhere in the volume.**

#### ***4.2.1.1 Description of Cone Truck***

We used the cone truck from Department of Civil Engineering at the University of British Columbia (UBC). The UBC cone truck is a self-contained laboratory with all of the equipment that was needed for the calibration and deployment of the resistivity cone.

In an effort to reduce sources of electrical noise during C-bert measurements, the cone truck was electrically isolated from the ground and the cone rods. The hydraulic jack pads, which allow the truck to be lifted and leveled, are large steel plates, approximately 1m x 2m x 0.5m. In order to isolate the truck from the ground we placed 2mm thick PVC mats under the jack pads. Another concern were the two metal guides that keep the cone rod centered and aligned with the hydraulic rams. In order to isolate the truck from the cone rods plastic guides were used.

#### ***4.2.1.2 Description of the Resistivity Cone***

The resistivity cone used in our study contained a standard cone and a resistivity module built by UBC. There are four brass ring electrodes on the module, arranged as two electrode pairs, one pair separated by ~10 mm, the other by ~ 150 mm. We used only the electrode pair separated by 150 mm to make the RCPT measurements. This electrode pair was calibrated using a technique similar to that described in Campanella and Weemees (1990). The resistivity cone was immersed in a 2 m x 2 m x 1.5 m water tank. Sodium chloride (NaCl) was added to the tank; the resistivity of the water was measured with a conductivity probe; and the voltage measured across the cone electrodes. This procedure was repeated ~20 times for different concentrations of NaCl. We observed a linear relationship between the cone voltage measurements and the probe-measured resistivity of the water allowing us to define the calibration factor needed to obtain resistivity values from our cone measurements.

Making subsurface ERT measurements requires a potential electrode below the surface. A key part of the C-bert concept is the use of an electrode, pushed into the subsurface on the resistivity cone, as the subsurface potential electrode. We modified the resistivity module on the cone so that the inner electrode pair functioned as a single,

isolated electrode. The C-bert system thus included the use of the outer electrodes on the resistivity module for resistivity logging, and the use of the inner electrodes for ERT measurements.

In addition to the two forms of resistance measurements, we acquired the standard suite of cone measurements. Once at the field site, the sensors in the standard cone were calibrated and the pore pressure sensor saturated as described in Lunne et al. (1997).

#### ***4.2.1.3 Design and Emplacement of Permanent Electrodes***

Figure 4.4 shows the plan of the survey grid, 35 m x 30 m, covering the Kidd2 site. On this plan view are shown the locations and depths of all the permanent electrodes. Also shown are the locations of 39 potential electrodes placed at the surface. These electrodes were 20 cm stainless steel stakes, hammered ~15 cm into the ground. These electrodes served to measure the potential field at the surface due to the permanent current electrodes. In addition, two of these electrodes (at the north-west and south-east corners of the grid) served as reference electrodes for the measurements made with the cone-mounted potential electrode.

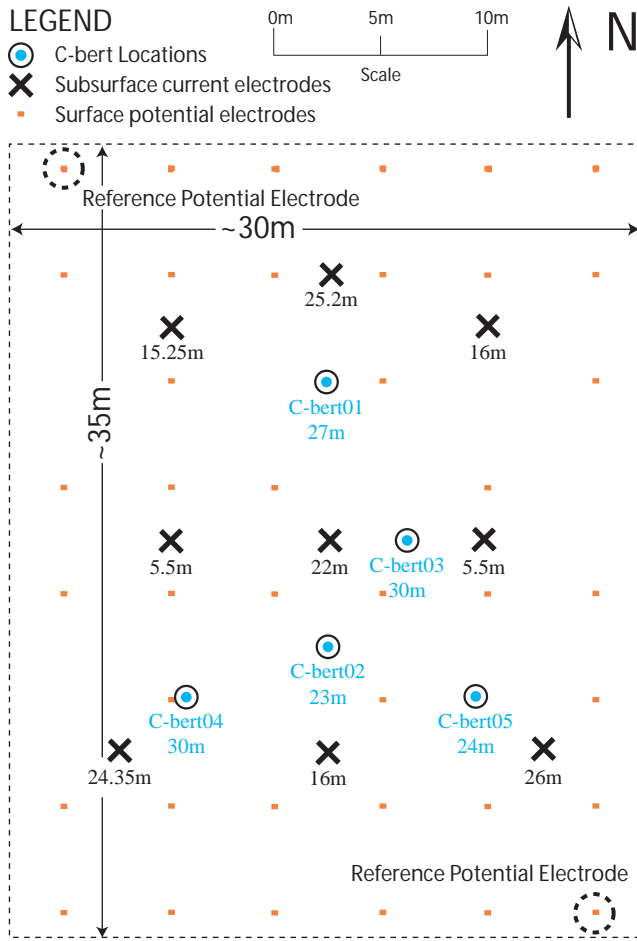
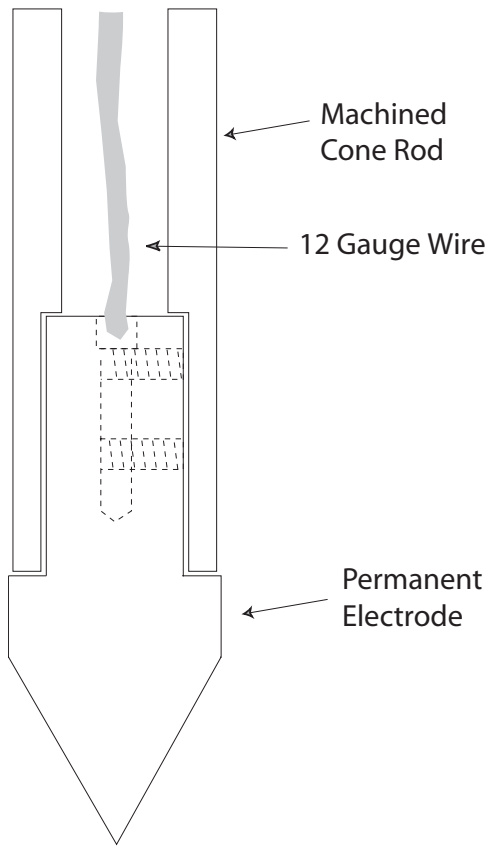


**Figure 4.4 Kidd2 survey map. The surface grid consisted of 39 electrodes. The locations of the 9 permanent current electrodes are indicated by the 'X'; the depth directly below the 'X' is the depth of emplacement. C-bert data were acquired at 5 locations, labeled C-bert01 through C-bert05. The maximum depths reached in the C-bert data acquisition are listed below the location.**

The current electrodes, pictured in Figure 4.5, were designed to be emplaced using the cone truck. Each electrode, machined out of 300-series stainless steel, has a conical tip with an apex angle of  $60^\circ$ , a maximum diameter of 41 mm and an overall length of 104 mm. A 12 gauge tinned copper wire was attached to the tip. The wire was held in place using two stainless setscrews. The resistance of the wire was  $\sim 5$  mOhm/m. The cable receptacle on the electrode was sealed using marine grade silicon sealer to minimize corrosion between the cable and the electrode. As shown schematically in Figure 4.5b, each electrode was inserted into a hollow cone rod that had a machined receptacle at one end. The electrode cable was threaded through the required number of cone rod sections, and the assembly was pushed into the subsurface with the electrode held in place by the force acting on the tip. Upon reaching the desired depth, the cone rod was retracted, leaving the electrodes in place.

Nine permanent current electrodes were emplaced at subsurface locations using the cone truck. As seen in Figure 4.4, two electrodes were placed at a depth of 5.5m, in the upper fresh water zone; three in the saltwater zone, between 15 and 16m; three in the silty clay between 25 and 26m; and one close to the interface between the saltwater zone and the silty clay. We were able to emplace all of the current electrodes in one day using the UBC cone truck (which is considerably slower than a commercial CPT rig). At the surface a small section of 6 in-diameter PVC casing was driven into the ground around the electrode cable and the casing capped with a screw-on lid. This protected the electrode leads, keeping them available for future repeat measurements.



(a)

(b)

**Figure 4.5 (a) Schematic of Permanent electrode seated in deployment rod. (b) Permanent current electrode.**

#### ***4.2.1.4 Data Acquisition***

The initial phase of the C-bert data acquisition involved obtaining surface measurements with the 39 surface electrodes. This was done using a Syscal R1-Plus 200 watt resistivity meter. The unit cycled through the 36 independent subsurface current electrode pairs, while measuring the potential field at all the surface electrodes. These surface data were directly incorporated into the C-bert data set.

As shown in Figure 4.4, we collected C-bert data at five locations with the depth of the cone holes ranging from 23m to 30m. At each location, the data acquisition involved two components: acquisition of the standard RCPT data (tip resistance, sleeve friction, induced pore pressure and resistivity), and acquisition of the tomographic data using the permanent subsurface current electrodes, the surface reference electrodes, and cone-mounted electrode.

At each C-bert location, the resistivity cone was pushed into the ground using the cone truck, obtaining standard RCPT data, with measurements every 2.5cm. These data yield high resolution resistivity and stratigraphy depth logs. At all five of the C-bert locations, we successfully acquired the standard suite of CPT data, and at four of the locations obtained high resolution resistivity logs. In the first hole (Cbert-01) we experienced a problem with the resistivity log, so had to discard the data.

Every 1m for C-bert01, and every 2m for C-bert02 – 05, ERT measurements were made using the Syscal resistivity meter. All permanent subsurface current electrodes and reference surface potential electrodes, and the cone-mounted potential electrode were connected to the control unit. The unit was programmed so as to cycle, at each depth sampling location, through the 36 independent current electrode pairs, injecting current into each pair and measuring the potential drop between the surface reference potential electrodes and the cone-mounted potential electrode. This resulted in 72 measurements per depth interval. The full C-bert survey took four days to acquire 6516 data points. Error estimates for the data were obtained by stacking ten measurements for each datum, and recording the standard deviation of these measurements. Typically, in resistivity experiments reciprocal measurements are used for determining the noise level.

Reciprocal measurements involve switching the current and potential measurement pairs for each location. The reciprocal measurements should yield identical results, and any variation provides quantification of error (Binely et al.,2002). However with the C-bert acquisition system, we are unable to inject current through the cone mounted electrode because the wiring and circuits are not designed to accommodate large amounts of current, and thus we could not obtain reciprocals. Table 4.2 is a compilation of the starting depths, depth intervals and finishing depths of the survey.

**Table 4.2 Testing depths for the tomography component of the C-bert experiment.**

	Starting Depth (m)	Maximum Depth (m)	Depth Interval (m)
C-bert01	3	27	1
C-bert02	2	20.5	2
C-bert03	4	30	2
C-bert04	4	30	2
C-bert05	2.25	24	2

## 4.3 Field Results and Interpretation

---

### 4.3.1 Resistivity Cone Data

Inversion of ERT is a highly nonlinear optimization problem. As such, an accurate starting model greatly increases the rate and probability of convergence of the inversion. Furthermore, this starting model is often used as the reference model in the regularization term of the inversion, and thus it will greatly affect the appearance of the resulting inversion. The suite of RCPT data, which is acquired as part of the C-bert experiment, provides valuable information about the subsurface, that can be used to build a good starting model. Furthermore, the resistivity data can be used as constraints within the inversion.

Figure 4.6 is a plot of the RCPT logs superimposed on a cross-section of the site. These data are from Cbert-05. The tip resistance, friction ratio (the percent ratio of sleeve friction to tip resistance) and induced pore pressure can be used to make interpretations of subsurface lithology. The most obvious lithologic feature in these logs is the top of the silty clay, which corresponds to a drop in tip resistance and an increase in friction ratio and induced pore pressure. More subtle is the boundary between the silty sand and the fine and medium sand. This boundary can be identified in both the friction ratio and pore pressure logs at approximately 10m below the surface, below which depth the logs no longer show small-scale fluctuations, which are indicative of the presence of silt. The resistivity log at this site is primarily an indicator of the extent of saltwater intrusion. From low values in the resistivity log, we see that the saltwater intrusion extends from approximately 10m to 23m; i.e. the saltwater intrudes the units of fine and medium sand. For this particular site we had a considerable amount of a-priori knowledge about the site, so the logs were not a necessity. It is clear, however, that the acquisition of these logs as part of the C-bert process is very useful for building a model of the subsurface.

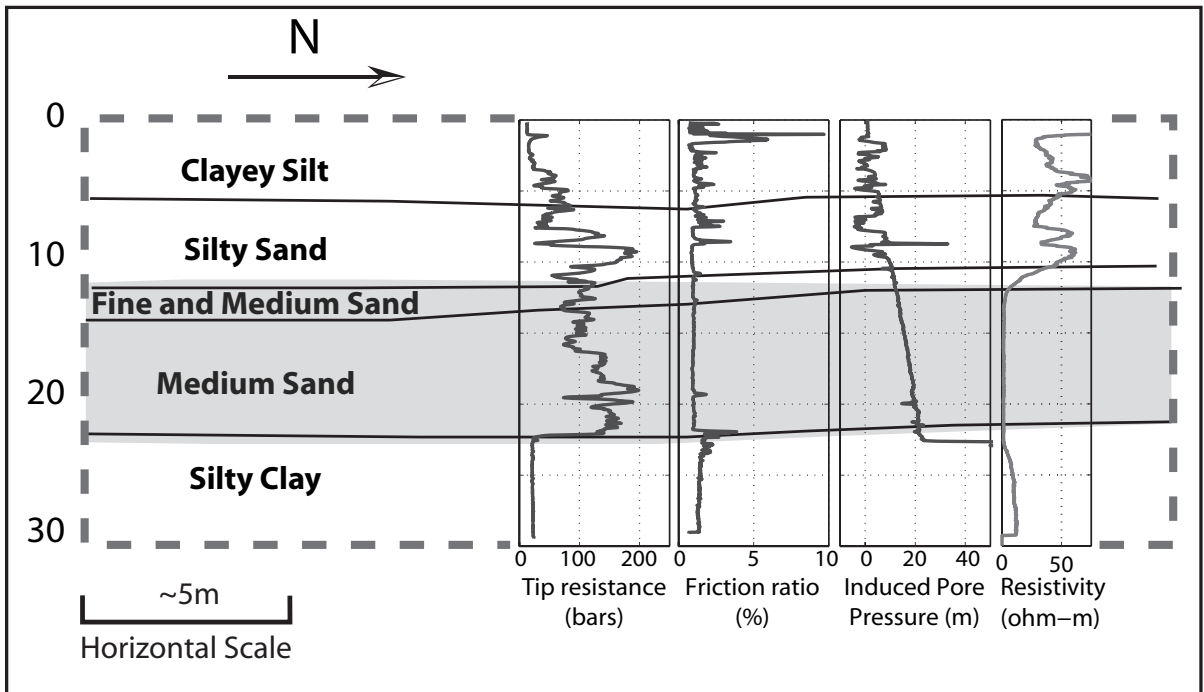


Figure 4.6 The RCPT data obtained from C-bert05 at Kidd2. The data are superimposed over the interpreted cross-section for the site.

#### 4.3.1.1 ERT Forward Modeling

ERT experiments yield a series of voltage measurements in response to a series of known input currents. From these data, we need to invert for the subsurface conductivity structure. The first step in this process involves the development of a mathematical framework, the forward model, that relates the recorded data to the conductivity structure:

$$-\nabla \cdot \sigma \nabla \phi = I(\delta(\mathbf{r} - \mathbf{r}_{s+}) - \delta(\mathbf{r} - \mathbf{r}_{s-})). \quad (4.1)$$

Equation 4.1 is the partial differential equation that relates the potential field ( $\phi$ ) to the input current ( $I$ ), from a dipole, through the conductivity structure of the medium ( $\sigma$ ). Here,  $\mathbf{r}_{s+}$  and  $\mathbf{r}_{s-}$  are the locations of the positive and negative current sources, respectively, and  $\delta(\mathbf{r} - \mathbf{r}_s)$  is the dirac delta function, centered at the current source location. In order to solve equation 4.1, the problem is approximated on a discretized grid, and solved numerically. We have chosen to discretize the system using a cell-centered, variable-grid, finite volume approach, similar to that presented by Haber et al. (2000a). This yields the discretized form of equation 4.1:

$$(\mathbf{D} \cdot \mathbf{S}(\mathbf{m}) \cdot \mathbf{G}) \mathbf{u} = \mathbf{A}(\mathbf{m}) \mathbf{u} = \mathbf{q}. \quad (4.2)$$

Here,  $\mathbf{D}$  and  $\mathbf{G}$  are matrices representing 3-D second order finite difference divergence and gradient operators, respectively. The difference operators are applied across the entire model space, including the boundary cells. This naturally enforces no-flux boundary conditions at the edges of the model space. Although these boundary conditions are not as ideal as the impedance matched boundary conditions presented in Zhang et al. (1995), they naturally fall out of the discretization, they are numerically efficient to solve, and their effects fall off as  $\frac{1}{r^2}$ . Furthermore, a variable grid discretization scheme allows us to push the boundaries far away from our region of interest without creating a prohibitively large model. In equation 4.2,  $\mathbf{S}$  is a diagonal matrix that contains the harmonic average of the conductivity of each cell face along the main diagonal.  $\mathbf{u}$  and  $\mathbf{q}$  are potential and source vectors respectively, defined at the centers of the volumes. From equation 4.2 we see that in order to predict the potential field, we need to solve for  $\mathbf{u}$  as shown in equation 4.3:

$$\mathbf{u} = \mathbf{A}(m)^{-1} \mathbf{q}. \quad (4.3)$$

The operator matrix,  $\mathbf{A}$ , is sparse and banded; therefore, equation 4.3 can be rapidly solved using preconditioned iterative methods.

For this work we used an incomplete LU decomposition for pre-conditioning. This is an expensive pre-conditioner to calculate; however, as  $\mathbf{A}$  remains the same for all our source terms, we can amortize the cost over all the source vectors. The solution of equation 4.3 was then iteratively determined, for each source vector, using a bi-conjugate stabilized gradient (Bicgstab) algorithm (Saad, 1996).

#### 4.3.1.2 ERT Inversion

For this work we chose to use an inexact Gauss-Newton inversion routine, similar to that described in Haber et al. (2000b). The objective function that we wish to minimize is the following:

$$\min_{\mathbf{m}} \left\{ \frac{1}{2} \|\mathbf{W}_d (\mathbf{Q}\mathbf{u} - \mathbf{d}_{\text{obs}})\|^2 + \frac{\beta}{2} \|\mathbf{W}_m (\mathbf{m} - \mathbf{m}_{\text{ref}})\|^2 \right\} \quad (4.4)$$

where  $\mathbf{W}_d$  is the data weighting matrix;  $\mathbf{Q}$  is a linear interpolation operator that projects the potentials  $\mathbf{u}$  determined using equation 4.3 to the corresponding locations where data were acquired;  $\mathbf{d}_{\text{obs}}$  is a vector containing the observed data;  $\mathbf{W}_m$  is a model regularization matrix;  $\beta$  is the regularization parameter that balances the effect of data misfit and model regularization during the minimization;  $\mathbf{m}$  is our model at a given iteration, where the model parameters are  $\ln(\sigma)$ ; and  $\mathbf{m}_{\text{ref}}$  our reference model, and in the case of the Kidd2 data our starting model, defined from our resistivity logs.

For the field data described here  $\mathbf{W}_d$  is a matrix that contains the estimate of the absolute error along the main diagonal as follows:

$$\text{diag}(\mathbf{W}_d) = \frac{\mathbf{1}}{|\mathbf{d}_{\text{obs}}| \cdot SD(\mathbf{d}_{\text{obs}})} \quad (4.5)$$

where,  $SD(\mathbf{d}_{\text{obs}})$  is the standard deviation of the observed data, obtained from stacking measurements in the field. The regularization matrix  $\mathbf{W}_m$  is an anisotropic first derivative operator. This operator promotes various levels of flatness in the x,y and z directions. The diagonal of  $\mathbf{W}_m$  contains the relative weights of each model parameter, in particular it

contains weights that penalize model structure near our current electrode locations. For our work the regularization parameter,  $\beta$ , was set to at an initial value, and progressively decreased by a factor of 10 whenever the objective function was not reduced by at least 10% between iterations.

Using the inexact Gauss-Newton method we define a starting model,  $\mathbf{m}_i$  (in this case  $\mathbf{m}_{\text{ref}}$ ), that we hope is near the local minimum of equation 4.4. The expressions under the norms in equation 4.4 are linearized about this model, and we calculate a small model update ( $\delta\mathbf{m}$ ) to obtain our new solution. The update is applied to the new model as follows:

$$\mathbf{m}_{i+1} = \mathbf{m}_i + \alpha\delta\mathbf{m} \quad (4.6)$$

where  $\mathbf{m}_{i+1}$  is the new model, and  $\alpha$  is a line search parameter. The form of the Gauss-Newton update is as follows:

$$\delta\mathbf{m} = -\underbrace{\left(\mathbf{J}^T\mathbf{J} + \beta\mathbf{W}^T\mathbf{W}\right)^{-1}}_{\mathbf{H}^{-1}} \underbrace{\left(\mathbf{J}^T\left(\mathbf{Q}\mathbf{A}(\mathbf{m})^{-1}\mathbf{q} - \mathbf{d}_{\text{obs}}\right) + \beta\mathbf{W}^T\mathbf{W}\left(\mathbf{m} - \mathbf{m}_{\text{ref}}\right)\right)}_{\mathbf{g}} \quad (4.7)$$

where  $\mathbf{J}$  is the Jacobian or sensitivity matrix,  $\left(\frac{\partial\mathbf{d}}{\partial\mathbf{m}}\right)$ . The matrix  $\mathbf{H}$  is an approximation to the Hessian while  $\mathbf{g}$  is the gradient of our objective function. It should be noted that  $\mathbf{J}$  is a very large, dense matrix and thus from a computational point of view we want to avoid explicitly forming the matrix. However, it was shown in Haber et al. (2000b) that  $\mathbf{J}$  has the form:

$$\mathbf{J} = \mathbf{Q}\mathbf{A}^{-1}\mathbf{B} \quad (4.8)$$

where  $\mathbf{B} = \frac{\partial(\mathbf{A}(\mathbf{m})\mathbf{u})}{\partial\mathbf{m}}$ . The matrices  $\mathbf{B}$  and  $\mathbf{Q}$  are sparse matrices. We can see from equation 8 that we can calculate the product of the sensitivity matrix and a vector (or its adjoint) by solving the forward (described by equation 4.3) or adjoint problems along with two matrix multiplications. Because of this, we do not compute the Hessian explicitly but instead perform a series of matrix-vector products. The procedure for calculating  $\mathbf{J}$  is as follows:

1. Calculate  $\mathbf{w} = \mathbf{B} \cdot \mathbf{v}$

2. Solve  $\mathbf{x} = \mathbf{A}(\mathbf{m})^{-1} \mathbf{y}$  using Bicgstab.
3. Calculate  $\mathbf{J} \cdot \mathbf{v} = \mathbf{Q} \cdot \mathbf{x}$

With this in mind, a natural way to solve equation 4.7 is by using the preconditioned conjugate gradient method, where only matrix-vector products need to be computed. Note that each PCG iteration involves one forward solve and one adjoint solve. In addition, we have to perform one forward solve and one adjoint solve in order to evaluate the gradient  $\mathbf{g}$  (Haber et al., 2000b).

The data from the RCPT logs, obtained coincidentally with the C-bert data, were included as constraints in the inversion. These data can be added to the inversion by either setting the values of the cells to their known value or as softer information by using them in the penalty function  $\mathbf{W}_m$ . For our work, we chose to include these data in the penalty function; this is done by applying a large model weight at the RCPT locations, and applying no model update at these locations.

After each model update, the objective function is reevaluated, and the line search parameter,  $\alpha$ , is determined to ensure sufficient decrease of the objective function.  $\alpha$  starts at a fixed value (usually one), and is reduced until the objective function satisfies the Armijo inequality:

$$\Phi(\mathbf{m}_{i+1}) = \Phi(\mathbf{m}_i + \alpha \delta \mathbf{m}) \leq \Phi(\mathbf{m}_i) + c_1 \alpha \nabla \Phi(\mathbf{m}_i)^T \delta \mathbf{m} \quad (4.9)$$

where  $c_1$  is a constant, that in practice takes a very small value, for example  $10^{-4}$  and  $\Phi$  is the value of the objective function. After the line search, if equation 4.4 has been minimized to the desired tolerance the inversion is terminated, otherwise another iteration is performed. Additionally, we use the gradient term  $\mathbf{g}$  in equation 4.7 as a convergence indicator; once the gradient  $\mathbf{g}$  becomes small, no further improvements can be obtained with additional iterations. For our field data, we had an excellent starting model from the RCPT logs, and thus convergence was usually obtained within three to five iterations of equation 4.7. This highlights another advantage of C-bert: we have high resolution logs to construct a good starting model. We note that these inversions result in non-unique solutions using an informed starting model, an informed reference model and resistivity logs as constraints yields better results than using any of this a-priori information independently.

### 4.3.1.3 The Cone Effect

One of the major challenges in working with C-bert data is that the cone, and the cone push rods are highly conductive and represents a large conductivity perturbation to the potential field near the measurement location. Unfortunately, explicitly modeling the cone-effect during inversions is computationally cost prohibitive for three reasons. First, the forward problem involves a solution at many spatial scales: i) in order to remove boundary effects in equation 4.3, the boundaries are extended, so the model space spans hundreds of meters in the x, y, and z directions; ii) we have an inherent field scale at which we would like to obtain information (i.e. the survey scale); and iii) the cone scale, which requires discretization, at the sub-centimeter scale. The multiscale nature of the problem results in a forward problem, that even with a variable grid mesh can lead to forward problems that have millions of cells. Second, the cone has a conductivity of approximately  $10^6$  S/m. Consequently including it in the forward operator can greatly increase the condition number of the matrix, making the problem difficult to solve. Third, at each new measurement location, the conductivity structure of the model space is slightly different from the previous location, and thus there is a new forward model required for each cone location. The first two issues make running a single, realistic forward model a challenging task. The third issue, that of being faced with thousands of these forward models in the inversion, makes explicitly modeling the cone infeasible.

In an effort to address the first two issues regarding computational difficulties we developed a grid refinement method for solving the forward problem. This method allows us to realize a decrease in the computational time required to solve the forward problem by an order of magnitude. Our solution approach, iteratively determined boundary conditions (IDBC), is described schematically in Figure 4.7. We begin by defining a fine scale conductivity model for which we would like to determine the potential field. The first step of IDBC is to define a starting grid that is coarser than our desired scale, with the boundaries far away from our region of interest. Using the conductivity values from our predefined fine scale conductivity structure, we parameterize the coarse grid by upscaling from the fine structure. We solve for the potentials ( $\mathbf{u}_c$ ) on the coarse grid. A second grid ( $\mathbf{g}_m$ ) is then constructed with cell dimensions that are half of  $\mathbf{g}_c$ , and the

known conductivities are upscaled onto this grid.  $\mathbf{u}_c$  is then interpolated onto this new grid, and the potentials in the boundary cells are fixed at the interpolated  $\mathbf{u}_c$  values. The boundary conditions of this new system are now set to the interpolated  $\mathbf{u}_c$  values, and are thus more accurate than the original no-flux boundaries. We note that the new grid, though higher resolution than the first grid, spans a smaller space, and thus has the same computational cost as the coarse grid. We solve for the potentials on this second grid, which yields the potential field  $\mathbf{u}_m$ . Successive grids are created, parameterized, and solved until we reach our desired level of discretization. Although this approach results in many forward solves, each model is comparatively small with respect to solving the entire finely discretized model at once, and the approach results in substantial computational savings. We note, that this approach bears some resemblance to the multigrid method in the sense that we solve the problem on progressively finer grids. However, multigrid is an iterative solver for the linear system, the IDBC solution is a method for determining more accurate boundary conditions, and thus minimizing the size of the linear system we are solving. IDBC still requires an iterative solver to obtain a solution to the linear system.

Figure 4.8 is a plot of the results for a dipole in a 3-D homogenous 100 ohm-m conductivity structure. The potential fields were determined using the fully parameterized approach as well as the IDBC approach. The potentials were converted to resistivities using the geometric factor, obtained from the analytical solution to a dipole in a homogenous half-space. Both solutions have an average resistivity that is slightly above 100 ohm-m. Using the IDBC the apparent resistivity has approximately 1% greater error than the full solution; however since the noise level in the data is usually larger than this, the error does not affect our inverse calculations, giving us an order of magnitude increase in speed.

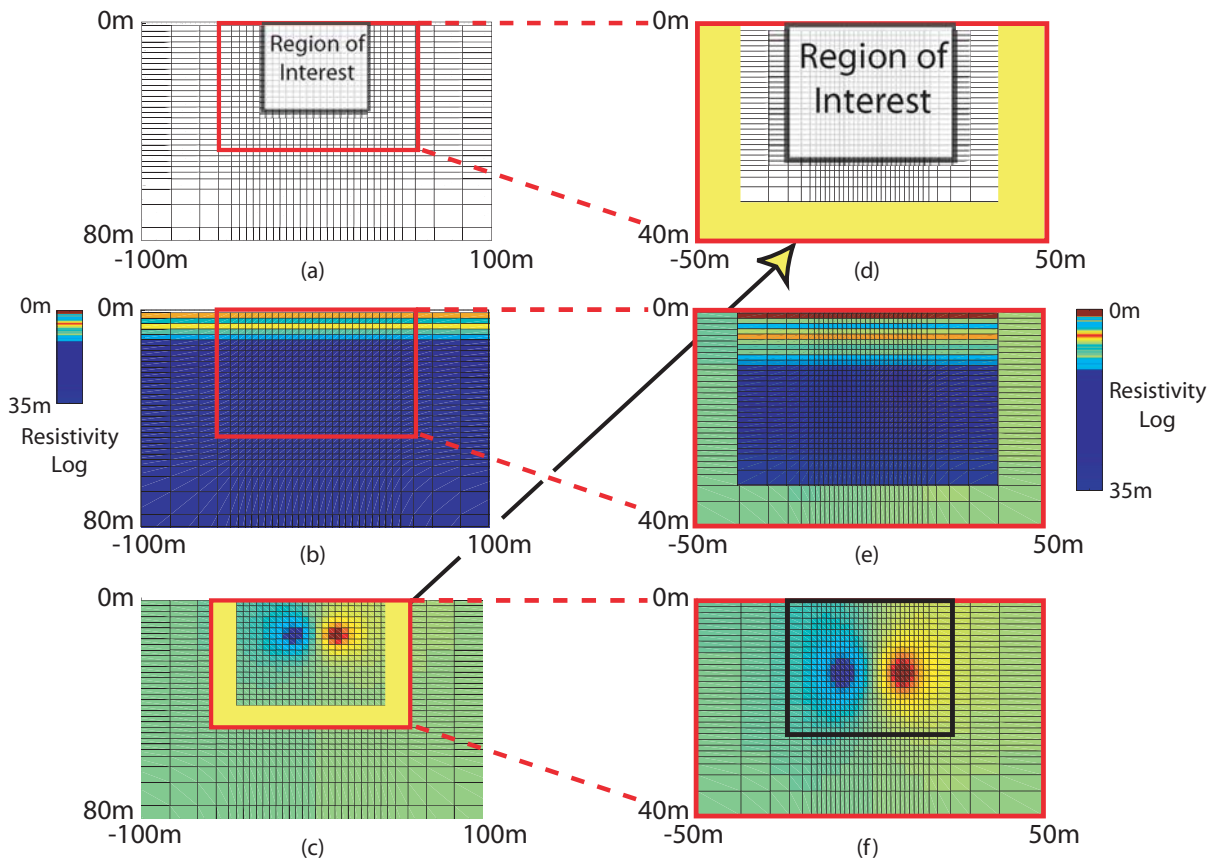


**Figure 4.7 Schematic of the iteratively determined boundary conditions approach (IDBC), using two iterations. (a) large coarse grid is defined with boundaries sufficiently far away so as not to influence the region of interest (ROI). (b) High resolution resistivity logs, or the fine scale 3-D resistivity structure, are upscaled onto the coarse grid. (c) The potential field is determined at every point in the volume. (d) Fine scale grid defined with cell dimensions that are  $\frac{1}{2}$  of coarse grid. Potentials from the coarse grid solution (the yellow region in frame c) are interpolated onto the boundary cells of the fine grid. (e) High resolution resistivity logs are upscaled onto the new grid; however, the boundary cells remain fixed potential boundaries. (f) Final solution is computed on the fine scale grid yielding a fine scale solution in the ROI.**

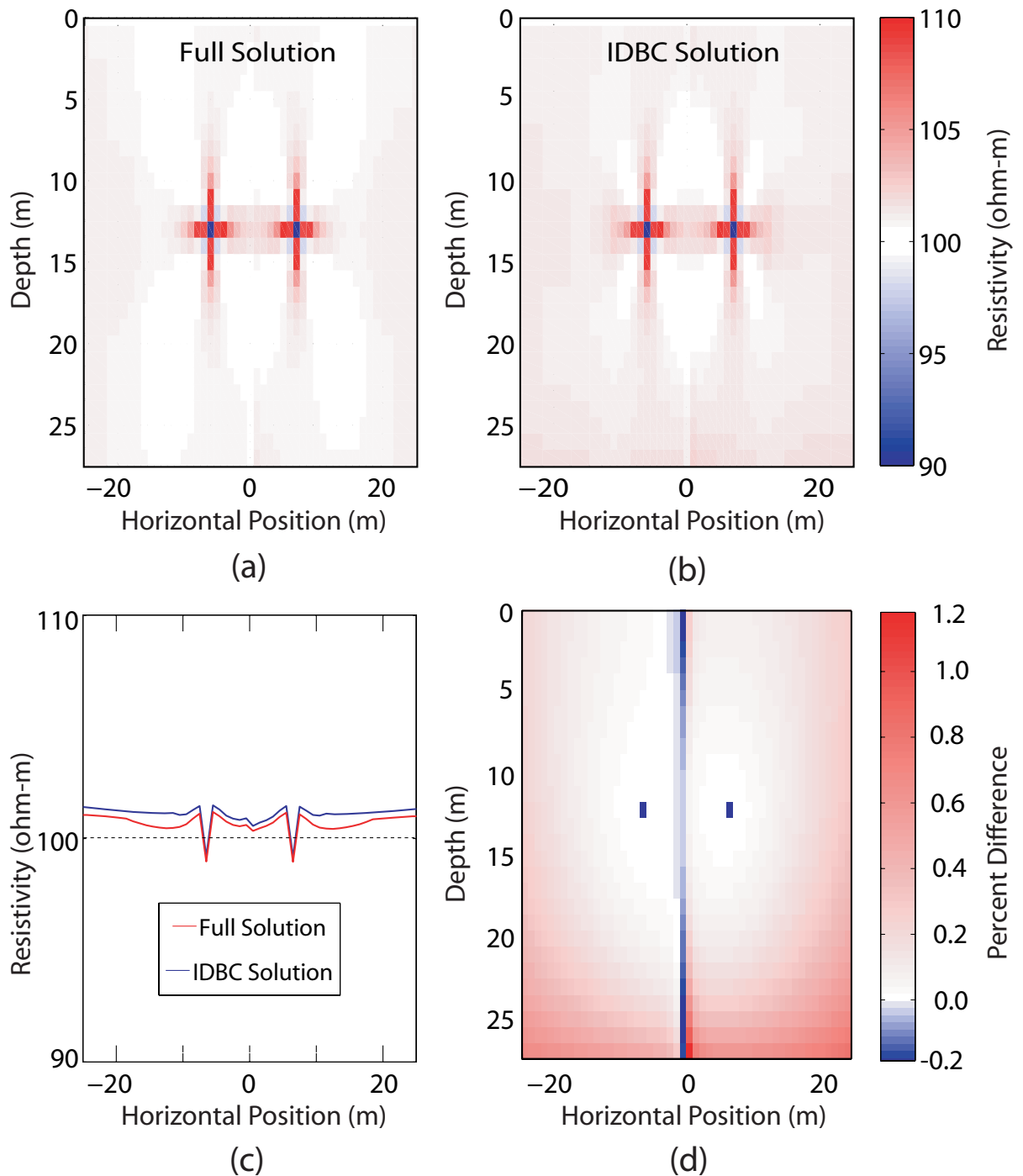


**Figure 4.8 Comparison of IDBC solution versus the fully parameterized solution; the solutions are for a dipole in a homogenous 100 Ohm-m media. The geometric factor has been applied to the potential fields and thus the entire image should be 100 Ohm-m. (a) 2d slice through the center of the 3d solution using the full solution method. (b) The same slice as in (a) solved using the IDBC approach. (c) The vertically averaged resistivities from the images in (a) and (b). (d) A percent difference map between images (a) and (b).**

Although the IDBC approach allowed substantial computational savings, it is still too slow to explicitly solve for the cone effect. As mentioned above, the third issue with determining the cone effect explicitly in the inversion requires that we calculate a correction for each measurement location during each inverse iteration. Practically speaking this would require tens of thousands of forward solves to complete the inversion. Recognizing this, we used IDBC as a way of calculating an approximate correction for the cone effect.

Assuming that  $\sigma_c \gg (\sigma_0 \text{ and } \sigma_1)$ , where  $\sigma_c$  is the conductivity of the cone;  $\sigma_0$  is the layered conductivity structure obtained from the resistivity log; and  $\sigma_1$  is a conductivity structure that is locally (i.e. near the cone) the same as  $\sigma_0$ , but may differ at a distance; we can develop the following correction:

$$u_i(\sigma_1 + \sigma_c) - u_i(\sigma_1) = u_i(\sigma_0 + \sigma_c) - u_i(\sigma_0) \quad (4.10)$$

where  $u_i$  is the potential for at a given model point. Following from equation 4.10 we obtain:

$$u_i(\sigma_1 + \sigma_c) = 1 + \frac{u_i(\sigma_0 + \sigma_c) - u_i(\sigma_0)}{u_i(\sigma_1)} \quad (4.11)$$

assuming that near the cone  $\sigma_1 \approx \sigma_0$ , which is reasonable because  $\sigma_0$  was derived from the resistivity logs, we can approximate the cone effect with the following equation:

$$u_i(\sigma_1 + \sigma_c) \approx 1 + \underbrace{\frac{u_i(\sigma_0 + \sigma_c) - u_i(\sigma_0)}{u_i(\sigma_0)}}_{C_i} \quad (4.12)$$

where  $C_i$  is the cone correction factor.

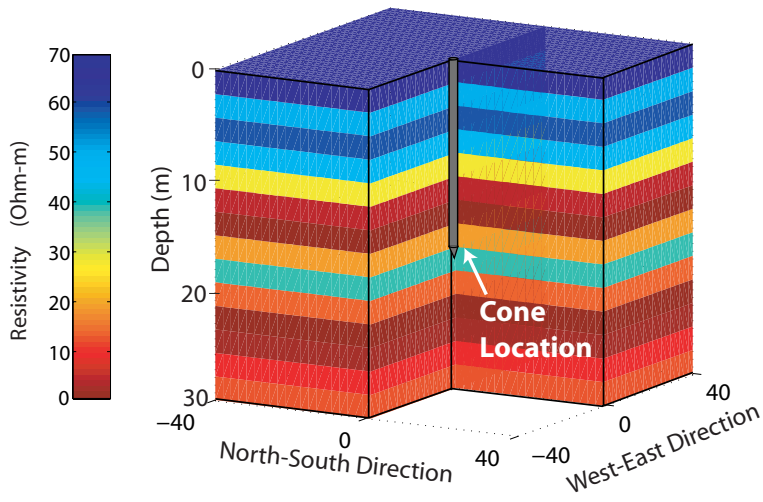
From equation 4.12 we see that by comparing the potential field obtained from a forward model,  $u_i(\sigma_0 + \sigma_c)$ , that explicitly includes the conductivity structure of the cone, with the potentials obtained from a model that does not include the cone conductivity structure,  $u_i(\sigma_0)$ , we can determine the modeling error associated with neglecting the cone in our model. For a new conductivity structure,  $\sigma_1$ , that is a perturbation about  $\sigma_0$ , we can use equation 4.12 to approximate the potential field

including the cone effect,  $u_i(\sigma_1 + \sigma_c)$ , without explicitly calculating the cone effect for the new conductivity structure  $\sigma_1$ . As described above, the inversion algorithm is based on a linearization of the non-linear problem, and therefore we implicitly assume that our starting conductivity structure, for example  $\sigma_0$ , is close to the true conductivity. In the case of C-bert, this a reasonable assumption as our starting model,  $\sigma_0$ , is derived from the resistivity logs. With this in mind, we recognize that calculating the correction factor before the inversion is a reasonable approach because the starting model for our inversion is close to the final model. Thus if we calculate a correction factor for the starting model, it will be approximately correct for our final model. Moreover, forward modeling demonstrated that the magnitude of cone effect was largely a function of the conductivity structure immediately adjacent to the cone.

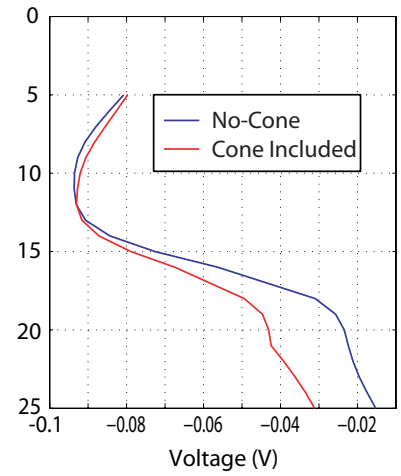
To practically implement this correction, we created a high resolution layered model, based on the RCPT log, for each C-bert surveys location. This model can be considered locally correct, as it is derived from the RCPT logs. Using IDBC we calculated the cone effect at all measurement locations for each cone profile, solving on a final grid that has cells around the cone location that are 10mm on a side. We then calculated the correction factor,  $C_i$ , as shown in equation 4.12. The correction factor was incorporated into the interpolation operator,  $\mathbf{Q}$ , described in equation 4.4, thereby approximating the cone effect when the potentials are mapped to the data locations in the inversion.

Figure 4.9a is an example of a resistivity structure we would obtain from a RCPT log. If we assume that the log represents a layered system, as depicted in Figure 4.9a, we can use the IDBC approach to calculate that C-bert data we would obtain, while pushing the cone into the subsurface, with and without explicitly including the cone and cone rods. Figure 4.9b shows the results from such an experiment for a signal current pair. As can be seen in Figure 4.9b, neglecting the presence of the cone significantly alters our calculated data. Using the data presented in Figure 4.9b, we can generate a cone correction factor, as described above, and apply this correction to a different data set. Figure 4.9c shows a resistivity structure, that is identical to the one presented in Figure 4.9a, except for the presence of a conductivity body a small distance from the cone location. As in Figure 4.9b, we present modeled data that considers the cone and modeled

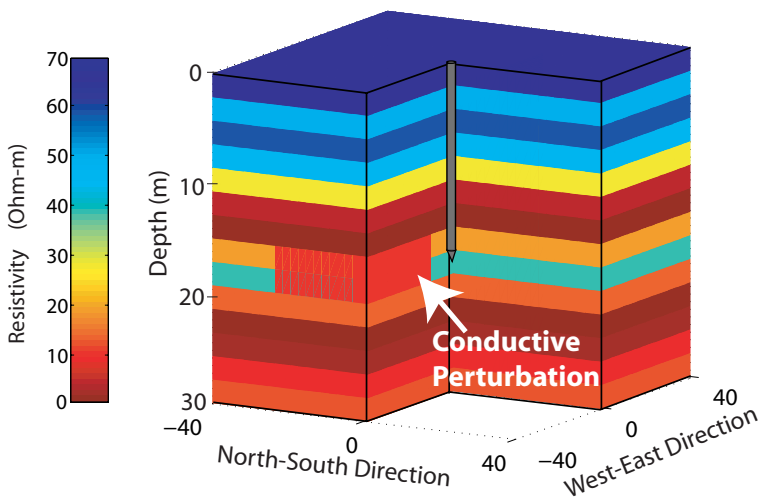
data that ignores the cone; in addition, we include the results of applying the cone correction to the data that does not include the cone. The corrected data set is a good approximation to the data that explicitly includes the cone. Although this approximation works well for this case, we stress that in the absence of a good local resistivity estimate, i.e. the resistivity logs, this approach will not work because the calibration is a linearization around the calibration model, and thus if the true model is far from the calibration model (i.e. the relationship becomes non-linear), the correction will fail.



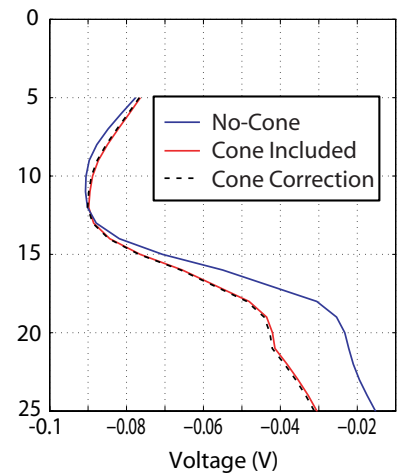
(a)



(b)



(c)



(d)

**Figure 4.9** (a) An example of a calibration resistivity structure. (b) Calculated data for the resistivity structure in (a). (c) A perturbed resistivity structure. (d) Data calculated for the resistivity structure in (c).

### ***4.3.2 Kidd2 Inversion Results***

For the Kidd2 data set, we parameterized the inversions on a 240,000 cell grid. The region of interest, a volume approximately 30m x 35m x 30m, contained approximately 74,000 cells with dimensions of 0.75m on a side. The remainder of the cells served to ensure that we encountered minimal boundary effects. We ran multiple inversions of the C-bert data that used slightly different regularization operators, as well as different initial guesses, and different starting values for the regularization parameter. The inversions tended to produce very similar results, and so we only show one of the results here.

The starting model we used was based on the four resistivity logs. Due to a problem with the RCPT logging system, the resistivity log from Cbert-01 was discarded. The model was generated by first vertically upscaling each of the logs to 0.75m grid cells, using geometric averaging. The four upscaled logs were arithmetically averaged in the horizontal direction to create a layered starting model. Following this, the model values at the four resistivity log locations were set to the values from the corresponding upscaled logs.

Figure 4.10 presents inversion results for the Kidd2 data set. From these results, we identify three resistivity units: the upper fresh water saturated region of clayey silt and silty sand, from approximately 1m to 10m; the saltwater intrusion from 10m to 22m; and the silty clay, below 22m. As can be seen from the five slices, the results are dominantly layered with small horizontal variations within each layer.

At approximately five meters deep in Figure 4.10c and 4.10d we see a low resistivity feature. As can be seen in Figure 4.10c, the RCPT log suggests that the resistivity should be higher than the inversion would suggest. A possible interpretation of these discrepancies could be the different frequencies at which the two data types were obtained, the resistivity log is obtained at 1000Hz while the imaging data are acquired at 4Hz. However, the work of Lesmes and Frye, 2001 indicates that the resistivity variation with frequency is quite small, and thus does not provide a suitable explanation. Closer examination of the CPT data (tip resistance, sleeve friction and induced pore pressure), indicates that there are some thin silty clay layers around 5.5m. The resistivity of there

layers is being averaged differently by the two resistivity techniques (the resistivity log and the inversion). The “true” resistivity likely lies somewhere between the values provided by the resistivity log and the inversion. Without the coincident data this interpretation would be difficult to make. Acquiring multiple data types is one of largest benefits of C-bert.

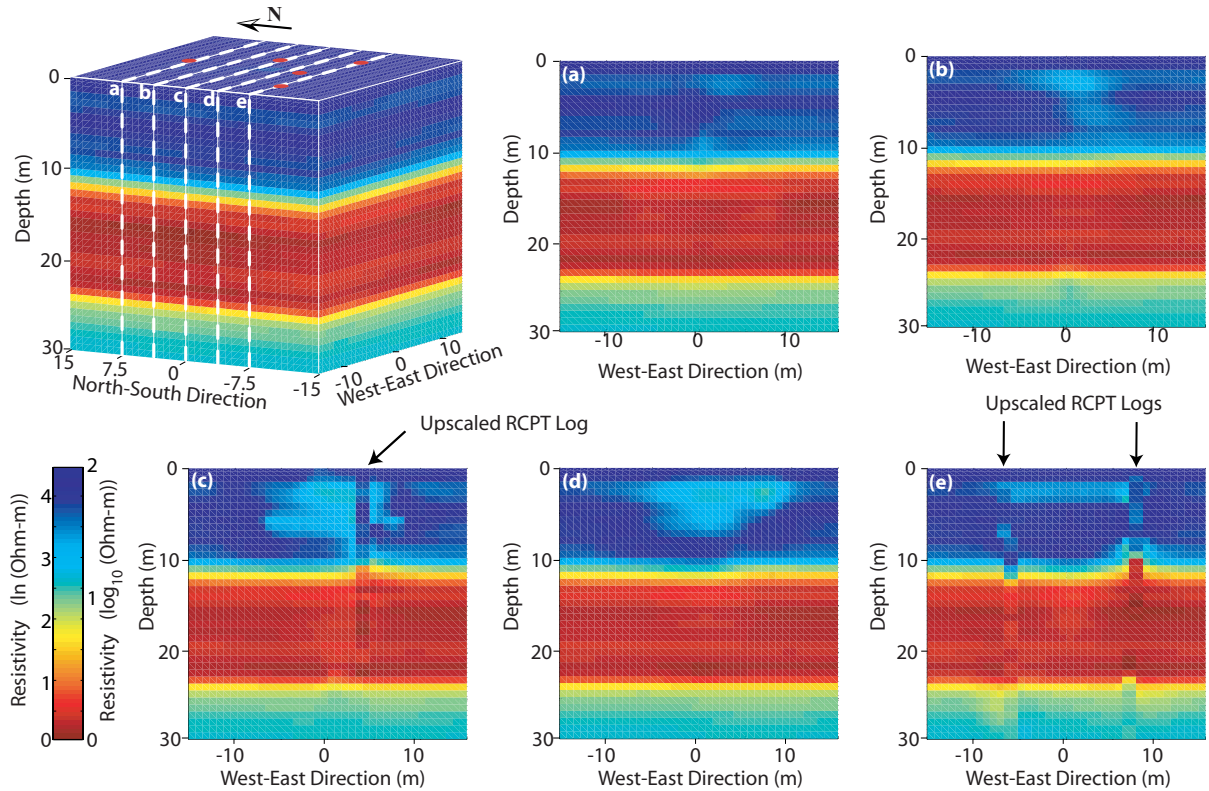


**Figure 4.10** Results from the inversions of the Kidd2 data set. Frames (a)-(e) are slices from the 3-D solution. In frames (c) and (e), the upscaled RCPT logs are superimposed over the inversion results. In the upper 10m of frame (c) there is a discrepancy between RCPT logs and the inversion results.

## 4.4 C-bert Numerical Experiment

---

While the results of the field test are very encouraging, we recognize that the large scale structure at the Kidd2 site is dominantly layered. We thus wanted to conduct a more challenging numerical experiment to further explore the potential benefits of C-bert.

Figure 4.11 is a schematic displaying the hypothetical field situation. A factory is suspected of leaking contaminants into the ground beneath the factory. The presence of the factory makes it impossible to perform a surface-based geophysical survey over the region of interest. As the plume does not extend laterally, direct sampling in boreholes would not indicate the presence of the contaminant. Furthermore, as this is a reconnaissance survey, we do not want to incur the costs and risks associated with installing boreholes. We therefore use C-bert to establish if indeed the factory is releasing contaminants.

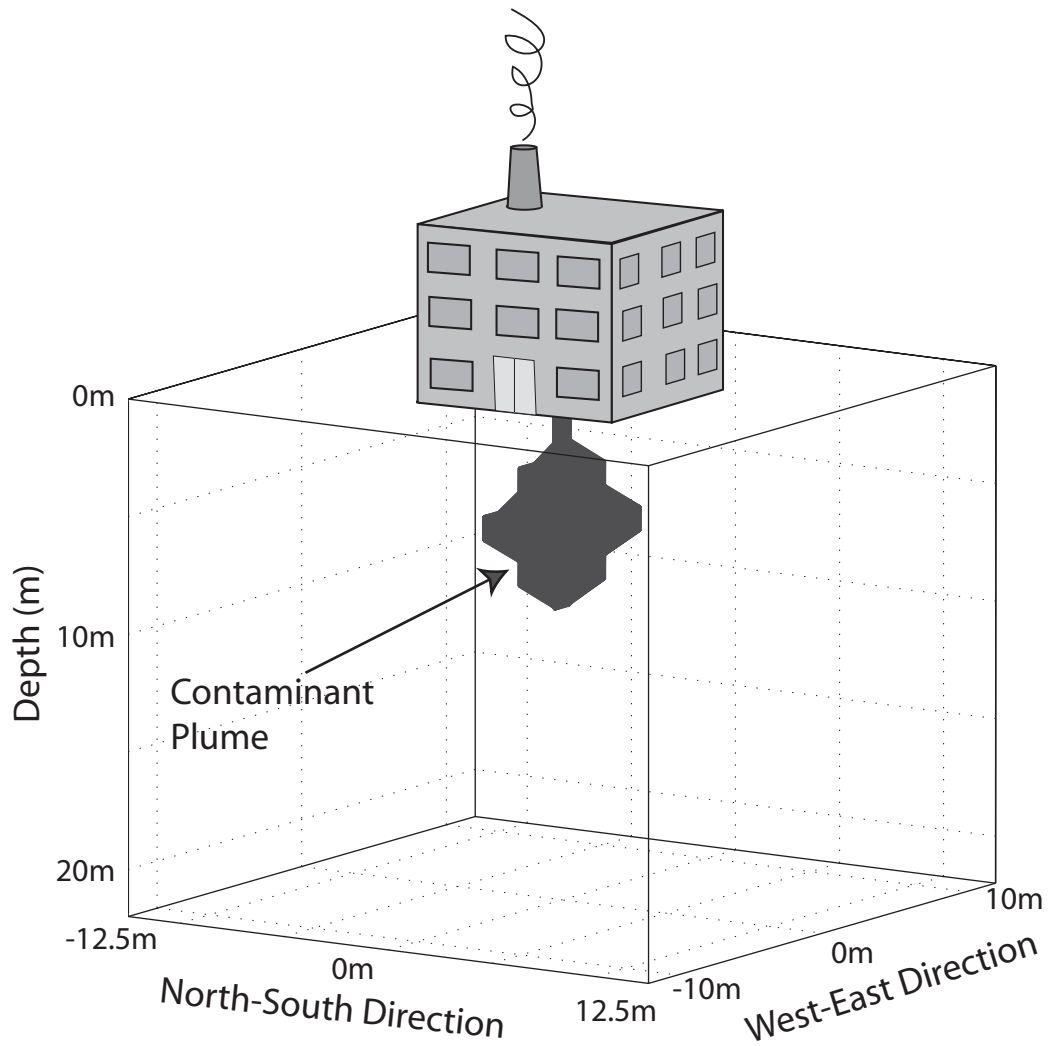


**Figure 4.11 Schematic of the synthetic problem. There is a suspected leak directly beneath the factory.**

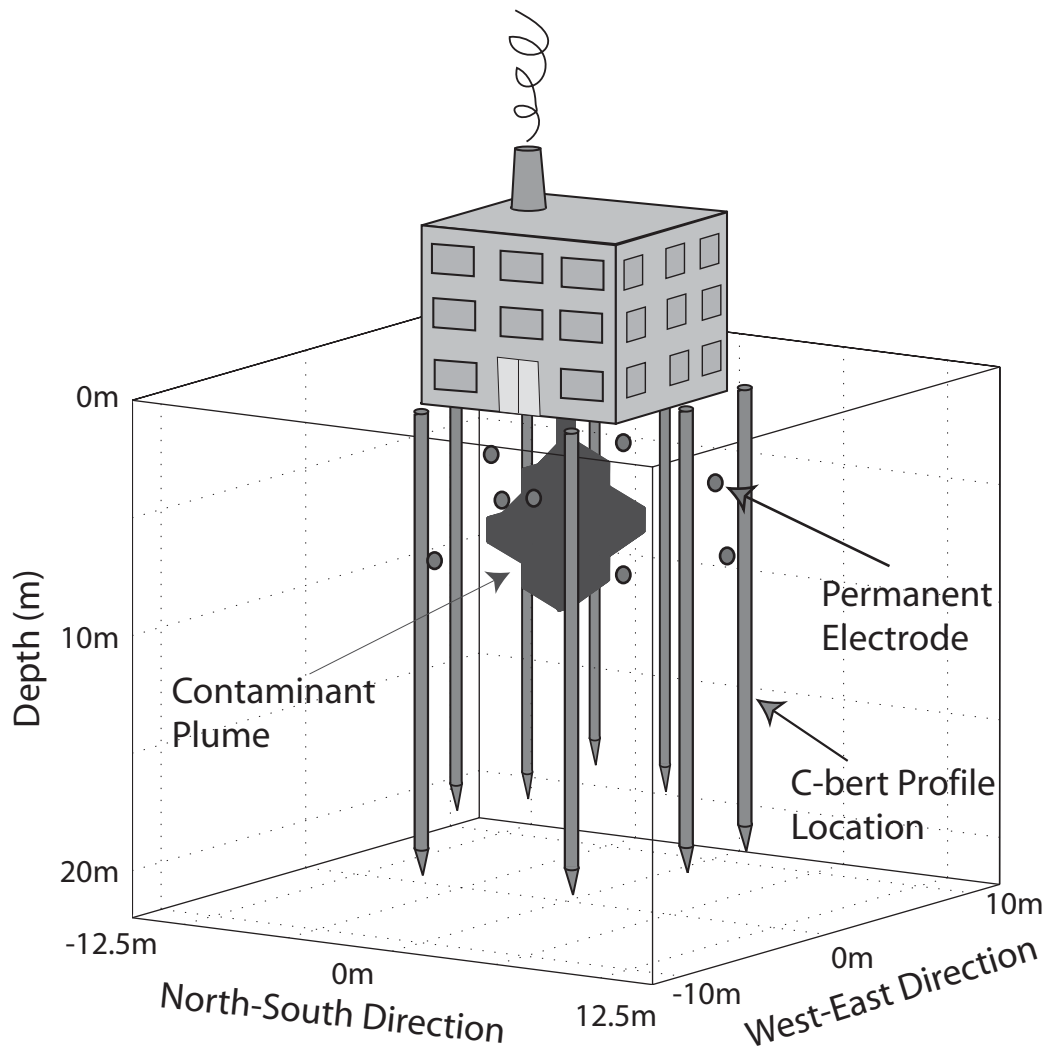


**Figure 4.12** Eight permanent electrodes are placed around the perimeter of the factor. Four are situated at depths of 4m and four are placed at 8m. Eight C-bert profiles are aquired around the perimeter, as indicated by the figure. C-bert profiles were aquired to a depth of 20m.

The model that was used for this experiment has a homogeneous 100 Ohm-m background resistivity which would correspond to a freshwater sandy aquifer. The contaminant saturated soil is modeled as a 5 Ohm-m material. These values yielded a resistivity contrast similar to that found at the Kidd2 site. The model space had 13200 cells; the contaminant occupied 116 cells. The position of the contaminant can be seen in Figure 4.11. In this experiment eight permanent current electrodes were pushed into the subsurface; Figure 4.12 illustrates the positions of the electrodes. Following the emplacement of these electrodes, we obtained a series of eight C-bert data sets around the perimeter of the building. The C-bert locations can be seen in Figure 4.12. 4704 synthetic data points, a total of 168 points for each of the 28 independent current pairs, were calculated using the forward modeling algorithm described above; these data were corrupted with 3%, uniformly distributed, random noise. Data were inverted using the Gauss-Newton algorithm, described earlier. As with the field experiment we used the RCPT logs to construct our starting model. However, as the cone never directly encounters the contaminant, the logs would suggest that the starting model for the inversion be a homogeneous 100 Ohm-m model. We used an isotropic flatness filter in the regularization.

Figure 4.13 illustrates the results of the inversion. As can be seen in the figure, we clearly identified the presence of the contaminant below the factory. This reconnaissance type of experiment highlights a major potential benefit of C-bert, that is real-time experimental design. All the RCPT data can be plotted in real time, so based on these data one can adapt the field sampling plan as more data come to light. Furthermore, as computational speed increases we will eventually be able to invert the C-bert data in the field, giving us 3-D information that can be used to guide and adapt our survey design. For this example, if it were found that the contaminant was migrating laterally, we could quickly adapt our sampling strategy, and acquire C-bert data sets that would allow us to image the migration. The results of a survey such as this may help to rapidly design a plan for clean-up at the site. In addition, these results could be used to guide the emplacement of a more expensive, permanent ERT array for long term monitoring.

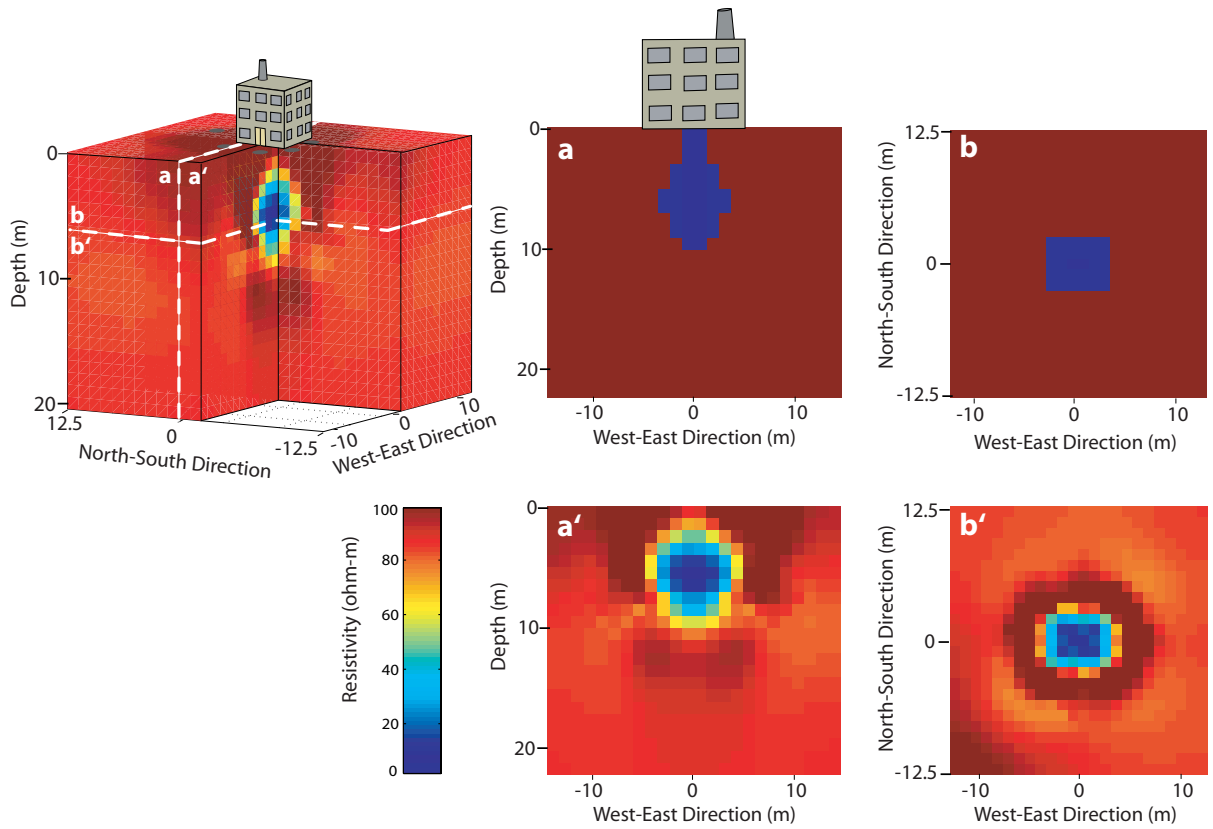


**Figure 4.13** Inversion results for the synthetic experiment. Frames a and a' are west-east slices through the synthetic model and the inverse result, respectively. Frames b and b' are depth slices, at 6m, through the synthetic model and the inverse results, respectively.

## 4.5 Summary and Conclusions

---

The focus of this work was an assessment of a cone-based imaging system for obtaining 3-D images of electrical conductivity. Cone-based imaging is advantageous for several reasons. First, it is a minimally invasive way to obtain information about the subsurface 3-D conductivity structure. Second, using a small number of source terms (e.g. for the Kidd2 study there were a total of only 36 current pairs), while measuring multiple data points, can potentially result in faster inversions. Third, we obtain multiple co-located data, which better constrains inverse results and assists in interpretation. Finally, field acquisition of C-bert data lends itself well to real time experimental design allowing one to choose new test locations as more information comes to light.

The Kidd2 field study has successfully demonstrated that C-bert data can be used to image the near subsurface. We have outlined the required field equipment and testing procedures necessary for acquiring these data. The equipment used for this survey required minor modifications of existing RCPT systems. Interpretation of the data, however, required the development of a cone-effect correction, which in turn required a computationally efficient solution to the forward problem. The iteratively determined boundary conditions approach, IDBC, was developed to facilitate this correction, by allowing us to solve the forward problem considerably faster than with a fully parameterized approach. The use of IDBC extends beyond simply solving for the cone effect; it can be used as an effective solver for the general Poisson's equation.

While in this pilot study we collected only five C-bert data sets, we could easily obtain tens of C-bert data sets in a full-scale field survey. The RCPT logs associated with each of these C-bert data sets are not only valuable for building an accurate starting model, but also give us the potential to generate more informed regularization operators for our inversions. In overparameterized inverse problems we must inject some a-priori knowledge in order to solve them. A-priori knowledge, based on in-situ, site specific measurements, is more desirable than derivative type filters, but in general these measurements are difficult to obtain. The co-located data that are acquired during the C-

bert process serves this purpose, as shown with our work, they can be used as constraints within our regularization operators.

We were very encouraged by the results of the field test at the Kidd2 site. We recognized, however, that the relatively simple, layered structure at the site did not allow us to fully demonstrate the potential benefits of C-bert. Our synthetic example illustrates the ability of C-bert to determine conductivity values in regions that are not readily accessible to other forms of measurement. We believe that, with further refinement, C-bert will become a useful tool for acquiring subsurface conductivity images.

# CHAPTER 5

## IMPROVED INTERPRETATION OF RESISTIVITY CONE PENETRATION LOGS

### Abstract

---

We develop a forward and inverse modeling routine for improved interpretation of resistivity logs acquired during resistivity cone penetration testing (RCPT). We use a series of forward models to study the sensitivity and resolution limitations of the RCPT module from the University of British Columbia. Using forward modeling we explore the effects of varying layer thickness and resistivity contrasts on the resulting RCPT logs. This analysis demonstrates that when thin conductive layers are present the spatial averaging of the resistivity log leads to overestimates of the true resistivity values. In addition, we investigate the 3-D sensitivity of the measurement by considering resistivity perturbations away from the cone. For the model we evaluated, we found the RCPT log to be sensitive to conductivity perturbations up to 20cm away from the cone. Our non-linear inversion algorithm allows the recovery of the true, layered resistivity structure from an RCPT resistivity log. The algorithm leads to accurate recovery of electrical resistivity at much higher spatial resolution than in the raw RCPT resistivity logs. Moreover, because the inversion incorporates information about the RCPT module electrode geometry, the results of the inversion are independent of module design and thus RCPT resistivity logs acquired using different tools can be compared using this technique. We demonstrate the utility of this approach using both synthetic and field data.

## 5.1. Introduction

---

Resistivity cone penetration testing (RCPT) is a relatively new in-situ testing technique that was developed by Campanella and Weemees in 1990. The technique involves attaching a resistivity module to a standard cone penetrometer so that measurements can be made of in-situ electrical resistivity. RCPT yields a high resolution resistivity log, along with the standard suite of cone penetration testing (CPT) data (eg. tip resistance, friction sleeve resistance and induced pore pressure). The tool was originally designed for assessing changes in ground water salinity (Campanella and Weemees, 1990). Since its development, however, this technique has been employed in other ways to obtain both qualitative and quantitative subsurface information.

Of specific interest in our research is the use of RCPT resistivity logs for two purposes: 1) to assist in acquiring a detailed 3-D image of the electrical conductivity structure of the subsurface and 2) to transform that electrical conductivity image to obtain information about subsurface properties, such as pore fluid resistivity, soil porosity, and degree of saturation.

Recent work in the Geophysical literature has highlighted the usefulness of resistivity logs, obtained during RCPT, to improve the electrical conductivity images obtained using electrical resistivity imaging. In particular, work has focused on the addition of RCPT logs as constraints in inversions of electrical resistivity imaging data. RCPT logs have been used to construct realistic starting models as well as constrain the depths of layers in DC-resistivity inversions. The addition of this information results in images that have better depth control and improved resolution (Catt, L.M. et al, 2005; Pidlisecky et al, 2006). In addition, RCPT has been shown to aid in the interpretation of geophysical images that were obtained without the use of RCPT logs as inversion constraints. For example Cardimona et al. (1998) used RCPT resistivity logs to help interpret seismic reflection and ground-penetrating radar data. Dahlin et al. (2004), used the RCPT resistivity logs for ground truthing resistivity values obtained from inversion of DC-resistivity data.

Material properties such as pore fluid resistivity, soil porosity, and degree of saturation can potentially be obtained from RCPT logs by using laboratory derived relationships between electrical resistivity and the material property of interest ( Archie, 1942; Waxman and Smits, 1968; Glover et al, 2000). However, using these relationships to obtain accurate estimates of material properties can be challenging, especially when the measurement scale and geometry of the field experiment differ from the laboratory experiment. Because obtaining accurate estimates of properties is challenging, Daniel et al (2003) explored the usefulness of obtaining relative changes in material properties from RCPT resistivity logs. In particular, they showed that by using pre- and post-compaction RCPT resistivity logs, one can infer the relative change in soil porosity. In addition, they show data that indicates there is promise for obtaining the relative change in saturation using RCPT.

There remain, however, significant challenges to using RCPT resistivity logs for aiding in the interpretation of geophysical images and obtaining 1-D estimates of material properties. In particular, we cite two major issues that need to be addressed.

First, when trying to incorporate resistivity logs with a geophysical data set or interpret RCPT resistivity logs using lab scale relationships, it is critical that one understands the averaging effect of RCPT. Given that the RCPT measurements are made using an electric field, i.e. a diffusive field, the measurement volume is a function of the in-situ conductivity structure and the resistivity tool geometry. “Tool geometry” means the relative position, shape and size of the measurement electrodes. These dependencies mean that the measured RCPT log is really a non-linear average of the subsurface conductivity structure near the cone.

When using RCPT resistivity logs in conjunction with other geophysical data, we are usually required to upscale the resistivity logs. However, to accurately perform this transformation we must understand the averaging that has occurred in the resistivity log. Furthermore, in cases where anisotropy may be present (e.g. interbedded silts and sands), knowing the scale of averaging can help to ascertain whether or not the resistivity log will be sensitive enough to detect the fine layers (i.e. to detect the anisotropy). With respect to the use of empirical relationships, the averaging that occurs during

measurement means that directly applying laboratory scale relationships (e.g. Archie's law) to RCPT logs can lead to erroneous estimates of material properties.

The second that needs to be addressed in order to improve the utility of these data is that, the RCPT resistivity module, unlike the standard cone, has no standardized design for the resistivity module. This makes it particularly challenging to quantitatively compare data that have been acquired using different resistivity modules. Because of this, we are precluded from building a database of RCPT logs that can be used to build correlations with other measured parameters, e.g. tip resistance. The standards that are associated with CPT, have allowed the scientific and engineering communities to develop meaningful correlations between parameters, this in turn has greatly improved the utility of CPT. Removing the effect of tool geometry from RCPT logs would allow for a similar database to be established for RCPT logs, and thus increase the utility of these data.

In this paper we present a numerical modeling technique that allows us to model the RCPT log, and thus understand the averaging that takes place. We demonstrate that, in layered media, the resistivity data acquired using the RCPT module can be markedly different the true in-situ resistivity values. We consider specifically the design of the RCPT module from the University of British Columbia, (UBC), and demonstrate a methodology by which we can obtain bounds on the resolution of the tool. In addition, we also present a novel inversion routine that allows us to, for a given RCPT log, undo the averaging of the RCPT and recover the true resistivity structure. This inversion technique can be used for any tool geometry. Moreover, the resulting inverted model is independent of tool geometry. We apply the technique to both synthetic and field data.

## 5.2. RCPT

---

The resistivity module considered in our study is the one described by Campanella and Weemees, (1990). The module, as seen in Figure 1, is coupled to a standard cone penetrometer; both the module and the cone were designed and built in the Department of Civil engineering at UBC. The module is 36.6mm in diameter, which is slightly larger than the diameter of the standard cone to ensure good soil-electrode coupling. It contains four brass ring electrodes, arranged as two electrode pairs, one pair separated by  $\sim 10$  mm, the other by  $\sim 150$  mm. For this work, we only consider the electrode pair separated by 150 mm to make the resistivity measurements. We have done this for two reasons. First, because of the larger separation and larger contact area (the outer electrodes are slightly wider), the outer electrodes yield a better signal/noise ratio and better repeatability. Second, with the wider spacing, the signal penetrates deeper into the soil. This is an advantage as it can reduce the sensitivity of the tool to the disturbed ground immediately adjacent to the cone. A drawback commonly noted about the wider electrode separation is that it samples a larger soil volume. This means the resulting measurement has lower resolution. However, using the inversion technique that will be presented in a following section we demonstrate that, even for the 150mm spacing, it is possible to recover accurate resistivity values with a vertical resolution equal to that of the spatial sampling interval (e.g. 2.5 cm).

During RCPT soundings discussed herein, resistivity measurements are made every 2.5cm. These measurements are made using a high frequency ( $\sim 1000$  Hz) AC current injected into one pair of electrodes. Voltage is measured across the same pair of electrodes (Lunne et al., 1997). This measurement yields a resistance value, which is a function of in-situ conductivity and tool geometry. In order to obtain the resistivity which is a material property, we scale the resistance by a geometric factor.

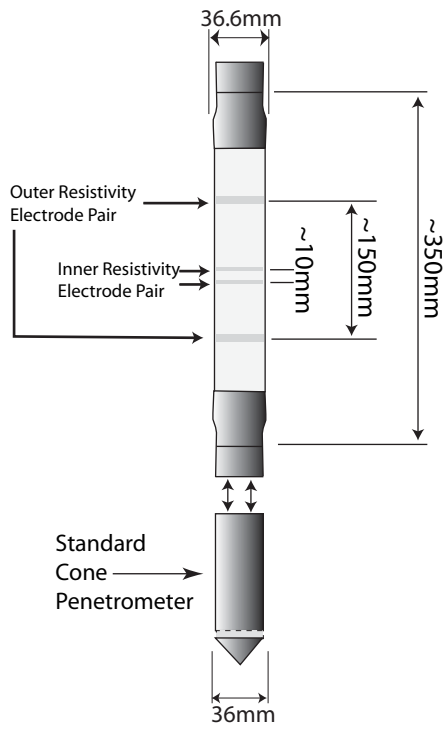


**Figure 5.1 UBC RCPT cone.**

For the field data described here, acquired with the UBC module, the geometric factor was obtained through a laboratory calibration (Campanella and Weemees, 1990). The resistivity cone was immersed in a 2 m x 2 m x 1.5 m water tank. Sodium chloride (NaCl) was added to the tank, the resistivity of the water is measured with a conductivity probe, and the voltage measured across the cone electrodes. This procedure was repeated ~20 times for different concentrations of NaCl. A linear relationship found between the cone voltage measurements and the probe-measured resistivity of the water was used to define the geometric factor needed to obtain resistivity values from the resistance measurements. For the synthetic models that are evaluated in this paper, an analogous numerical experiment was performed to obtain the geometric factor.

## 5.3. Modeling and Inversion

---

### 5.3.1. Forward Modeling

Here we present an algorithm for modeling the observed resistivity log obtain during RCPT, for a given conductivity structure. The algorithm can be used to model any RCPT module, given we know the electrode geometry of the tool. RCPT involves injecting current through a pair of electrodes and measuring the potential field at the same electrodes. When the current is injected, the surrounding 3-D conductivity structure determines the potential that will be measured for a given input current. The partial differential equation that describes this is:

$$-\nabla \cdot \sigma(x, y, z) \nabla \phi(x, y, z) = I(\delta(\mathbf{r} - \mathbf{r}_+) - \delta(\mathbf{r} - \mathbf{r}_-)). \quad (5.1)$$

where  $\phi$  is the potential field;  $I$  is the input current, from a dipole; and  $\sigma$  is the conductivity structure of the medium. Here,  $\mathbf{r}_+$  and  $\mathbf{r}_-$  are the locations of the positive and negative current sources, respectively, and  $\delta(\mathbf{r} - \mathbf{r}_+)$  is the dirac delta function, centered at the current source location.

In order to model RCPT resistivity logs, we solve equation 5.1 on a grid, discretized so as to capture the scale of interest. For modeling the resistivity logs, this requires that the model space has cells on the order of centimeters in the region immediately surrounding the cone. Rewriting equation 5.1 in matrix form we have:

$$(\mathbf{D} \cdot \mathbf{S}(m) \cdot \mathbf{G}) \mathbf{u} = \mathbf{A}(m) \mathbf{u} = \mathbf{q}. \quad (5.2)$$

Here,  $\mathbf{D}$  and  $\mathbf{G}$  are matrices representing 3-D, variable grid, second-order finite-difference divergence and gradient operators, respectively. The difference operators are applied across the entire model space, including the boundary cells. This enforces no-flux boundary conditions at the edges of the model space.  $\mathbf{S}$  is a diagonal matrix that contains the harmonic average of the conductivity of each cell face along the main diagonal.  $\mathbf{u}$  and  $\mathbf{q}$  are potential and source vectors respectively, defined at the centers of the cells. The source vector,  $\mathbf{q}$ , is an approximation to the delta function in the right hand side of equation 5.1. As such,  $\mathbf{q}$  is a vector of zeros with a value of  $\frac{1}{\Delta V}$  at the positive source

location and a value of  $-\frac{1}{\Delta V}$  at the negative source location, where  $\Delta V$  is the volume of the cell.

From equation 5.2 we see that in order to predict the potential field, we need to solve for  $\mathbf{u}$ , as shown in equation 5.3:

$$\mathbf{u} = \mathbf{A}(m)^{-1}\mathbf{q}. \quad (5.3)$$

In equation 5.3 we obtain the potential field at all points in our model space. However, the RCPT log is a small sub-set of these points. In order to obtain our RCPT log, we define a projection matrix,  $\mathbf{Q}$ , that selects the RCPT data points from  $\mathbf{u}$ . This results in the following equation for calculating our measure data, i.e. the RCPT log:

$$\mathbf{d} = \mathbf{Q}\mathbf{u} = \mathbf{Q}\mathbf{A}(\sigma)^{-1}\mathbf{q}. \quad (5.4)$$

where  $\mathbf{d}$  is the potential measured by the RCPT logging tool. In order to transform these data into resistivity values, we scale  $\mathbf{d}$  by the geometric factor.

As mentioned earlier, the resistivity module is calibrated in a tank of water with known conductivity. When numerically modelling the RCPT resistivity logs, we perform the tank experiment numerically. Using equation 5.4 we model the RCPT resistivity log at the center of a homogeneous conductivity structure (i.e. the tank). Given this datum, we can then define the geometric factor as follows:

$$K = \frac{1}{\sigma \cdot d_{center}} \quad (5.5)$$

Given  $K$ , we can then define our modeled RCPT log as follows:

$$\mathbf{R}_{log} = K \cdot \mathbf{d} \quad (5.6)$$

where  $\mathbf{R}_{log}$  is our modeled log. The above technique allows for the modeling of the RCPT log for any conductivity model. Furthermore, the technique can be used to model the response and sensitivity of different logging tool designs.

We note that the operator described in equation 5.3 is defined in 3-D. However, there are some computational challenges with modeling RCPT resistivity logs in 3-D.

First, as the cone is small, we must discretize quite finely around the cone, so as to accurately model current flow. This can result in  $\mathbf{A}$  becoming large. Second, as the cone is pushed through the subsurface, at each new acquisition location (e.g. every 2.5cm) we have a new  $\mathbf{q}$  term so must solve equation 5.3 many times. These two factors make it computationally prohibitive to explicitly model the RCPT resistivity logs in 3-D. Thus we have opted to solve the problem using a 2.5-D approximation. With the 2.5-D solution we assume  $\frac{d}{dy}\sigma(x, y, z) = 0$ , i.e the conductivity structure does not vary in the y-direction.

This reduces the model space to a 2-D plane. However, the approximation still considers current flow in 3-D. Solving the 2.5-D problem is much more efficient than solving the full 3-D formulation. Details of the 2.5-D algorithm, and the specific implementation used for this work can be found in Pidlisecky and Knight (2006).

The above model approach allows us to model the RCPT logs, for any 2-D conductivity structure, for any RCPT logging tool. All that is required is the electrode geometry and sampling interval of the tool.

### 5.3.2. Inversion

As can be seen in equation 5.1 the measured potential field is a non-linear function of the conductivity structure near the cone. Because of this the resistivity log represents a non-linear average of the resistivity structure near the measurement location. Furthermore, the averaging is also a function of the tool geometry. Ideally we would like to remove the effect of this averaging, so as to get an accurate estimate of electrical conductivity that is independent of tool geometry. In this section we develop a non-linear inversion technique that allows us to recover the layered resistivity structure that gives rise to our measured RCPT log.

In order to determine the resistivity structure captured in our observed RCPT log, we seek the layered resistivity model that minimizes the misfit between our observed log and our modeled log. Framing this as our objective, we seek to minimize the following objective function:

$$\Phi(\mathbf{m}) = \left\| (K\mathbf{Q}\mathbf{A}(\mathbf{m})^{-1}\mathbf{q} - \mathbf{R}_{\text{obs}}) \right\|^2 = \left\| (\mathbf{R}_{\text{calc}} - \mathbf{R}_{\text{obs}}) \right\|^2 \quad (5.7)$$

where  $\mathbf{m}$  is our layered model at a given iteration, with the model parameters defined as  $m = \ln(\sigma)$ ;  $\mathbf{R}_{\text{obs}}$  is a vector containing the observed RCPT log;  $\mathbf{R}_{\text{calc}}$  is a vector containing the calculated RCPT log for  $\mathbf{m}$ ; and  $\| \cdot \|^2$  is the least-squares norm. To solve equation 5.7 we expand the first term under the norm about a given model,  $\mathbf{m}_i$ , to yield:

$$\Phi(\mathbf{m}_{i+1}) = \left\| \left( \mathbf{R}(\mathbf{m}_i)_{\text{calc}} + \frac{\partial \mathbf{R}}{\partial \mathbf{m}} \delta \mathbf{m} \right) - \mathbf{R}_{\text{obs}} \right\|^2 \quad (5.8)$$

In order to find the minimum of equation 5.8, we take the derivative with respect to  $\mathbf{m}$  and set the resulting function to zero, yielding the Gauss-Newton model update:

$$\delta \mathbf{m} = - \underbrace{(\mathbf{J}^T \mathbf{J})^{-1}}_{\mathbf{H}^{-1}} \underbrace{(\mathbf{J}^T (\mathbf{R}_{\text{calc}} - \mathbf{R}_{\text{obs}}))}_{\mathbf{g}} \quad (5.9)$$

where  $\mathbf{J}$  is the Jacobian or sensitivity matrix,  $\left( \frac{\partial \mathbf{R}}{\partial \mathbf{m}} \right)$ . The matrix  $\mathbf{H}$  is an approximation to the Hessian and  $\mathbf{g}$  is the gradient of our objective function. We note that using  $\mathbf{m} = \ln(\sigma)$  enforces a positivity constraint on the inverted conductivity structure.

With equation 5.9 we can predict a model update,  $\delta \mathbf{m}$ , that minimizes the value of our objective function in equation 5.7. Theoretically, equation 5.9 can be solved only if the number of model parameters is less than or equal to the number of measured data. Ideally, we would like to predict one model parameter for each datum. This leads to an equally determined problem in theory. In practice, however, the matrix  $\mathbf{H}$  is ill-conditioned, and thus the inverse of  $\mathbf{H}$  will be unstable and equation 5.9 will yield a very noisy model update (Per-Christian Hansen, 1998). The ill-conditioned nature of these types of problems can be overcome by adding a-priori knowledge about the solution. The way this is most commonly done is by adding a component of model regularization to the objective function in equation 5.7. However, traditional regularization techniques, such as those presented by Tikhonov and Arsenin (1977), result in smoothed models that tend to incorrectly predict conductivity values. Because we are interested in recovering sharp

boundaries (i.e. layers) in our model and we want to recover the true resistivity values (at the scale of our sampling interval), we take a different approach to model regularization.

In order to regularize our solution, we reduce the model space by a small number of parameters, so that part of  $\mathbf{H}$  represents an overdetermined system. In practice, this means that we recover fewer model parameters than number of data so there is a loss of resolution in part of our model space. For any given log, however, we are free to choose in which part of the model space we are willing to give up resolution. In many situations where we use RCPT, the top ½ meter of soil is not the region of interest, so sacrificing resolution in this region might be the logical choice. Alternatively, if there is a depth interval where a resistivity log shows little variation, it might be reasonable to approximate this region as a single, homogeneous, layer.

In addition to stabilizing the inverse solution by reducing the size of the model space, we also solve equation 5.9 using a truncated singular value decomposition (SVD) (Per-Christian Hansen, 1998). Solving equation 9 using truncated SVD helps to further reduce numerical noise present in  $\mathbf{H}^{-1}$  and is useful for stabilizing the solution when there is significant noise in the data.

Given that equation 5.9 is a linearization of the non-linear problem about a model iterate,  $\mathbf{m}_i$ , we must solve equation 5.9 for many iterations to find the model that best fits the data. At each iteration we define a new model as follows:

$$\mathbf{m}_{i+1} = \mathbf{m}_i + \alpha \delta \mathbf{m} \quad (5.10)$$

where  $\mathbf{m}_{i+1}$  is the new model, and  $\alpha$  is a line search parameter. We use a line search to ensure that the model update sufficiently decreases the value of the objective function in equation 5.7. The sufficient decrease criterion is defined by the Armijo inequality:

$$\Phi(\mathbf{m}_{i+1}) = \Phi(\mathbf{m}_i + \alpha \delta \mathbf{m}) \leq \Phi(\mathbf{m}_i) + c_1 \alpha \cdot \mathbf{g}(\mathbf{m}_i)^T \delta \mathbf{m} \quad (5.11)$$

where  $c_1$  is a constant, which in practice takes a very small value (e.g.  $10^{-4}$ ) and  $\Phi$  is the value of the objective function.  $\alpha$  in equation 5.10 is initially taken as unity, then the inequality in equation 5.11 evaluated. If equation 5.11 is not satisfied,  $\alpha$  is reduced, and the process repeated until either equation 5.11 is satisfied, or a predetermined number of linesearch iterations is exceeded. Once a suitable  $\alpha$  has been determined, equation 5.8 is

linearized about the new solution, and a new iterate determined. This process is repeated until the objective function in equation 5.7 has been minimized to a desired tolerance. For the examples presented here, the inversion required between 6 and 10 iterations to reach convergence.

## 5.4. Synthetic Examples

---

In this section, we use three synthetic examples to evaluate the correspondence between three different subsurface conductivity structures and what is captured in the RCPT resistivity logs. The three examples represent thin layers of low-resistivity silt or clay in a resistive sand background. The analysis for sandy layers in a clay background produced similar results. Figure 5.2 is a one meter depth section of the grid on which our computations were performed. The smallest cells, located along the centerline, are 2.5cm x 2.5cm. The total width of the model space was 8m, which was sufficient to eliminate boundary effects. The cone was modeled along the centerline of the grid, starting at the top of the grid. The cone was moved vertically down through the model space, with data being calculated every 2.5cm.

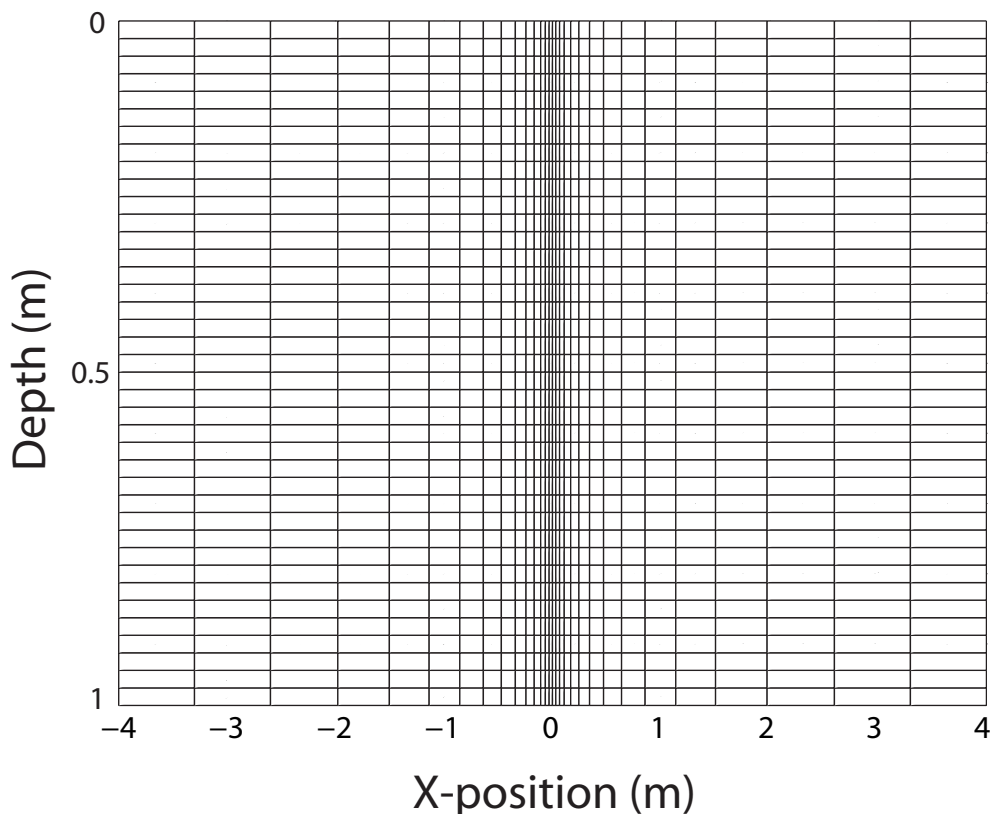


Figure 5.2 The forward and inversion grid. The cone is modeled at the center of the grid.

### ***5.4.1. Layers of Varying Thickness***

The first resistivity structure we explored can be seen in Figure 5.3a. The background sand was assigned a resistivity of 100 Ohm-m. The six clay layers, with resistivity of 1 Ohm-m, increased in thickness from 5cm at the top of the model to 27.5 cm at the bottom. Figure 5.3b is the 1-D profile taken down the center line of Figure 5.3a. This log represents what we would measure if our resistivity module had perfect resolution (i.e. no averaging).

In Figure 5.3c, we see the modeled resistivity log, obtained using the forward model approach described earlier. We note three ways in which the log in Figure 5.3c is observed to vary from the 1-D profile. First, in Figure 5.3c, the clay layers located at 2m and 4m deep have two distinct peaks for each layer. These layers have thickness less than electrode separation. Each peak is associated with the point when one of the measurement electrodes passes through the center of the layer, thus we see two peaks. Second, we substantially overestimate the resistivity of the first three clay layers. The overestimate is due to the fact the log has vertical sensitivity beyond the electrodes, and is thus averaging over a length scale that is larger than the thickness of the clay layer. Thus, the measurement is being influenced by the resistive sand unit. Third, for all of the layers the log overestimates the thickness of the layers. For example, the 10cm thick layer appears to be roughly 25cm in the log. As with the previous point, the vertical averaging causes the tool to sense the layer before it has reached the layer.

From this example we see that if we desire to quantitatively interpret the RCPT logs, if the resistivity contrast is 1:100, the layer thickness must be greater than the electrode separation before we will measure the true conductivity value of the layer. However, even when the layer is this thick we will only correctly estimate the resistivity at the center of the layer. This example suggests that for thin clay layers, we can drastically overestimate in-situ resistivity. Another general feature to take from the modeled log is that the log represents a smoothed version of the true model.

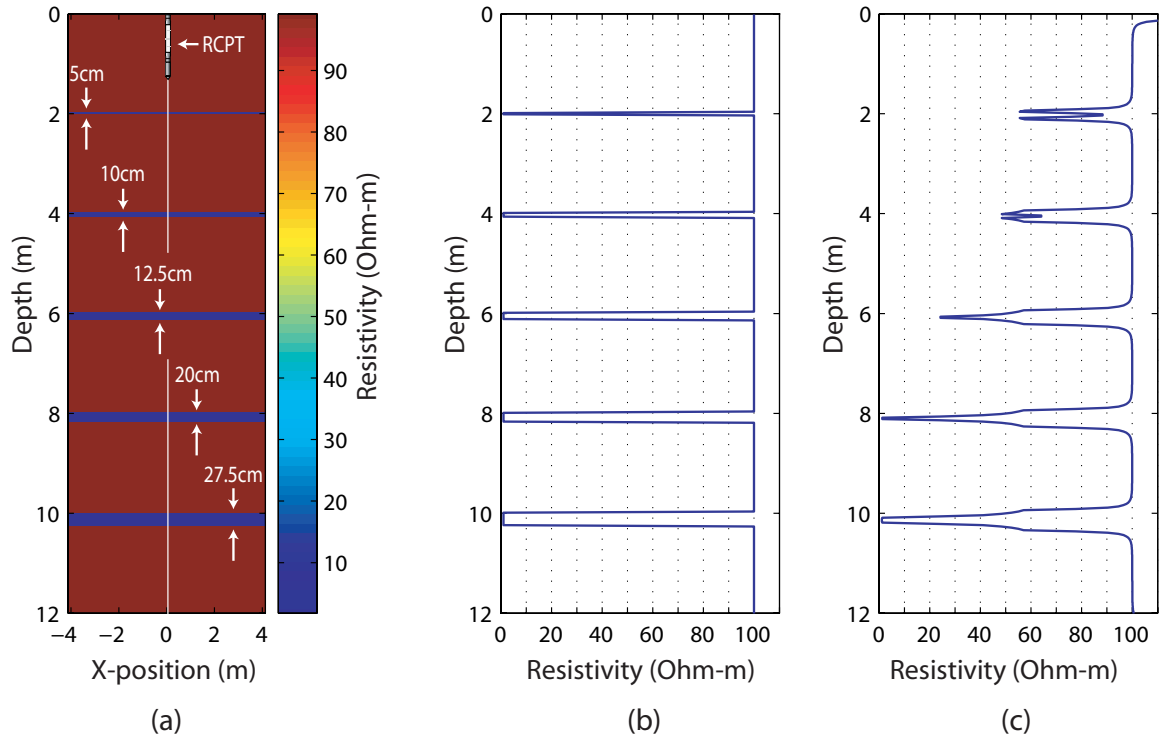


**Figure 5.3 Forward modeling results for clay layers of varied thickness. (a) the 2.5D resistivity structure used for the forward modeling. (b) 1-D resistivity profile. (c) modeled RCPT resistivity log.**

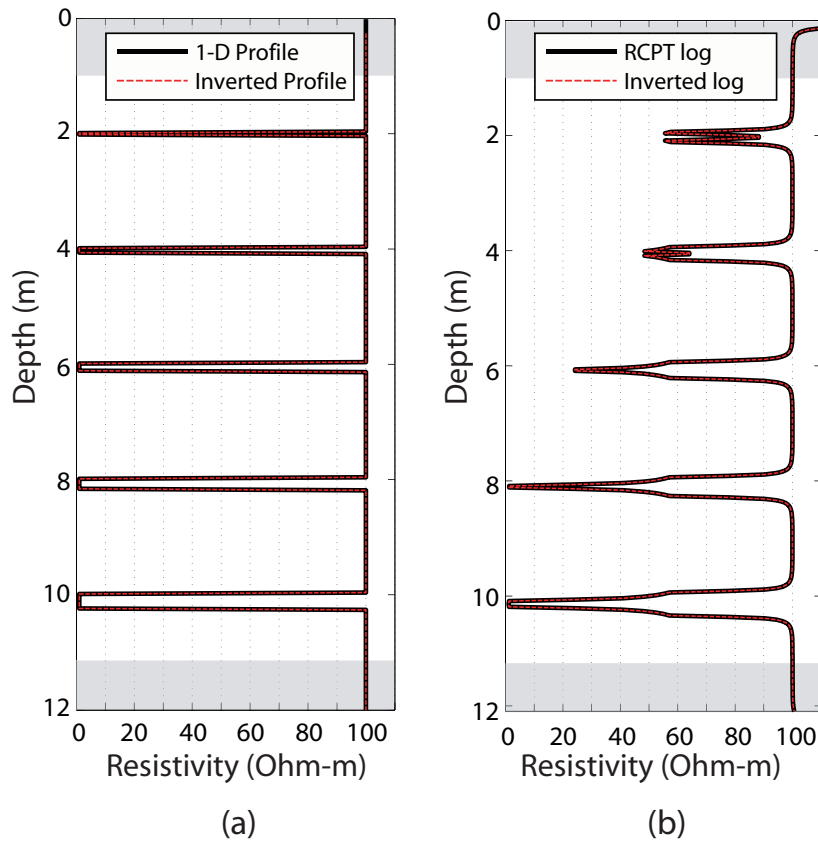


**Figure 5.4** Inversion results for the model in Figure 5.3. (a) the 1-D resistivity profile and the inverted profile. (c) the modeled RCPT log and the inverted log.

Starting with the modeled RCPT resistivity log in Figure 5.3c, we used our inversion algorithm described above to see if it were possible to recover the 1-D resistivity profile shown in Figure 5.3b. Figure 5.4 is the result of the inversion. The shaded regions at the top and bottom of Figures 5.4a and 5.4b are the regions, that for the purpose of the inversion, were modeled as one cell. The rest of the model was discretized at 2.5cm. Figure 5.4a shows the 1-D resistivity profile, from Figure 5.3b, along with our inverted profile. From this image it is clear that the models are almost a perfect match. Figure 5.4b shows the RCPT log, from Figure 5.3c, plotted with the log we obtain through the inversion routine. As with the 1-D profiles, the logs match nearly perfectly. We note that no noise was added to this inversion. In practice RCPT data can be acquired with a very high signal to noise ratio. With a high signal to noise ratio in the data, the numerical noise in the inversion becomes the dominant factor, and thus we can largely

ignore data noise. However, if the data do contain significant noise, we can handle the noise by varying the truncation threshold of the SVD solution.

#### ***5.4.2. Layers of Varying Resistivity***

The next resistivity structure is shown in Figure 5.5a. Again, the background sand has a resistivity of 100 Ohm-m. But in this example, the silt/clay layers have a consistent thickness of 15cm and a resistivity of 90 Ohm-m in the top layer decreasing to 10 Ohm-m in the bottom layer. Each successive layer decreases in resistivity by 20 Ohm-m. Figure 5.5b is the 1-D profile taken down the center line of Figure 5.5a.

Figure 5c is the modeled RCPT resistivity log for the resistivity structure in Figure 5.5a. There are two key points to observe when comparing Figures 5.5b and 5.5c. First, the modeled RCPT resistivity log is a fairly good representation of the 1-D resistivity profile shown in Figure 5.5b. As with the previous example the RCPT log overestimates the resistivity values, however, in this case the overestimate is only on the order of 10%. Second, we once again overestimated the width of the layer, once again due to vertical averaging. In general, however, for this case where the resistivity contrast between the background and the layers was small, the log is fairly good representation of the 1-D resistivity profile.

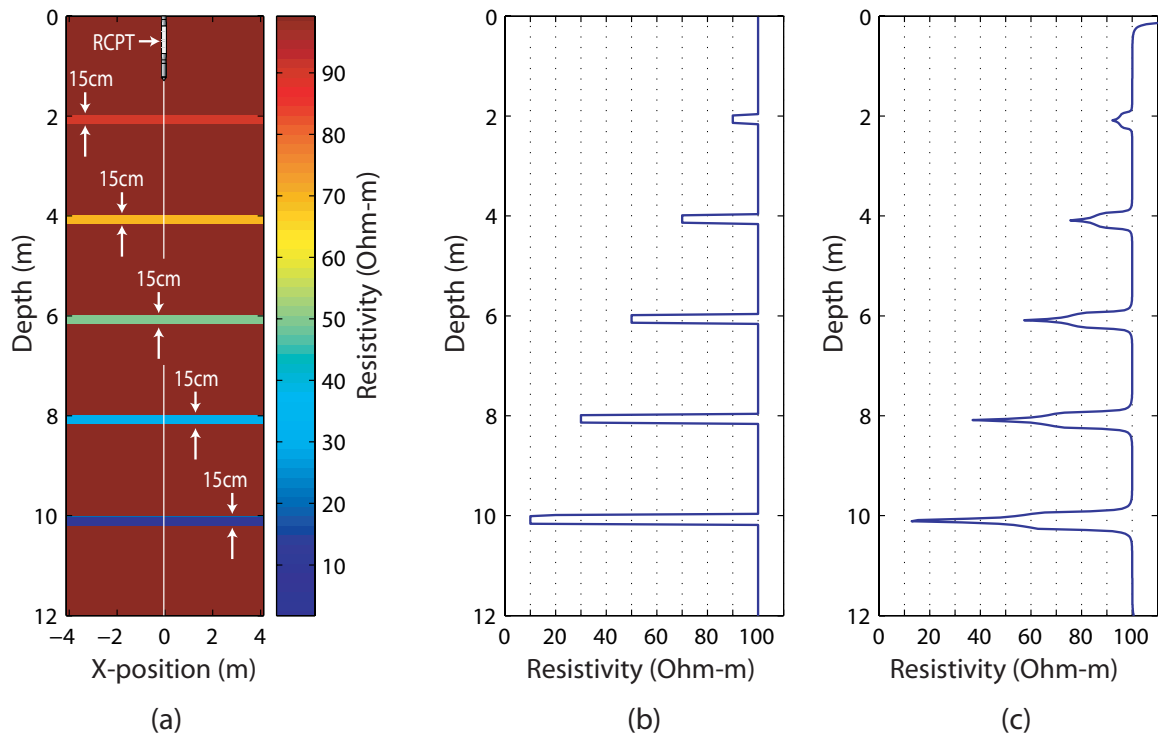


**Figure 5.5 Forward modeling results for layers with varied conductivity. (a) the 2.5D resistivity structure used for the forward modeling. (b) the 1-D resistivity profile. (c) modeled RCPT resistivity log.**

Figure 5.6 shows the results of using our inversion algorithm to recover a resistivity profile from the modeled RCPT resistivity log seen in Figure 5.5c. Figure 5.6 presents the results of the inversion. As with the previous example the shaded portions of these models are modeled as one cell. In Figure 5.6a we see the true profile plotted with the inverted profile; we obtain a near perfect match. The inverted RCPT log and the true RCPT log, from Figure 5.5c, also exhibit excellent agreement. The two inversion examples presented thus far have shown near perfect recovery of the true model. We note however, these inversions represent the best case scenarios. We have no noise and are inverting on the same grid that was used for the forward model. In addition, it is important to note that, despite the fact the RCPT logs were modeled using the 2.5D approximation, the layered systems can be well approximated with a 1-D profile (e.g. the inverted profile).

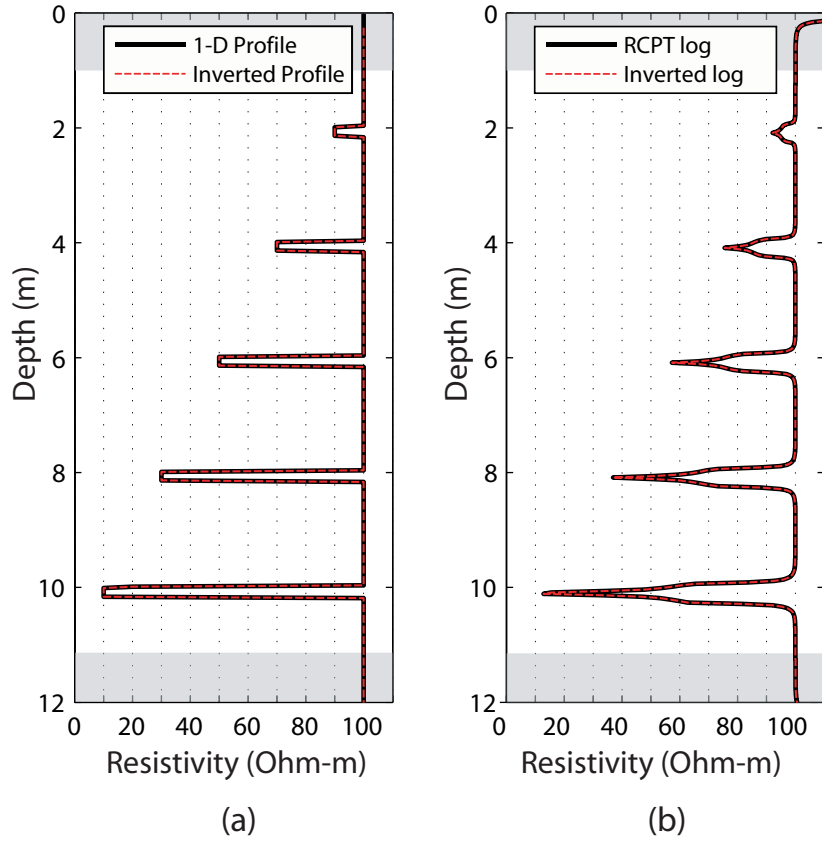
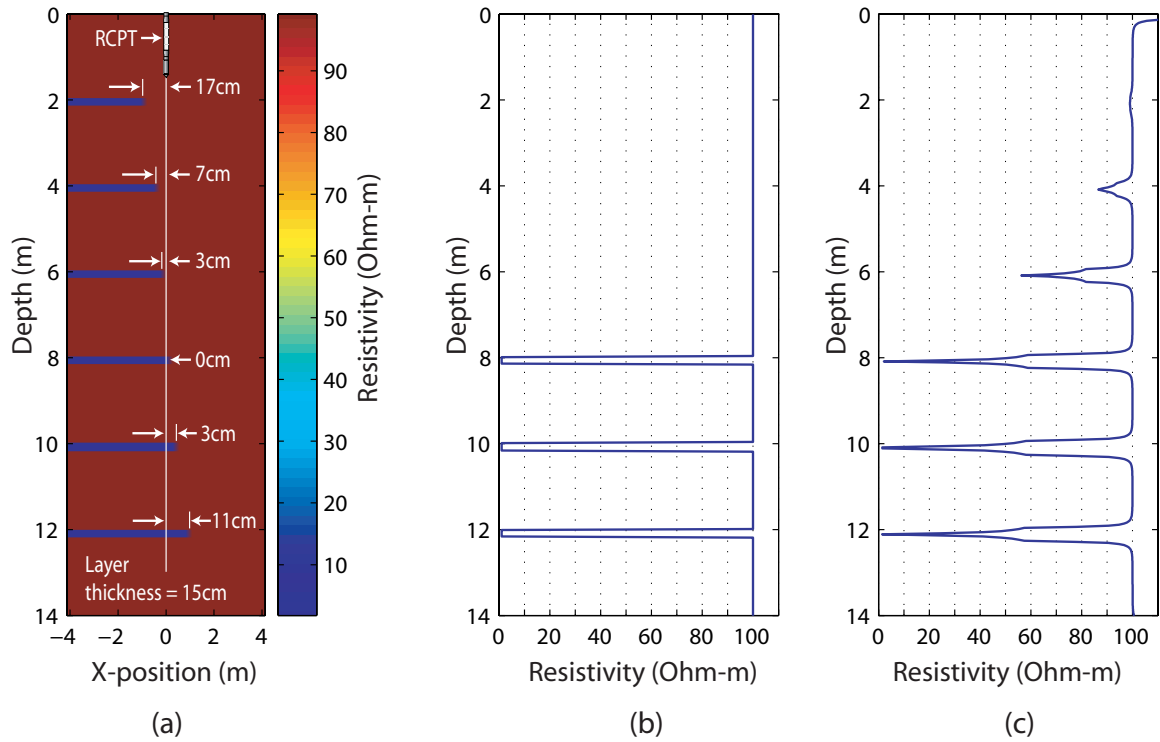


Figure 5.6 Inversion results for the model in Figure 5.5. (a) the 1-D resistivity profile and the inverted profile. (c) the RCPT log and the inverted log.

### ***5.4.3. Truncated layers and 3-D effects***

In order to establish the sensitivity of the RCPT resistivity log to resistivity perturbations slightly away from the cone, we ran a series of numerical experiments that involved moving a clay layer closer to the cone. Figure 5.7a depicts the resistivity structure under consideration. As before, the background sand has a resistivity of 100 Ohm-m. However, in this example, the clay layers have fixed thickness and resistivity of 15cm and 1 Ohm-m, respectively. The layer edge at the top of the structure is 17cm away from the cone location. The layer is progressively moved from left to right, until it overlaps the cone location by 11cm, at the bottom of the structure.

Figure 5.7b is the 1-D profile. As can be seen in the profile, the RCPT module does not encounter the clay layer until a depth of 8m. The modeled resistivity log is seen in Figure 5.7c. There is a key difference between this modeled resistivity log and the 1-D resistivity profile, shown in Figure 5.7b. The difference is that the modeled log shows sensitivity to the truncated layers that are away from the logging location. In particular, the modeled resistivity log shows large peaks at 4m and 6m. The presence of these peaks is evidence that the RCPT resistivity log is averaging in 3-D, and that there is measurable sensitivity to perturbations away from the cone.



**Figure 5.7 Forward modeling results for truncated clay layers. (a) the 2.5-D resistivity structure used for the forward modeling. (b) the 1-D resistivity profile. (c) modeled RCPT resistivity log.**

As with the previous examples we inverted data from the modeled RCPT resistivity log to recover the 1-D resistivity profile. However, when attempting to invert these data, we found the inversions to be very noisy. The noise was due to the fact that the RCPT logs were created using a 2-D conductivity structure, however, the inversion is done assuming that the earth is a layered model. This leads to an inconsistency between our forward modeling physics and our inversion physics, which in turn leads to a noisy inversion. In order to reduce the noise in the inversion we discretized the model using a different approach from the previous two models. We identified regions of the RCPT log in Figure 5.7c that did not vary and discretized these regions with 25cm cells. These regions are identified by the shaded regions in Figure 5.8. The white regions in Figure 5.8 were discretized at 2.5cm. This discretization substantially reduced the noise in the inverted models.

The inverted model in Figure 5.8a has two key features. First, the routine tries to fit layers at 4m and 8m. However, because the RCPT log actually contains 3-D information and the inverted model is 1-D, the inverted profiles are noisy in these regions. When forcing the inversion to solve for a layered model when the true earth is locally 2D or 3D, we will not be able to accurately match the data. We note that, for the case of the UBC RCPT module, locally can mean  $< 20\text{cm}$  away from the cone.

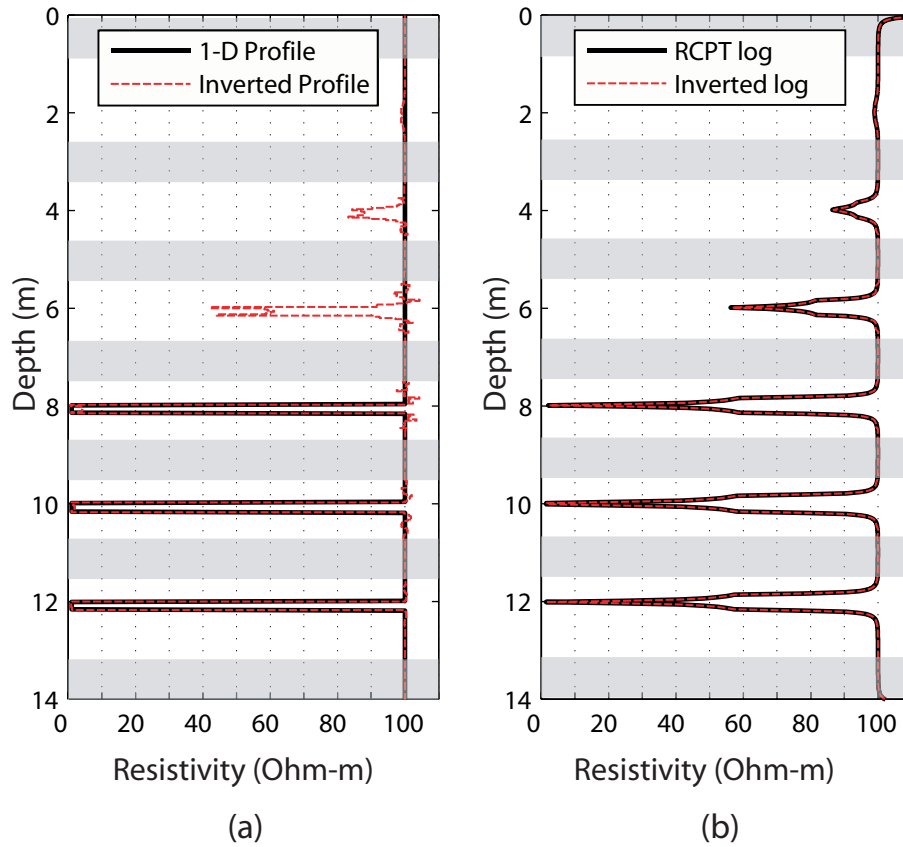


Figure 5.8 Inversion results for the model in Figure 5.7. (a) the 1-D resistivity profile and the inverted profile. (c) the RCPT log and the inverted log.

## 5.5. Field data

To further evaluate the merits of our inversion technique for interpreting RCPT resistivity logs, we applied the technique to field data that were acquired at the Kidd2 research site in Richmond, British Columbia. RCPT was performed in the top 12 m of the site. Standard CPT measurements were made from the surface to 12m. The resistivity log was acquired in the saturated zone, from a depth of 2m to 12m. Figure 5.9 presents the results of the RCPT. The soil behavior type (SBT) was determined using the interpretation scheme of Robertson, (1990). The SBT uses the measured tip resistance and friction ratio to generate a lithology profile. The profile was generated at a discretization of 2.5cm, however, large sections of the log result in the same SBT and thus the resulting SBT profile has 40 distinct units, with thickness varying from 2.5cm to 1.5m. The region of interest, from 2m to 12m, is comprised of sands, interbedded with silty-sand. Of particular note is the rapid decrease in electrical resistivity starting at approximately 10m. This decrease is due to the presence of a salt water intrusion at the site. Within the salt water intrusion, current flow is dominated by the fluid conductivity and thus the measurement is not sensitive to changes in geology.

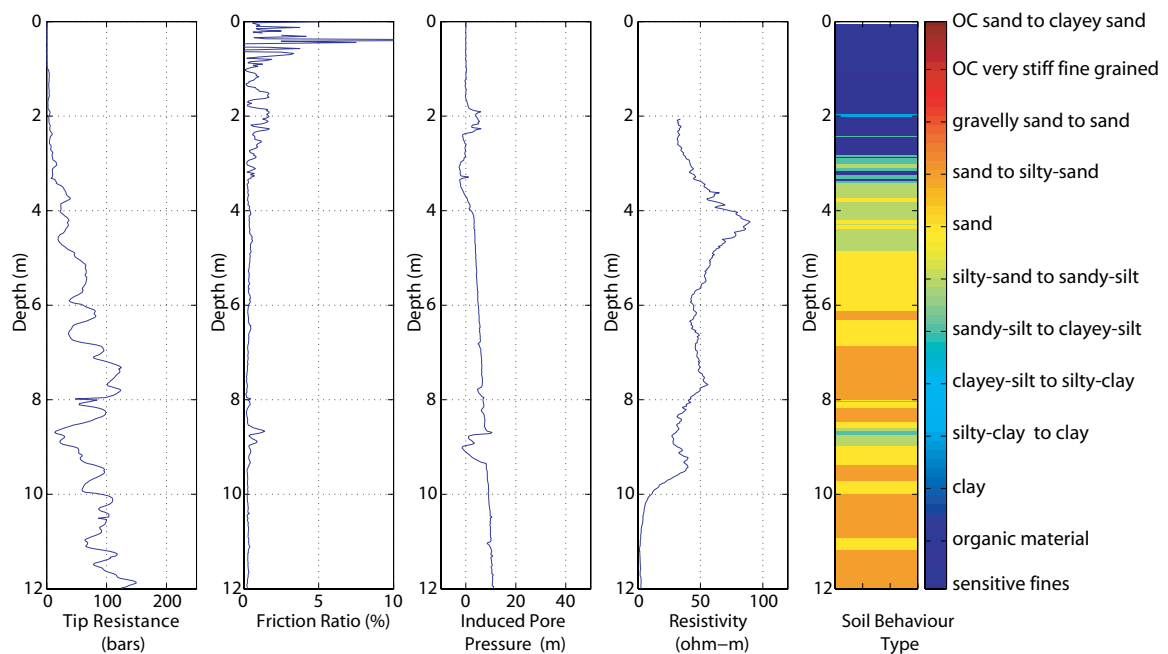


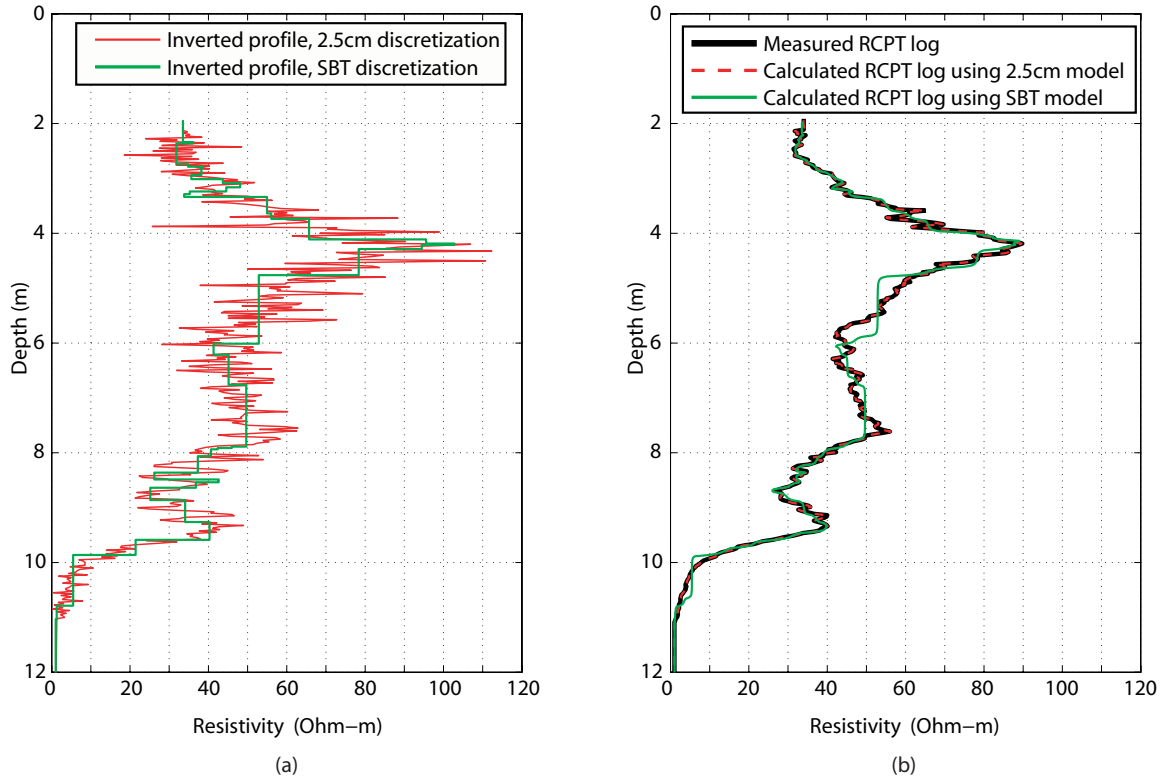
Figure 5.9 RCPT logs from the Kidd2 site.

Figure 5.10 shows the results from our inversions. In Figure 5.10a are shown the inverted 1-D resistivity profiles for two different discretization techniques; the red 1-D profile used a 2.5cm model discretization while the green profile uses a discretization that is based on the the SBT. In Figure 5.10b are the measured RCPT resistivity log and two calculated resistivity logs obtained for the two different discretizations.

In Figure 5.10b, we see that the calculated log for the 2.5cm discretization an excellent fit to the observed RCPT resistivity log. The red 1-D profile in Figure 5.10a has resistivities that vary over a smaller spatial scale and over larger magnitude range than the observed RCPT resistivity log in Figure 5.10b. From this, we can assert that the subsurface variability is considerably greater than as indicated by the observed RCPT resistivity log. We see a number of fine silt-clay layers as well as some highly resistive sand layers that are muted out in the observed RCPT log. This high resolution model can be used for evaluating potential anisotropy in the subsurface. If many thin clay layers were present, they may be muted by the RCPT. However, they can be very important because even a small number of thin clay layers can make a soil package electrically anisotropic. If one is using the RCPT data with other forms of measurement, such as electrical resistivity tomography, an understanding of anisotropy is key to merging these data. We note, however, that although this high resolution model is useful for evaluating anisotropy, it may not be the appropriate scale for making field interpretations. With this in mind, we inverted the data using a second discretization.

The green 1-D resistivity profile in Figure 5.10a is the inverted profile using a discretization that was based on the layering defined by SBT. Each continuous layer in the SBT profile was modeled as a single cell in the inversion. The green line in Figure 5.10b is the calculated RCPT resistivity log for the SBT discretization. Between the depths of 2m and 5m we see a good match to the observed RCPT resistivity log. From 5m to approximately 7.75m, there is a discrepancy between the observed and calculated resistivity logs. The observed RCPT resistivity log has considerable variability over this interval, however, the SBT over this depth exhibits small variability, indicating that in this region the SBT and resistivity values are poorly correlated. From 7.75m to 12m the two logs in Figure 5.10b agree well. The advantage of using the SBT discretization is that it immediately allows one to ascertain whether or not there is a relationship between

lithology (as defined by the SBT) and the observed RCPT resistivity log. In addition, because the SBT is based on different physical measurements, the inversion technique provides a systematic approach for linking the mechanical properties measured by CPT to the resistivity log.



**Figure 5.10 Inversion results for KIDD2 data. The red line corresponds to a discretization of 2.5cm. The green line corresponds to a discretization based on SBT. (a) The inverted 1-D resistivity profiles. (b) the measured RCPT log, and the calculated RCPT logs obtained from the inversion.**

## 5.6. Conclusions

---

In this paper we have used three synthetic experiments to explore the sensitivity and resolution of the UBC RCPT module. We have demonstrated that the measured resistivity log represents a smoothed version of the subsurface resistivity structure. This smoothing can be particularly important when there are fine clay layers, as these layers can give rise to anisotropy.

For the first example considered, we see that if the layer thickness is less than the electrode spacing, the resistivity log will have two peaks instead of one. These peaks are due to the electrode passing through the center of the thin layer. This example also demonstrates the vertical averaging that occurs during resistivity logging. Because of the averaging, the RCPT resistivity log will substantially overestimate the true in-situ resistivity of the clay layers. In order for the RCPT resistivity log to measure the true resistivity of a clay layer, the layer thickness must be greater than 20cm. However, even for a 20cm layer, the correct conductivity value will only be obtained at the center of the layer. In addition, we saw that the vertical averaging of the resistivity log can lead to an overestimation of layer thickness, as the module will sense the layer before it has actually been reached.

A second forward modeling experiment was performed that considered 15cm thick silt and clay layers, with variable resistivity, in a sandy background. The maximum resistivity contrast between the layers and the background was 1:10. For this experiment, the RCPT resistivity log does a relatively good job of capturing the true resistivities, with an overestimate of less than 10%. However, as with the first example we still overestimate layer thickness.

The third experiment considered the effect of truncated layers near the cone. From this experiment, we determined that the RCPT is sensitive to perturbations away from the cone location. For the case considered here, the sensitivity extends approximately 20cm radially away from the cone.

In addition to forward modeling, we have presented the theory for and demonstrated the practical application of an inversion algorithm that allows for

quantitative interpretation of the RCPT logs. Using this inversion technique we are able to recover the layered subsurface conductivity model that gives rise to the measured RCPT log. For the first two numerical experiments we recovered near perfect models using our inversion routine. For the third experiment, involving truncated layers, we recovered a noisy resistivity model. The noise was attributed to the fact that the RCPT logs contain measurable 3-D information. Our inverse result is constrained to be a layered structure, and thus when the true earth is locally not layered the inversion cannot match the true structure. In order to further illustrate the potential of our inversion approach, we applied our algorithm to field data. From the results of the inversions we demonstrated two key points. First, for this data set, there is substantial variability in the subsurface resistivity that is not evident in the true log. Second, at this test location there is no strong correlation between soil behavior type and electrical resistivity.

We feel that inversion, coupled with forward modeling is a powerful approach that can allow for quantitative interpretation of RCPT data. The inverted conductivity models are appropriate for use with lab scale relationships as they represent the true conductivity at a known scale. Furthermore, the approach presented here can be adapted for any RCPT module design. The models that result from the inversion process are independent of RCPT module design.

# CHAPTER 6

## CONCLUSIONS

---

Understanding the spatial distribution of subsurface properties is of paramount importance to effective management of contaminated sites. This, however, is a challenging task as most standard testing techniques result in sparse data that provide a limited picture of subsurface variability. Geophysical data, specifically resistivity measurements have been shown to be quite useful for improving models of the subsurface. Unfortunately, 3-D resistivity imaging techniques require boreholes for instrument deployment; at many contaminated sites these invasive methods are not acceptable, due to the risks associated with contacting and spreading the contaminants. Furthermore, standard resistivity surveys often have limited resolution away from the boreholes. Because of this, resistivity methods need further development for the specific application of near-surface imaging.

The underlying goal of this dissertation was to improve the state of electrical resistivity imaging for near-surface characterization. The goal was embodied in the development of cone-based electrical resistivity tomography (C-bert). This technology is a minimally invasive way of obtaining 3-D electrical conductivity images of the subsurface. By way of a successful field test of the C-bert system, I have demonstrated that it is a viable, and advantageous technique for imaging the near-surface. Moreover, the process of developing C-bert has necessitated the development of more than just a field technique. New forward and inverse modeling algorithms have been developed in order to accommodate this new type of data. Computational techniques for accounting for the effect of the cone penetrometer on the measured potential have been developed. Furthermore, I have created a new framework for interpreting resistivity cone penetration testing logs, so that they can be better understood and more amenable to integration with other types of data, such as C-bert.

The major contributions of this dissertation are as follows:

- ◆ Development and implementation of an improved 2.5-D electrical resistivity modeling algorithm. The algorithm includes an optimization scheme for acquiring the Fourier coefficients required for the 2.5-D approximation. As well, the algorithm includes a highly effective correction for reducing error associated with boundary conditions and source singularities.
- ◆ Development and implementation of a 3-D electrical resistivity inversion algorithm. The algorithm is flexible in that it allows for inversion of data using non-standard geometries. Furthermore, the algorithm includes a 3-D version of the boundary/source correction that was applied to the 2.5-D problem. Using this correction allows for a substantially smaller model space and thus increases the speed of the inversion.
- ◆ Design and realization of the C-bert acquisition system. This design was followed by a successful field deployment of the system at the Kidd2 research site in Richmond, British Columbia. Inversion of the data required the creation of a correction factor to account for the perturbation caused by the highly conductive cone. The correction factor was made computationally tractable by the advent of a new solution method for Poisson's equation. This solution, iteratively determined boundary conditions, results in an order of magnitude speed up over standard iterative methods. I note that although this solver was developed to accommodate the cone correction, it can be applied as a solver to any Poisson's equation. With the correction factor, I successfully inverted the field data, and demonstrated the usefulness of C-bert.
- ◆ Creation of a forward modeling and inversion framework for interpreting RCPT resistivity logs. I demonstrated that the measured RCPT resistivity log represent a non-linear average of the properties in a region surrounding the tool. This averaging can lead to the muting of fine clay layers, and thus information regarding possible anisotropy can be lost. Through inversion, however, we can remove the averaging effect and

recover a considerably higher resolution model of the subsurface conductivity. Furthermore, the results from the inversion are independent of probe geometry and, thus this technique allows for the quantitative comparison of data acquired using different tools.

C-bert has been shown to be a useful concept, however, this technique still has many avenues that need to be explored. As documented in chapter 4, much work went into developing a tractable way to account for the effect of the cone on the data. Ideally we would like to acquire a signal that is not subject to the perturbations associated with the cone. Now that C-bert has been demonstrated as a useful technique, the next logical step would be to explore the possibility of using non-conductive coatings on the cone rods to reduce, or eliminate, the cone effect.

Beyond further development of the testing method, I feel C-bert presents two other unique opportunities for future work. First, because of the way C-bert data are acquired, by pushing the cone at a series of different locations, it is particularly well suited to take advantage of the concept of real-time experimental design. As computational power increases and inversion algorithms are further refined, we will be able to obtain images in real-time. Based on these images, we can make intelligent choices about where to acquire our next C-bert profile, so as to maximize data worth. The second opportunity arises because we obtain multiple data types with C-bert. Having multiple data types allows for exploring the concept of informed inversion. Herein I used the RCPT logs to develop an accurate starting model for the inversions and to act as soft constraints in the inversions. However, another approach would be to develop an informed regularization operator that takes into account the other forms of data that are available from the C-bert survey.

The algorithms that I present for modeling and inverting RCPT data also open paths for future research. In particular, I feel that the inversion approach presented here can be extended as an upscaling technique for data integration. When integrating logging data with other forms of measurement, that have different spatial scales, we can invert our logging data on a grid that is discretized to correspond with our desired measurement scale (i.e. the upscaled grid). The resulting inverse model will be the upscaled parameter.

The advantage of formulating upscaling as an inverse problem is that we are then using the physics of the measurement to generate the upscaling relationship, rather than assuming some simple averaging relationship.

This dissertation makes several contributions to the state of electrical imaging in the near-surface. Most importantly, I developed and demonstrated the usefulness of C-berth. I showed that this technique is an effective way to acquire 3-D images of the subsurface conductivity structure. I have developed improved forward and inverse algorithms for modeling these and other types of electrical resistivity data. These algorithms have been released as open source software, in hopes of maximizing their impact on the near-surface community. My work on interpretation of RCPT has resulted in a better understanding of the averaging that is present with this measurement. Furthermore, the inverse approach I develop, allows one to remove this averaging effect and increase the resolution of the RCPT log.

# REFERENCES

---

Andersen, K., Brooks, S., and Hansen, M., 2001, A Bayesian approach to crack detection in electrically conductive media. *Inverse Problems*, 17, 121-136.

Archie, G. E., 1942, The electrical resistivity log as an aid in determining some reservoir characteristics. *Trans. Am. Inst. Min. Metall. Pet. Eng.*, 146, 54-62, 1942.

Binley, A., G. Cassiani, R. Middleton and P. Winship, 2002, Vadose zone flow model parameterisation using cross-borehole radar and resistivity imaging. *Journal of Hydrology*, 267: 147-159, 2002.

Campanella, R. G. and Weemees, I., 1990, Development and use of an electrical resistivity cone for groundwater contamination studies. *Can Geotech J*, 27, 557-567.

Cardimona, S.J. Clement, W.P. and Kadinsky-Cade, K., 1998. Seismic reflection and ground-penetrating radar imaging of a shallow aquifer. *Geophysics* vol. 63, No. 4 pp 1310-1317.

Catt, L.M., West, L.J., Clark, R. and Murray, T., 2005, Electrical Resistivity Inversion Constrained by Resistivity Cone Penetrometry (RCPT): Application to Landfill Site Characterisation. *Eos Trans. AGU*, 86 (18), Jt. Assem. Suppl., Abstract NS23A-03, New Orleans, LA, May 2005.

Clague, J. J., Luternauer, J. L. and Hebda, R. J., 1983, Sedimentary environments and postglacial history of the Fraser Delta and lower Fraser Valley, British Columbia. *Can.J.Earth Sci.* 20, 1314-26.

Dahlin, T., Garin, H. and Palm, M., 2004, Combined Resistivity Imaging and RCPT for Geotechnical Pre-investigation. *Procs. Nordic Geotechnical Meeting (NGM)*, 2004, Ystad Sweden.

Daily, W. and Ramirez, A., 1995, Electrical-resistance tomography during in-situ trichloroethylene remediation at the Savanna river site. *J.Appl.Geophys.*, 33, 239-249.

Daniel, C.R. Campanella, R.G., Howie, J.A., Giacheti, H.L., 2003, Specific Depth Cone Resistivity Measurements to Determine Soil Engineering Properties. *J. of Environmental and Engineering Geophysics.* ,Vol. 8 issue 1, pp 15-22.

Daniel, C.R., Giacheti, H.L., Howie, J.A. and Campanella, R.G., 1999, Resistivity Piezocone (RCPTU) Data Interpretation and Potential Applications. *XI Panamerican Conference on Soil Mechanics and Geotechnical Engineering* Foz do Iguassu, Brazil. pp.361-368.

- Dey, A. and Morrison, H. F., 1979, Resistivity modeling for arbitrarily shaped two-dimensional structures. *Geophysical Prospecting* 27, 106-136.
- Glover, P., M. J. Hole and J. Pous, 2000, A modified Archie's Law for two conducting phases. *EPSL*, 180, 369-383, 2000.
- Haber, E., Ascher, U. M., Aruliah, D. A. and Oldenburg, D. W., 2000a, Fast simulation of 3D electromagnetic problems using potentials. *J.Comput.Phys.(USA)*, **163**, 150-71.
- Haber, E., Ascher, U. M. and Oldenburg, D., 2000b, On optimization techniques for solving nonlinear inverse problems. *Inverse Probl.(UK)*, **16**, 1263-80.
- Hofmann, B. A., 1997, In situ ground freezing to obtain undisturbed samples of loose sand for liquefaction assessment. Ph.D. Thesis, Univ of Alberta.
- Hunter, J. A., Pullman, S. E., Burns, R. A., Good, R. L., Harris, J. B., Pugin, A., Skvortsov, A. and Goriainov, N. N., 1998, Downhole seismic logging for high-resolution reflection surveying in unconsolidated overburden. *Geophysics*, **63**, 1371-1384.
- Jackson, J. D., 1975 Classical Electrodynamics, John Wiley, New York.
- Jarvis, K. D. and Knight, R., 2000, Near-surface VSP surveys using the seismic cone penetrometer. *Geophysics*, **65**, 1048-1056.
- Jarvis, K. D. and Knight, R. J., 2002, Aquifer heterogeneity from SH-wave seismic impedance inversion. *Geophysics*, **67**, 1548-1557.
- Jarvis, K., Knight, R. J. and Howie, J. A., 1999, Geotechnical applications of VSP surveys using the seismic cone penetrometer. *Proceedings of the Symposium on the Application of geophysics to engineering and environmental problems*, 11-20.
- Kemna, A., Vanderborght, J., Kulesa, B. and Vereecken, H., 2002, Imaging and characterisation of subsurface solute transport using electrical resistivity tomography (ERT) and equivalent transport models. *J.Hydrol.*, **267**, 125-146.
- LaBrecque, D. J., Yang, X., 2001, Difference inversion of ERT data; a fast inversion method for 3-D in situ monitoring. *Journal of Environmental & Engineering Geophysics*, vol.6, no.2, pp.83-89.
- Lesmes, D.P. and Frye, K.M., 2001, Influence of por fluid chemistry on the complex conductivity and induced polarization responses of Berea sandstone. *J. Geophysical Research*, Vol. 106, B3, 4079-4090.

- Lunne, T., Robertson, P. K. and Powell, J. J. M., 1997, Cone penetration testing in geotechnical practice. Blackie Academic & Professional.
- Malinverno, A. and Torres-Verdin, C., 2000, Bayesian inversion of DC electrical measurements uncertainties for reservoir monitoring. *Inverse Problems* 16 (2000) 1343–1356.
- Narbutovskih, S. M., Daily, W. D., Morey, R. M. and Bell, R. S., 1997, Test results of CPT-deployed vertical electrode arrays at the DOE Hanford Site. Proceedings of the *Symposium on the Application of geophysics to engineering and environmental problems*, 21-31.
- Neilson-Welch, L., 1999, Saline water intrusion from Fraser River estuary: A hydrogeological investigation using field chemical data and a density-dependent groundwater flow model. M.S Thesis, Univ. of British Columbia.
- Neilson-Welch, L. and Smith, L., 2001, Saline water intrusion adjacent to the Fraser River, Richmond, British Columbia. *Can.Geotech.J.*, **38**, 67-82.
- Oldenburg D.W., Li Y., and Ellis R.G., 1997, Inversion of geophysical data over a copper gold porphyry deposit: a case history for Mt. Milligan. *Geophysics*, 62, No.5, 1419-1431.
- Per-Christian Hansen, 1998, Rank-Deficient and Discrete Ill-posed Problems: Numerical Aspects of Linear Inversion. SIAM monographs on mathematical modeling and computation.
- Pidlisecky, A. and Knight, R., 2006, FW2\_5D: A MATLAB 2.5-D Electrical resistivity modeling code. *Submitted to Computers and Geosciences*.
- Pidlisecky, A., Knight, R. and Haber, E. 2006. Cone-based Electrical Resistivity Tomography. To appear in *Geophysics*.
- Ramirez, A.L., Nitao, J.J., Hanley, W.G., Aines, R., Glaser, R.E., Sengupta, S.K., Dyer, K.M., Hickling, T. L., and Daily, W. D., 2005, Stochastic inversion of electrical resistivity changes using Markov Chain Monte Carlo approach. *J. Geophys. Res.*, 110, B02101, doi: 10.1029/2004JB003449.
- Robertson, P.K. 1990. Soil Classification using the cone penetration test. *Canadian Geotechnical Journal*, 27, pp 151-158.
- Saad, Y., 1996, Iterative Methods for Sparse Linear Systems. PWS Publishing Company.
- Singha, K. and Gorelick, S.M., 2005, Saline tracer visualized with electrical resistivity tomography: field scale spatial moment analysis. *Water Resources Research*, 41, W05023.

Singha, K. and Gorelick, S.M., 2006, The difficulty with field-scale petrophysical relations used to estimate tracer concentrations from electrical inversions: effects of spatially variable resolution. To appear in *Geophysics*.

Slater, L., A. M. Binley, W. Daily and Johnson, R., 2000, Cross-hole electrical imaging of a controlled saline tracer injection. *J.Appl.Geophys.*, 44: 85-102.

Slater, L., A. Binley, R. Versteeg, R., G. Cassiani, R. Birken and S. Sandberg, 2002, A 3D ERT study of solute transport in a large experimental tank. *J. Appl. Geophysics*, 49(4), 211-229.

Telford, W.M, Geldart, L.P.Sheriff, R.E., 1990, Applied Geophysics-Second Edition. Cambridge University Press, Cambridge

Tikhonov, A. N. and Arsenin, V. Y., 1977 Solutions of Ill-Posed Problems. Wiley, New York, 1977.

Versteeg, R., Birken, R., Sandberg, S. K. and Slater, L., 2000, Controlled imaging of fluid flow and a saline tracer using time lapse GPR and electrical resistivity tomography. *Proceedings of the symposium on the Application of geophysics to engineering and environmental problems*, 283-292.

Waxman, M. H.,and L. J. M. Smits, 1968, Electrical Conductivities in Oil-Bearing Shaly Sands, *Society of Petroleum Engineers Journal*, 243, 107-122, 1968.

Xu, S.Z., Duan, B.C., and Zang, D.H., 2000, Selection of the wavenumbers  $k$  using an optimization method for the inverse Fourier transform in 2.5D electrical modeling. *Geophysical Prospecting* 48, 789-796.

Yeh, T. C. J., Liu, S. Glass, R. J., Baker, K., Brainard, J.R., Alumbaugh, D. and LaBrecque, D., 2002, A geostatistically based inverse model for electrical resistivity surveys and its applications to vadose zone hydrology. *Water Resour. res.*, 38(12), 1278, doi:10.1029/2001WR001204.

Yuval., and Oldenburg, D.W., 1996, DC resistivity and IP methods in acid mine drainage problems: results from the Copper Cliff mine tailings impoundments. *Journal of Applied Geophysics*, 334, 187-198.

Zhang, J., Mackie, R. L., and Madden, T. R., 1995, 3-D resistivity forward modeling and inversion using conjugate gradients. *Geophysics* **60**, 1313-1325.